Offshore vertical wind shear: Final report on NORSEWInD's work task 3.1

Pena Diaz, Alfredo; Mikkelsen, Torben; Gryning, Sven-Erik; Hasager, Charlotte Bay; Hahmann, Andrea N.; Badger, Merete; Karagali, Ioanna; Courtney, Michael

Publication date:
2012

Document Version
Publisher's PDF, also known as Version of record

Offshore Vertical Wind Shear

Final report on NORSEWInD's work task 3.1

DTU Wind Energy E-Report

Alfredo Peña, Torben Mikkelsen, Sven-Erik Gryning,
Charlotte B. Hasager, Andrea N. Hahmann,
Merete Badger, Ioanna Karagali and Michael Courtney
DTU Wind Energy-E-Report-0005(EN)
August 2012

DTU Wind Energy
Department of Wind Energy

DTU Wind Energy-E-Report-0005(EN)

Offshore Vertical Wind Shear

Final report on NORSEWInD's work task 3.1 including deliverables:
3.2 Calculated vertical wind shears
3.3 Multi-variational correlation analysis
3.4 NWP data for wind shear model
3.5 Vertical extrapolation methodology
3.6 Results input into Satellite maps

Alfredo Peña, Torben Mikkelsen, Sven-Erik Gryning, Charlotte B. Hasager, Andrea N. Hahmann, Merete Badger, Ioanna Karagali and Michael S. Courtney

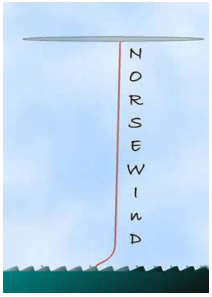

DTU Wind Energy
Department of Wind Energy

DTU

DTU Wind Energy, Risø Campus,
Technical University of Denmark, Roskilde, Denmark

August 2012

Author: Alfredo Peña, Torben Mikkelsen, Sven-Erik Gryning, Charlotte B. Hasager, Andrea N. Hahmann, Merete Badger, Ioanna Karagali and Michael S. Courtney
Title: Offshore Vertical Wind Shear
Final report on NORSEWInD's work task 3.1
Department: DTU Wind Energy

DTU Wind Energy-E-Report-0005(EN)
August 29, 2012

ISSN:
ISBN:
978-87-92896-04-9

Abstract (max. 2000 char)

This document reports on the analysis performed by the work task 3.1 of the EU NORSEWInD project and includes the following deliverables:

- 3.2 Calculated vertical wind shears
- 3.3 Multi-variational correlation analysis
- 3.4 NWP data for wind shear model
- 3.5 Vertical extrapolation methodology
- 3.6 Results input into satellite maps

The nature of the offshore vertical wind shear is investigated using acquired data from the NORSEWInD network of mast and wind lidar stations. The importance of the knowledge of the vertical wind speed profile and wind shear is first illustrated for the evaluation of power outputs. Background related to the parametrization of the vertical wind speed profile and the behavior of the vertical wind shear in and beyond the atmospheric surface layer is presented together with the application of the long-term atmospheric stability parameters for the analysis of the long-term vertical wind speed profile.
Observed vertical wind shears are illustrated for all NORSEWInD wind lidar and meteorological stations in terms of wind shear roses, distributions, and diurnal and monthly evolutions. A multi-variational correlation analysis is performed to study the vertical wind shear dependency on fetch, mean wind speed, seasonality and atmospheric stability. Numerical weather prediction data from the advanced weather research and forecasting (WRF) model is used to 1) Evaluate the ability of the model for the prediction of winds, temperatures and turbulent fluxes to be used for the extrapolation of wind speeds in the surface layer and 2) Construct a basis for the analysis of the long-term vertical wind speed profile and wind shear. A vertical extrapolation methodology for offshore wind resources is also presented based on different methods including profile methods, bulk and gradient Richardson numbers and long-term analysis of the atmospheric stability conditions. Finally, we propose alternatives for the extrapolation of surface winds typically from satellite retrievals and evaluate the effect of such methodologies on the wind speed, power density and vertical wind shear based on data from an offshore tall meteorological mast, where measures of the atmospheric stability can be performed based on observations and WRF outputs.

Contract no:
TREN-FP7EN-219048

Project no:
219048

Sponsorship:
EU

Cover:

Pages: 112
Tables: 2
Figures: 144
References: 68

Technical University of Denmark
Frederiksborgvej 399
4000 Roskilde
Denmark
Tel. +4546775024
bcar@dtu.dk
www.vindenergi.dtu.dk

Contents

1 Introduction

The collaborative EU-FP7 project "Northern Seas Wind Index database" also known as NORSEWInD observed through a network of stations the wind regime in the Northern European Seas. NORSEWInD's work package (WP) three–WP-3–worked on:

1. the analysis of the observations of the vertical wind shear at the NORSEWInD network of stations (nodes). This is work task (WT) one-WT-3.1, led by DTU Wind Energy–Risø campus.
2. the analysis of the effects of the platforms, rigs and structures on the wind flow observed by traditional anemometry (cup and sonic anemometers) and ground-based remote sensors (such as wind lidars and sodars) by means of computational fluid dynamics (CFD) and wind tunnel measurements. This is WT-3.2, which was led by the University of Strathclyde

This document reports on the findings and analysis carried out for WT-3.1, which includes the following deliverables:

- 3.2 Calculated vertical wind shears – Section 4
- 3.3 Multi-variational correlation analysis – Section 5
- 3.4 NWP data for wind shear model – Section 6
- 3.5 Vertical extrapolation methodology – Section 7
- 3.6 Results input into Satellite maps – Section 8

The main objective of WT-3.1 is the derivation and analysis of the vertical wind shear at 100-m height above mean sea level (AMSL), because this is the typical hub height (H_h) of the large wind turbines and, therefore, the height where NORSEWInD has focused the modeling, observation and analysis efforts. The vertical wind shear is a measure of the rate of change of the wind speed with height. The analysis and observation of the vertical wind shear is somehow a more complicated task compared to traditional wind resource assessment and wind campaigns, where only observations at one height (commonly hub height) are studied. The reason for this is that it implies an understanding of the physical processes behind the vertical wind speed profile and the parameters which controls it.

Knowledge of the vertical wind speed profile and wind shear is important for (among others):

- predicting winds at higher or lower heights from winds observed at a reference height. This is commonly performed in the meteorology community (not as common in the wind energy one though) through the use of wind profile models. However, most of these models are only valid within the surface boundary layer (SBL), which is the lowest part of of the atmospheric boundary layer (ABL) (typically less than 10% of if) where the fluxes of momentum and heat can be considered constant with height. Above the SBL, other models have to be used (Gryning et al., 2007a; Peña et al., 2008; Peña, 2009; Peña et al., 2010a; Sathe et al., 2011), since the wind becomes influenced by other scaling parameters that are otherwise negligible in the SBL.
- predicting wind power outputs. This is almost never performed, because the standard in the industry for power calculations is still the hub-height wind speed. However, as the wind turbines have grown in size, the rotors are exposed to a wide range of wind speeds while turning. The power generation is thus more related to the wind speed integrated over the heights where the rotor operates than to the hub-height only (see example below).

- predicting loads. Design loads are normally based on the variation of turbulence at a specific height under a specific range of wind speeds or turbulence measured at hub height. In the best of the cases, vertical turbulence and wind speed profiles are used for the estimation of loads, but the models employed are either simple or restricted to neutral atmospheric conditions.
- predicting wake effects. This is almost never performed since most of the engineering wind farm wake models are based on the hub height wind speed. With the advancement of CFD, the effect of the vertical wind shear has been started to be studied (Lu and Porté-Agel, 2011). By using information of atmospheric stability and measurements from ground-based remote sensors, such as wind lidars and sodars, these effects have also started to be quantified (Barthelmie and Jensen, 2010)
- performing power curve measurements. This has become rather popular in the recent years due to the need to minimize the uncertainty in the measurement of wind turbine power curves. By using more information on the vertical wind speed profile other than the hub-height wind speed, the scatter on the turbine's power measurements is reduced (Wagner et al., 2011)
- performing thrust curve measurements. This, as far as the authors are aware of, has never been done but as with the power curve measurements, it is a matter of time before the first attempts to reduce the thrust curve related uncertainties.

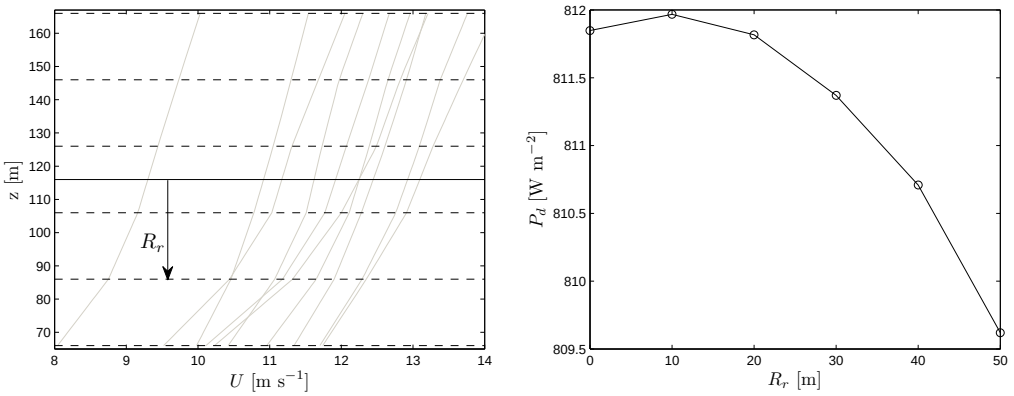

Figure 1: (left) Typical wind profiles measured at Horns Rev II, where a 'virtual' turbine hub height has been inserted at 116 m AMSL (solid black line) and different ranges for the profile analysis (within $\pm R_r$ in dashed lines). (right) Power density as function of the range of vertical levels used for the analysis ($R_r = 0$ corresponds to the P_d using information on u_h only). The results are based on more than 70000 10-min profiles.

To show the importance of accounting for the vertical wind shear, we have estimated the power density using wind speed measurements at one of the NORSEWInD stations (Horns Rev II). There, measurements were performed with a wind lidar at different levels and within the range 66–166 m, more than 70000 10-min vertical wind speed profiles were acquired. This range is here selected, since tall wind turbines operate within these levels (assuming H_h=116 m and a range of rotor radius R_r). When the time series of the hub-height wind speed u_h is used for predicting the power density P_d, as traditionally performed in wind energy,

$$P_d = \frac{1}{2}\rho\overline{u_h^3}, \tag{1}$$

where ρ is the air density (here assumed to have a constant value of 1 kg m^{-3}) and the overbar denotes the time mean, the result does not necessary correspond with the value found when taking into account the higher and lower wind speed levels. Using the equivalent wind speed

u_{eq}, which is the value based on the kinetic energy flux of the profile (Wagner et al., 2011),

$$u_{eq} = \left(\sum_i u_i^3 \frac{A_i}{A} \right)^{1/3}, \tag{2}$$

where u_i is the wind speed at the i-th height in the vertical wind speed profile and A_i is the area of the corresponding segment of the rotor swept area A, power densities can be estimated for different turbine dimensions (different R_r and therefore A values) by replacing u_h in Eq. (1) with u_{eq}. Figure 1-left illustrates a few number of wind profiles used for the power density calculations in Fig. 1-right, where it is shown that by using more wind speed levels, the estimated power densities vary. The degree of variation depends on the range of wind speed levels used for the analysis (here given by R_r), the nature of the vertical wind speed profile (its shape), the amount of profiles (10-min values) and the hub height.

NORSEWInD therefore provides us, for the first time, the means to massively analyze the offshore vertical wind shear at a large number of offshore meteorological stations and locations where wind lidars have been deployed in the Irish, North and Baltic Seas.

2 Background

2.1 The vertical wind speed profile and wind shear

Surface layer

Models and parameterizations for the offshore vertical wind speed profile are broadly used in the ABL community but they have not been completely implemented in the wind energy one. The latter mainly works based on the logarithmic wind speed profile,

$$u = \frac{u_*}{\kappa} \ln\left(\frac{z}{z_0}\right), \tag{3}$$

where u is the wind speed at a height z, u_* is the friction velocity, κ is the von Kármán constant (~ 0.4) and z_0 is the roughness length, which is valid within the SBL and under neutral atmospheric conditions only. The roughness length is commonly modeled over water surfaces using the expression of Charnock (Charnock, 1955),

$$z_0 = \alpha_c \frac{u_*^2}{g}, \tag{4}$$

where α_c is the Charnock's parameter and g the gravitational acceleration.

In most of the wind energy-related applications, the wind speed is therefore not modeled as function of atmospheric stability, although it is well known that this as well as other atmospheric variables, such as the boundary-layer height (BLH) and baroclinicity, have a strong impact on both the wind speed and the vertical wind speed profile shape. The diabatic vertical wind speed profile, i.e. the vertical wind speed profile in non-neutral atmospheric conditions, which has been found to fit well wind speed observations within the SBL (Gryning et al., 2007a; Peña and Gryning, 2008; Peña, 2009; Peña et al., 2010a),

$$u = \frac{u_*}{\kappa} \left[\ln\left(\frac{z}{z_0}\right) - \psi_m\right], \tag{5}$$

where ψ_m is the extension of the logarithmic wind speed profile to account for atmospheric stability, shows that the vertical wind shear is not a function of height and roughness length only, but also of atmospheric stability. The ψ_m forms are functions of the height above the ground and of the Obukhov length L, which can be directly estimated as

$$L = -\frac{u_*^3\, T}{\kappa\, g\, \overline{w'\Theta_v'}}, \tag{6}$$

where T is the mean temperature and $\overline{w'\Theta_v'}$ the kinematic virtual heat flux. Empirical forms for ψ_m can be found in the literature, and here we use for stable atmospheric conditions

$$\psi_m = -4.7\frac{z}{L} \tag{7}$$

and for unstable atmospheric conditions,

$$\psi_m = \frac{3}{2}\ln\left(\frac{1+x+x^2}{3}\right) - \sqrt{3}\arctan\left(\frac{2x+1}{\sqrt{3}}\right) + \frac{\pi}{\sqrt{3}} \tag{8}$$

where $x = \left(1 - 12\frac{z}{L}\right)^{1/3}$.

The above stability-roughness-height dependency of the wind shear can also illustrated by defining a vertical wind shear parameter based on, e.g. the power law expression,

$$u = u_r \left(\frac{z}{z_r}\right)^{\alpha}, \tag{9}$$

where u_r and z_r are a reference wind speed and height, respectively, and α the power law or wind shear exponent. The power law fits well the diabatic vertical wind speed profile, particularly when Eq. (9) is used locally. The integration of Eq. (9) respect to z gives

$$\frac{du}{dz} = u_r\, \alpha \left(\frac{z}{z_r}\right)^{\alpha-1} \left(\frac{1}{z_r}\right) = \frac{u_r\, \alpha}{z} \left(\frac{z}{z_r}\right)^{\alpha} = \alpha\frac{u}{z}, \tag{10}$$

so the power exponent can be expressed as

$$\alpha = \frac{du}{dz}\frac{z}{u}. \tag{11}$$

From Monin-Obukhov similarity theory (MOST) (Monin and Obukhov, 1954), the vertical wind speed gradient in the surface layer can be written as,

$$\frac{du}{dz} = \phi_m \frac{u_*}{\kappa z}, \tag{12}$$

where ϕ_m is the dimensionless wind shear, which is a function of the dimensionless stability parameter z/L and also some sort of the derivative with respect to height of ψ_m in Eq. (5). By inserting Eqs. (5) and (12) in (11), the power exponent becomes a function of stability, height and roughness,

$$\alpha = \frac{\phi_m}{\ln(z/z_o) - \psi_m}. \tag{13}$$

Although Eq. (13) is valid for the SBL only, it already shows that the commonly adopted value of α for wind energy calculations in offshore conditions, i.e. 0.2 (IEC, 2005), is valid for a very narrow set of conditions. Figure 2 illustrates the range of α values for a range of heights, roughness lengths and stability conditions (different colors) based on Eq. (13).

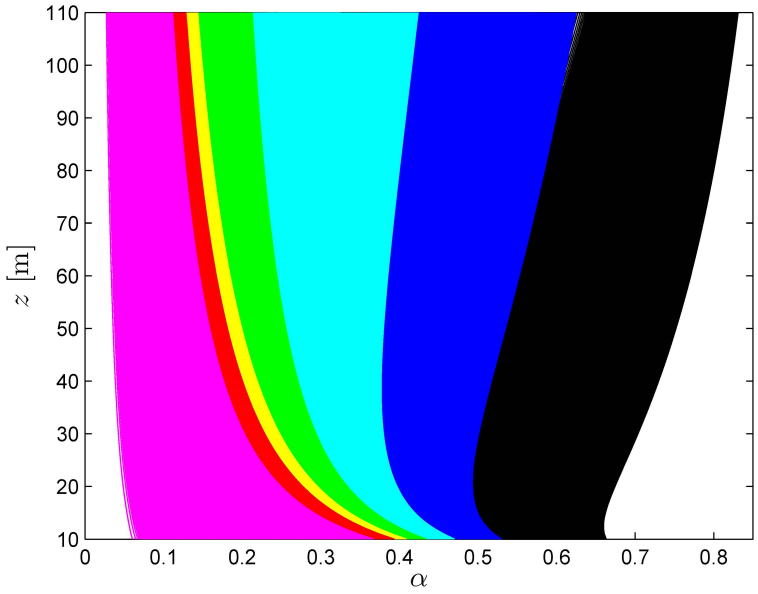

Figure 2: The behavior of the wind shear exponent α with height, surface roughness and atmospheric stability from Eq. (13). The left-most curve within each color range corresponds to the lowest roughness value (0.1 mm) typical of very smooth water surfaces and the right-most to the highest roughness value (1 m) typical of forest and vegetated areas. The colors show the range of atmospheric stability conditions: magenta (very unstable), red (unstable), yellow (near unstable), green (neutral), cyan (near stable), blue (stable) and black (very stable)

Beyond surface layer

Above the surface layer, the vertical wind speed profile and wind shear become dependent on other scaling factors such as the BLH, here denoted as z_i, among others. Using mixing-length theory, Gryning et al. (2007a) and Peña et al. (2008, 2010a) proposed models for the vertical wind speed profile, which similarly to the analysis done before for MOST, show a dependency of α on z_i. Taking the "most simplified" model, i.e. that in Peña et al. (2008),

$$\frac{du}{dz} = \frac{u_*}{\kappa}\left(1 - \frac{z}{z_i}\right)\left(\frac{1}{z}\phi_m + \frac{1}{z_i - z}\right) \qquad \text{and,} \tag{14}$$

$$u = \frac{u_*}{\kappa}\left[\ln\left(\frac{z}{z_o}\right) - \psi_m f_s\right], \tag{15}$$

where $f_s = 1$ and $f_s = 1 - z/(2z_i)$ for unstable and stable conditions, respectively, it is simple to demonstrate α's dependency on z_i by integrating Eqs. (14) and (15) in (11),

$$\alpha = \frac{\phi_m\left(1 - z/z_i\right) + z/z_i}{\ln\left(z/z_o\right) - \psi_m f_s}. \tag{16}$$

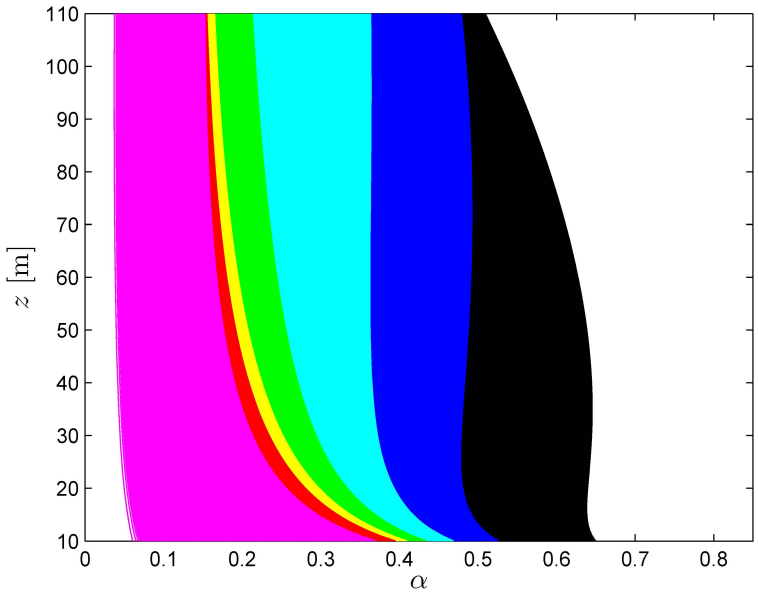

Figure 3: As Figure 2 but for the model in Eq. (16)

2.2 Long-term vertical wind speed profile

The analysis shown so far reflects the behavior of the 'short-term vertical wind speed profile', which is that observed on a 'instantaneous' basis, i.e. the average vertical wind speed profile within 10-, 30-min or even some hours. It also works well when classifying the vertical wind speed profiles in different atmospheric stability conditions, as shown in the analysis in Gryning et al. (2007a); Peña and Gryning (2008); Peña et al. (2008); Peña (2009); Peña et al. (2010a,b).

In many wind resource campaigns, however, the instantaneous measurements are not analyzed but the average of all measurements. When averaging, especially in a long term campaign (with a minimum measurement period of at least one year), all atmospheric stability situations may occur. Thus, vertical wind speed profiles from a wide range of atmospheric conditions are averaged together, which results in an average vertical wind speed profile that is very close to that typical of neutral atmospheric conditions, although it generally shows some deviations. This is due to the fact that not all atmospheric stability conditions have the same weight in the wind profile and thus knowledge of the long term atmospheric stability is required to correct the long term wind speed profile from its neutral form. In other words, we need to estimate the long-term stability correction $\langle\psi_m\rangle$, which is not equal to the ψ_m function evaluated for a mean value of the Obukhov length, so $\langle\psi_m(z/L)\rangle \neq \psi_m(z/\langle L\rangle)$.

Long term atmospheric stability correction

Kelly and Gryning (2010) modeled the probability density function P of $1/L$ as,

$$P = n_{\pm}\frac{C_{\pm}}{\sigma_{\pm}}\frac{\exp\left[-\left(C_{\pm}\left|1/L\right|/\sigma_{\pm}\right)^{2/3}\right]}{\Gamma\left[1 + 3/2\right]}, \tag{17}$$

where the subscripts $+$ and $-$ denote the stable and unstable 'sides' of the distribution, $n_{\pm}$ are fractions of occurrence of each stability side, $C_{\pm}$ are semi-empirical constants reflecting the 'speed' of the distribution and $\sigma_{\pm}$ are scales of variations in $1/L$, which are based on the long-term standard deviation of $\overline{w'\theta'_v}$ and the average u_* value,

$$\sigma_{\pm} = \frac{g}{\langle \overline{T} \rangle} \frac{\langle \left(\overline{w'\theta'_v} - \langle \overline{w'\theta'_v} \rangle_{\pm} \right)^2 \rangle^{1/2}}{\langle u_*^3 \rangle}. \tag{18}$$

The $\sigma_{\pm}$ are used to estimate the average long-term stability correction of the average wind speed profile,

$$\langle \psi_m \rangle = -n_+ \frac{3\sigma_+}{C_+} b' \ z + n_- \ f_-, \tag{19}$$

where $b' = b/\Gamma[5/3]$ (b comes from the stable common form $\psi_m = bz/L$) and f_- is a function of σ_-, C_-, z and β, which comes from the unstable common form $\phi_m = (1 - \beta z/L)^{-1/3}$. The exact formulation of f_- can be found in Kelly and Gryning (2010).

Application to the long-term wind profile

The integration of the long-term atmospheric stability correction with the vertical wind speed profile models results in parameterizations similar to that in Eq. (5). Without taking into account the BLH effect on the vertical wind speed profile, one can easily derive the MOST-based long-term vertical wind speed profile:

$$\left\langle \frac{\kappa u(z)}{u_*} \right\rangle = \ln \left(\frac{z}{z_o} \right) - \langle \psi_m \rangle. \tag{20}$$

Kelly and Gryning (2010) derived the following expression when using the vertical wind speed gradient of Gryning et al. (2007a):

$$\left\langle \frac{\kappa u(z)}{u_*} \right\rangle = \ln \left(\frac{z}{z_o} \right) - \left(1 - \frac{z}{z_m} \right) \langle \psi_m \rangle - \frac{1}{z_m} \int_{z_o}^{z} \langle \psi_m \rangle dz + \frac{z_m}{2L_m} \left[1 - \left(1 - \frac{z}{z_m} \right)^2 \right], \tag{21}$$

where z_m and L_m are the effective means of the BLH and the middle boundary layer length scale. Here, we provide a simpler expression (it neglects the contribution of L_m), which results from the vertical wind speed gradient of Peña et al. (2008)

$$\left\langle \frac{\kappa u(z)}{u_*} \right\rangle = \ln \left(\frac{z}{z_o} \right) - \left(1 - \frac{z}{z_m} \right) \langle \psi_m \rangle - \frac{1}{z_m} \int_{z_o}^{z} \langle \psi_m \rangle dz. \tag{22}$$

3 NORSEWInD network of stations

We analyze data from the NORSEWInD network of stations/nodes, which are available at the NORSEWInD database (DB). Only those stations, which were available at the DB at the time 23:50 CET of October 31 2011 (deadline for uploading data) are used. Data from other NORSEWInD stations are available in the DB, but there is no description of them (at least not before the deadline).

Figure 4 illustrates the locations of the network of stations of the NORSEWInD project used for the analysis of the offshore vertical wind shear. Except for the Høvsøre and Utsira stations, all other nodes are offshore. 14 stations are available, from which 7 of them are meteorological masts dedicated for wind speed measurements that NORSEWInD obtained permission to use. The other 7 are either platforms, oil rigs or offshore structures where wind lidars have been deployed (mostly through NORSEWInD). It is important to highlight that at any of the wind lidar nodes there are meteorological data other than those retrieved by the wind lidars.

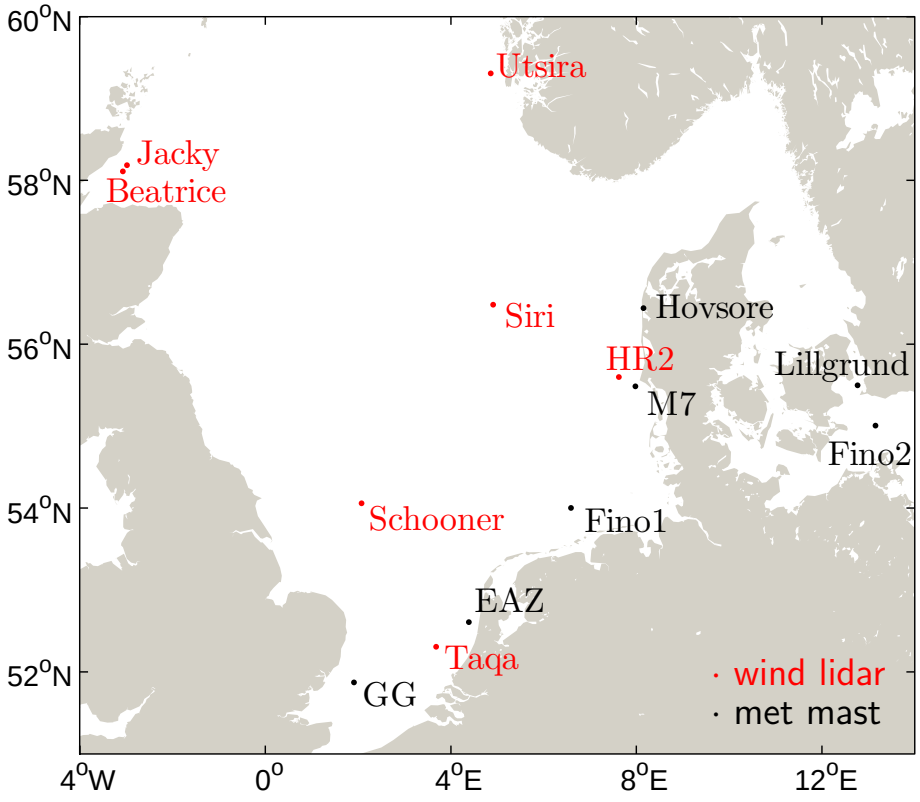

Figure 4: NORSEWInD network of meteorological and wind lidar stations in the North and Baltic Seas

Table 1 summarizes the period of measurements available for each of the NORSEWInD nodes, together with the available data, type of measurement and heights of observation. All data in the DB are reported based on 10-min means.

The NORSEWInD DB has data from two types of wind lidars. The first is the WindCube unit from the company Leosphere, which is a pulsed wind lidar. For details on the wind lidars refer to Peña (2009) and Courtney et al. (2008). For this type of wind lidar, only 10-min data that have both carrier-to-noise ratios (CNRs) larger or equal to -20 dB and an 'availability' of 100%[1] are used. By setting this filter, the amount of 10-min profiles which can be retrieved

[1]The parameter availability is here related to the amount of measurements within a period where the CNR

Table 1: NORSEWInD nodes information. Also displayed are the heigths of measurement of wind speed (WS), temperature (T), pressure (P), relative humidity (RH), wind direction (WD) and sonic (S)

Node	Node type	Period in DB	No. of 10 min	Height of WS AMSL [m]	Height of other measures AMSL [m]
Jacky	wind lidar	2010-11-10–	923	60–320	-
	WindCube	2011-11-09	5347	[60, 80, 100]	
Siri	wind lidar	2010-06-02–	6277	85–345	-
	WindCube	2011-05-02	20243	[85, 105, 125]	
Schooner	wind lidar	2010-07-16–	24525	76–216	-
	WindCube	2011-11-09	28572	[76, 92, 99]	
Taqa	wind lidar	2010-02-25–	38748	70–250	-
	WindCube	2011-03-19	47317	[70, 90, 110]	
HR2	wind lidar	2009-06-25–	70650	66–286	-
(Horns Rev II)	WindCube	2011-08-17	94848	[66, 86, 106]	
Utsira	wind lidar	2009-09-28–	33649	67–300	-
	WindCube	2011-07-01	59908	[67, 80, 100]	
Beatrice	wind lidar	2010-11-10–	9034	[52.5, 75.5, 90.5...	-
	ZephIR	2011-02-25		105.5, 162.5]	
Høvsøre	met mast	2004-02-28–	60828	[10, 40, 60...	S-10
(flat and homo.)		2011-12-18		80, 100]	
M7	met mast	2005-01-01–	297826	[20, 30, 40...	P-16
(Horns Rev I)		2009-12-15		50, 60, 70]	WD-[28, 68]
					T-[-3, 16, 64]
Fino 1	met mast	2003-07-30–	28530	[33, 40, 50,	T-[-3, 30, 40, 50, 70, 100]
		2010-05-01	85942	80, 90, 100]	P-[20, 90]
					WD-[33, 40, 50, 60, 80]
					RH-[33, 50, 90]
Lillgrund	met mast	2009-01-01–	52482	[13, 20, 40...	P-5, RH-7
		2009-12-31		63, 65]	T-7, WD-[18, 61]
Fino 2	met mast	2007-07-31–	66991	[32, 42, 52, 62...	WD-[31, 51, 71, 91]
		2010-04-30	75244	72, 82, 92, 102]	RH-[30, 50, 99]
					T-[30, 40, 50, 70, 99]
					P-[30, 90]
EAZ	met mast	2005-07-01–	4501	[21, 70, 116]	RH-[21, 70, 116]
(Egmond aan Zee)		2008-12-31	96185		P-20, WD-[21, 70, 116]
					T-[-3.8, 21, 70, 116]
GG	met mast	2006-01-23–	222033	[42.5, 52.5, 72.5...	WD-62.5, P-84.5
(Greater Gabbard)		2010-07-12		82.5, 86.5]	T-84.5, RH-38.5

up to the highest range of measurements (~ 300 m) decreases compared to the theoretical amount of profiles that can be retrieved during the period of deployment. These are the numbers shown in the first line corresponding to each WindCube node in Table 1. To increase the amount of data without loosing accuracy on the wind speed measurements (same filters are applied) and due to the fact that the analysis is based on observations at 100 m AMSL, another set of data is prepared for a shorter range of heights (up to ~ 100 m AMSL). These are the numbers shown in the second line for each WindCube node. Wind directions are retrieved at all wind speed heights.

The second type of wind lidar is the ZephIR unit from the company Natural Power, which

is lower than a threshold limit

is a continous wave wind lidar. The laser principle is different in this type of instrument, so there are 'always' measurements at each programmed height. The filter here only allows 10-min data with more than 100 'points in fit' (a measure of the accuracy of the wind speed retrieval algorithm), a CS≤ 0.3 (this is a measure of the degree of activity of the cloud correction algorithm) and no precipitation. Two other heights, 38 and 800 m above the lidar level (ALL), are programmed to correct for fog and cloud contamination. Wind directions are also retrieved at all wind speed heights.

In this WT, we also performed analysis of the effects of fog and clouds on the wind lidars when these where placed at Høvsøre for testing, calibration and verification prior to deployment. This is shown in Appendix A. A wind lidar was also placed at the Fino 3 meteorological mast as part of the NORSEWInD project. In Appendix B we illustrate some of the findings of the analysis of both wind lidar and Fino 3 measurements in which this WT was involved.

Data are always very different from mast to mast. In the case of the Høvsøre meteorological mast, we bypass the NORSEWInD DB and use DTU Wind Energy's DB, since in the latter we also have records of the turbulent fluxes from the sonic anemometers. Here we use those from the sonic at 10 m and the amount of data corresponds to concurrent sonic/cup anemometer data. The mast is located 1.7 km from the west coast of Denmark and in order to analyze the wind shear corresponding to flat and homogenous terrain, we restrict the study to the sector 30°–120° (with north at 0°). Refer to Jørgensen et al. (2008) and Peña (2009) for details of the site and meteorological mast at Høvsøre.

For some of the other masts there are two sets of data (thus two lines in Table 1). The first, a shorter dataset, contains 'processed data', i.e. data that have been filtered and corrected due to mast/boom flow distortion by the NORSEWInD partner Fraunhofer IWES (Hagemann et al., 2009b). Further details on the masts can be found in (Hagemann et al., 2009a).

4 Observed vertical wind shears

The vertical wind shear has been analyzed by means of the power exponent α in Eq. (11). The term du/dz has been approximated to $\Delta u/\Delta z$, i.e. the ratio of the difference of wind speeds between two levels to the height difference of those levels, z is the geometrical mean between the two levels and u is the wind speed at that geometrical mean, so the wind speeds at these two levels have been averaged.

The α parameter can also be directly estimated from the power law in Eq. (9). However, in this case is not obvious the level where α is estimated. We analyze the Utsira wind lidar data to compare the two methods for α estimation. Figure 5 shows the results for α measured using the heights 40 and 53 m ALL, shown as 'power law', since it uses Eq. (9) and using Eq. (11) shown as 'gradient'; first applying it to the heights 40 and 53 m ALL (left frame) and second applying it to the heights 53 and 73 m ALL (right frame). The results not only show that the 'gradient' and 'power law' methods are equivalent, but also that the vertical wind shear is a very local measure, since it already varies when computed from a higher layer.

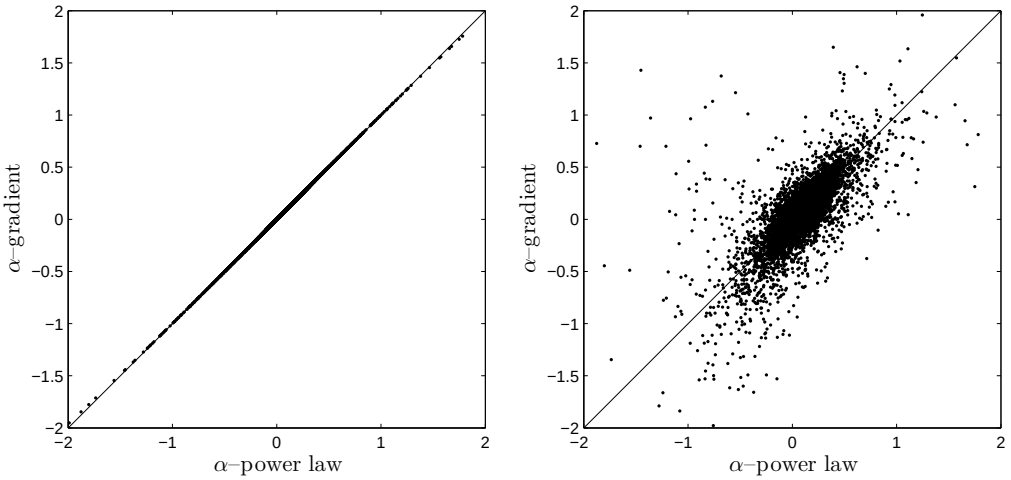

Figure 5: The power exponent α estimated from Eq. (9) (power law) at 53 and 73 m ALL compared to its estimation from Eq. (11) at 40 and 53 m ALL (left) and at 53 and 73 m ALL (right)

4.1 Wind lidar nodes

At NORSEWInD wind lidars are used over platforms and oil rigs. At all wind lidar nodes, the observations include heights above 100 m AMSL (the target height for wind shear analysis in NORSEWInD). As shown in Table 1, the amount of 10-min measurements for the nodes using WindCubes increases, when only the first three heights are examined (second line on each node). Therefore, in this section we will concentrate on the dataset, which provides us with the highest amount of measurements.

Utsira

This wind lidar was placed over the island of Utsira and, therefore, the wind speed measurements, and thus the vertical wind shear, will be affected by the orography and roughness of the island. The first four measurements are performed at 40, 53, 73 and 93 m ALL. According to the lidar installation report (Kindler, 2010b), the unit was installed at a height 27 m AMSL. The wind lidar first four measurements are then at 67, 80, 100 and 120 m AMSL, thus the wind shear can be estimated at 73.5, 90 and 110 m AMSL.

The winds at Utsira come nearly either from north or south (Fig. 6). The orographic effect on the wind speed for the northerly sector is high as estimated from the wind atlas analysis and application program (WASP) (Mortensen et al., 2007) as shown in Fig. 7 at 67 m AMSL.

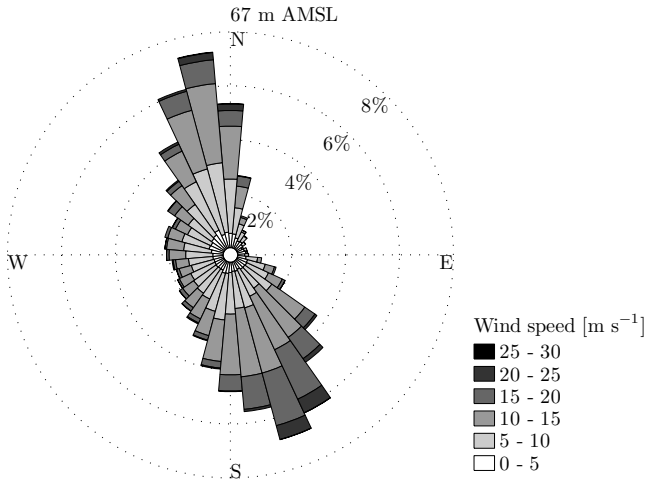

Figure 6: *The wind rose at Utsira at 67 m AMSL*

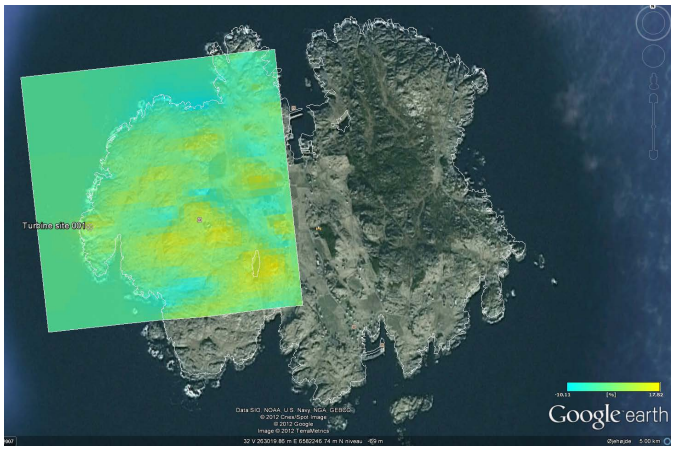

Figure 7: *The orographic speed effect on the Utsira island at 67 m AMSL for northerly winds*

The analysis of the vertical wind shear should take into account these effects. In Appendix C, we perform an analysis of such orographic effects by using WAsP Engineering (WAsP Eng) (Mann et al., 2002). However, we will not correct the data because we found an inconsistency between the orography map and the installation report. According to the map, the wind lidar is located at 19.6 m AMSL, i.e. 7.4 m lower than the installation report height. A visual inspection of the map in Google Earth also shows a slight displacement of the map. Therefore, the orographic effects calculated at the wind lidar location might differ from those observed and any correction will add to the uncertainty due to the methods used for the correction, the uncertainty on the displacement of the map.

Figure 8 shows the vertical wind shear rose at 90 m AMSL (which is the closest level to the 100 m AMSL one). It is observed that most of the α values are in the range 0–0.125 for most of the sectors and that the percentage of negative and very positive (> 0.25) values is rather high.

A more complete illustration of the range of α values for all sectors is shown in Fig. 9. There, the centroid of the distribution is also illustrated, which is found to be close to the value estimated using Eq. (13) assuming neutral atmospheric conditions, a close to water

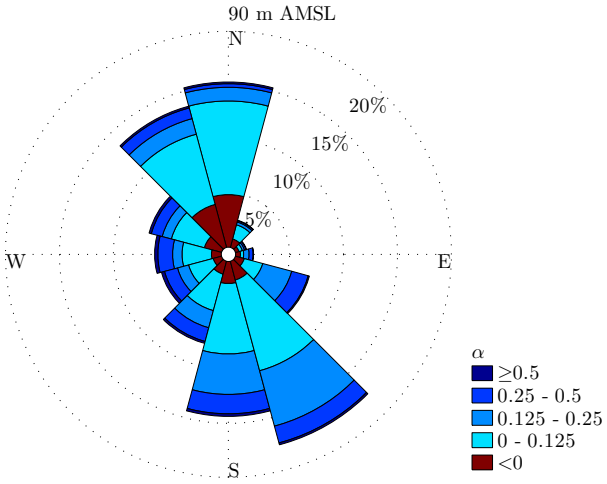

Figure 8: *The vertical wind shear rose at 90 m AMSL at Utsira*

roughness, $z_o = 0.0002$ m, and at 90 m ($\alpha = 0.077$). It is clear that there is a high amount of cases where α becomes negative (meaning that the wind speed decreases with height) and another high amount of cases where α is very high.

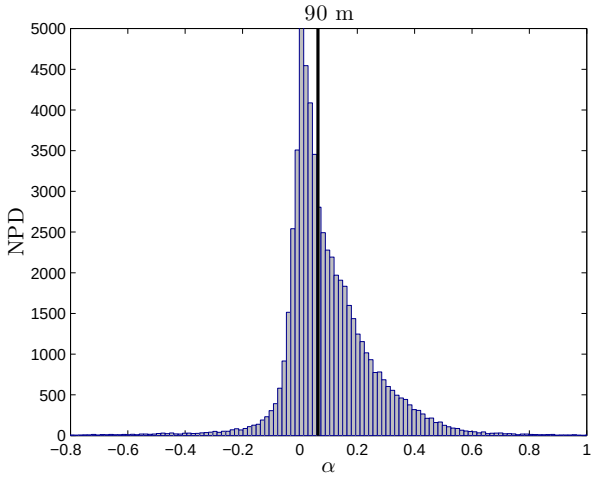

Figure 9: *All-sector distribution of the vertical wind shear at 90 m AMSL at Utsira. The solid black line represents the centroid of the distribution* $\alpha = 0.0630$

One expects that some negative α values will be measured, since under unstable atmospheric conditions the wind speed does not strongly increases with height. In the particular case of Utsira, negative α values can be associated with the speed up effect of the island. According to the findings from the WAsP Eng analysis in Appendix C, speed ups will be observed up to 140 m ALL for the west and east sectors and at all wind lidar heights for the north and south sectors, partly explaining the low α values. However, as it will be shown for the other NORSEWInD nodes, these low α values are always present, although the measurements are performed over the 'flat' sea.

The diurnal and monthly evolutions of the α-values measured at 90 m AMSL from October 1, 2009, to September 30, 2011, (to try to avoid a diurnal or monthly bias) are illustrated in Fig. 10. There is no evidence of a diurnal variation of α and its seasonal variation is little; α is lowest at the end of summer (August and September) and increases during the winter period.

There is almost no diurnal variation because on the mean the sea temperature does not

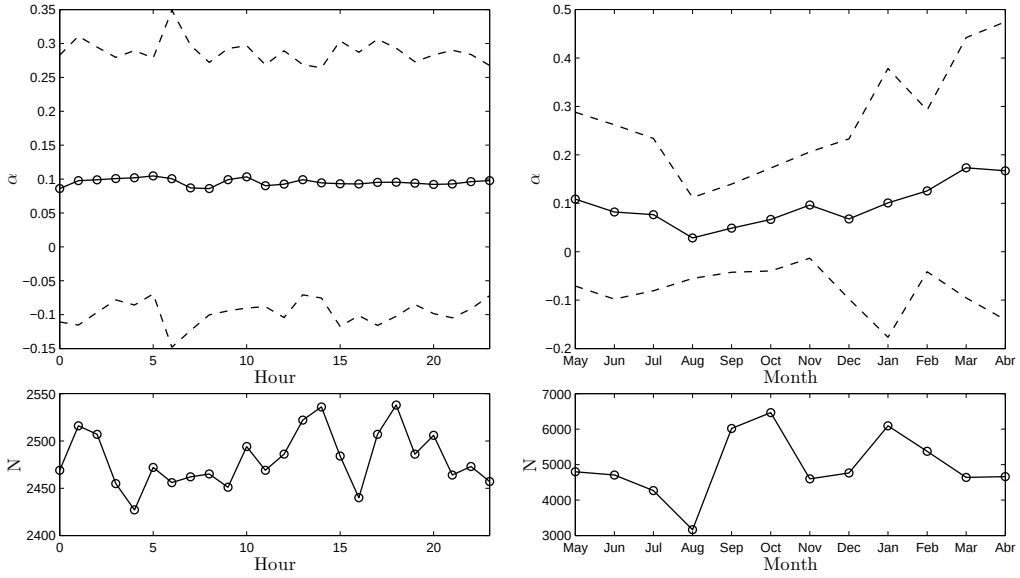

Figure 10: (top) Diurnal (left) and monthly (right) evolution of the all-sector mean vertical wind shear at 90 m AMSL at Utsira. The dash lines represent the mean±1 standard deviation. (bottom) Number of 10-min measurements used for the calculations on top

vary during the day. As low α values are usually found under convective situations (see Fig. 2), we also expect to find the lowest values when the sea is warmest, which is about late summer. As the sea gets colder during the winter months, the atmosphere is often stable and so α increases.

Horns Rev II

This wind lidar was placed on the transformer/platform of the Horns Rev II wind farm. The wind speed measurements at the lower levels and thus the vertical wind shear might be affected by the distortion of the platform. The first four measurements are performed at 40, 60, 80 and 100 m ALL. According to the lidar installation report (Kindler, 2010a), the unit was installed on the deck of the platform at 26 m AMSL. The wind lidar's first three measurements are then at 66, 86 and 106 AMSL, thus the wind shear can be estimated at 76 and 96 m AMSL.

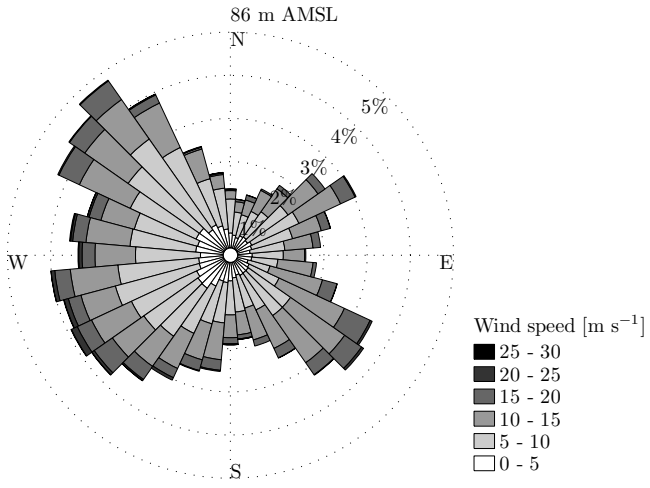

Figure 11: The wind rose at Horns Rev II at 86 m AMSL

According to the CFD and wind tunnel results of Stickland et al. (2010), wind lidar measurements performed at the Horns Rev II transformer do not need to be corrected for platform distortion when they are performed above 2.4 times the platform height. This means that only measurements below 62.5 m AMSL are influenced by the platform.

The winds at Horns Rev II mainly come from the west sectors (Fig. 11). Therefore, the wind speeds measured at the platform are affected by the wake of the wind farm (Fig. 12). The wake effects on the wind lidar observations can be observed when looking at the sector-wise mean vertical wind speed profile (Fig. 13). There only 12 sectors have been used for the analysis (sector 1 is oriented to the north and the counting is clockwise) and it is clearly seen that the wake sectors (8–12) have lower wind speeds for the first ~ 120 m AMSL.

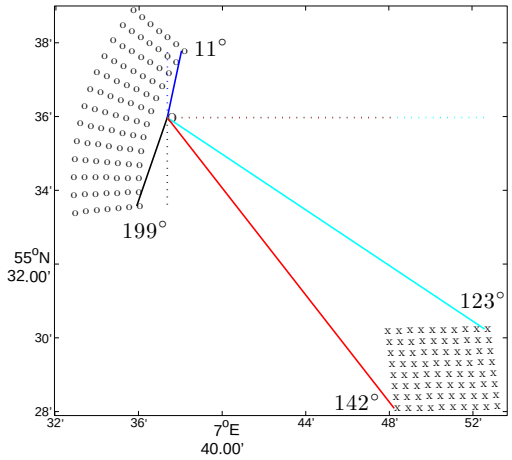

Figure 12: *Layout of the Horns Rev I and II wind farms. The platform location is shown in a circle*

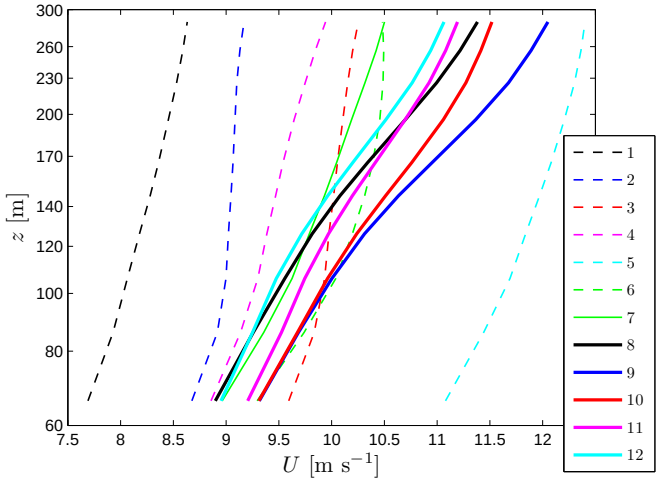

Figure 13: *Mean vertical wind speed profiles per sector at Horns Rev II*

Also interesting is that the vertical wind speed profiles correspondent to the east sectors (2–4), where the land is closest to the platform (~ 28 km) seem to face over-speeding at the first measurement levels. There might be a roughness/orographic effect due to the land mass. Simulations carried out with WAsP at the wind lidar measuring heights reveal a slight over-speeding due to roughness, which is decreasing the higher the level of measurement. At 66 m AMSL, the over-speeding is 0.28% and at 286 m is 0.10%. We will not attempt to correct the measurements for this effect, since these values are very low and, although they are in agreement with the measured profiles, they only reduce the wind speed ~ 0.03 m s^{-1}

at the highest. Also, the WAsP simulations are performed with a rather simple terrain map.

Figure 14 shows the vertical wind shear rose at 96 m AMSL at Horns Rev II. As with the Utsira data, it is observed that most of the α values are in the range 0–0.125 for most of the sectors, although the amount of higher values is larger. This is particularly observed at the wake sectors, where it is clear that α is higher at 100 m AMSL compared to a non-wake sector.

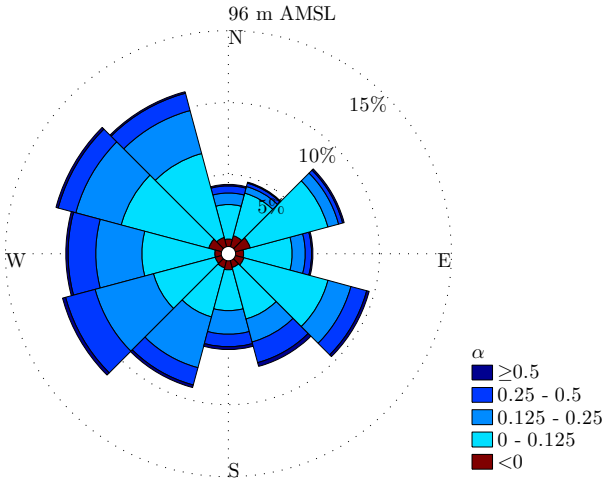

Figure 14: *The vertical wind shear rose at 96 m AMSL at Horns Rev II*

The range of α values for all sectors is shown in Fig. 15. The centroid of the distribution (0.0950) is higher than the theoretical neutral one (0.076) due to the wake of the wind farm in the predominant sectors. The distribution is very similar to that at Utsira, and we also found a high amount of cases where α is negative or very high.

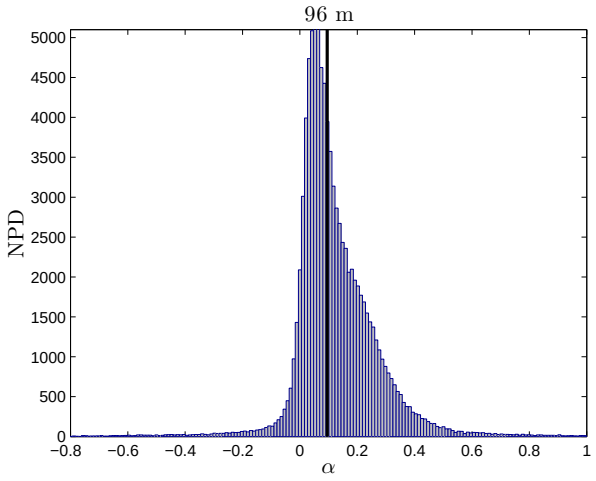

Figure 15: *All-sector distribution of the vertical wind shear at 96 m AMSL at Horns Rev II. The solid black line represents the centroid of the distribution* $\alpha = 0.0950$

The diurnal and monthly evolutions of the α-values measured at 96 m AMSL from July 1, 2009, to August 31, 2011, (to try to avoid the diurnal or monthly bias) are illustrated in Fig. 16. As shown at Utsira (the diurnal and monthly behaviors of α at Horns Rev II are very similar), there is no evidence of diurnal variation of α. The seasonal variation is little; α is lowest at the autumn months and increases during the winter period (peaking in April).

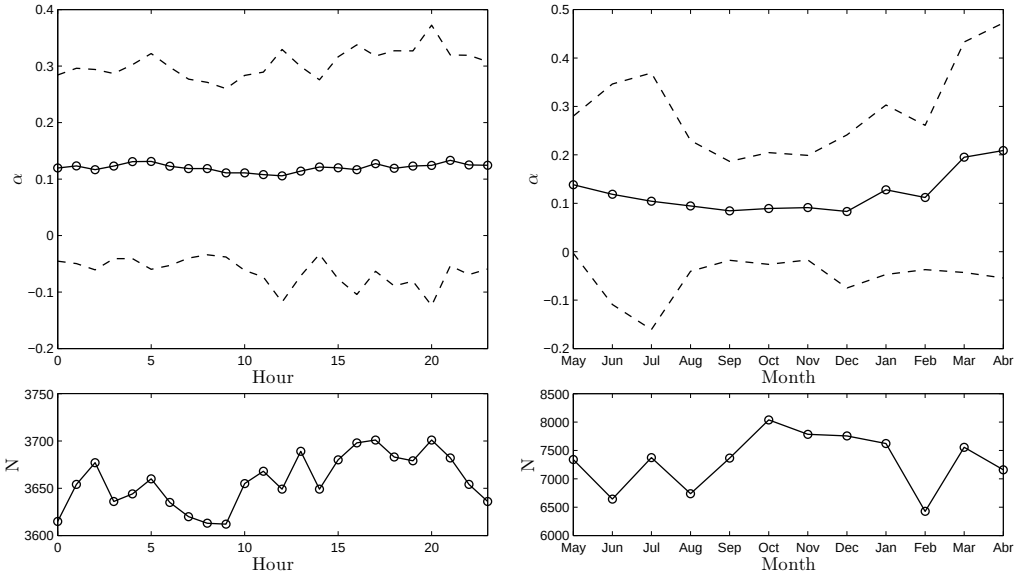

Figure 16: (top) Diurnal (left) and monthly (right) evolution of the all-sector mean vertical wind shear at 96 m AMSL at Horns Rev II. The dash lines represent the mean±1 standard deviation. (bottom) Number of 10-min measurements used for the calculations on top

Taqa

This wind lidar was placed on the Taqa P15-F gas rig. The first four measurements are performed at 40, 60, 80 and 100 m ALL. According to the lidar installation report (Kindler, 2010d), the unit was installed near the helipad at 30 m AMSL. The wind lidar first three measurements are then at 70, 90 and 110 AMSL, thus the wind shear can be estimated at 80 and 100 m AMSL. Assuming that the CFD and wind tunnel results of Stickland et al. (2010) for the Horns Rev II are also valid for the Taqa platform, wind lidar measurements performed above 72 m AMSL do not need to be corrected for flow distortion.

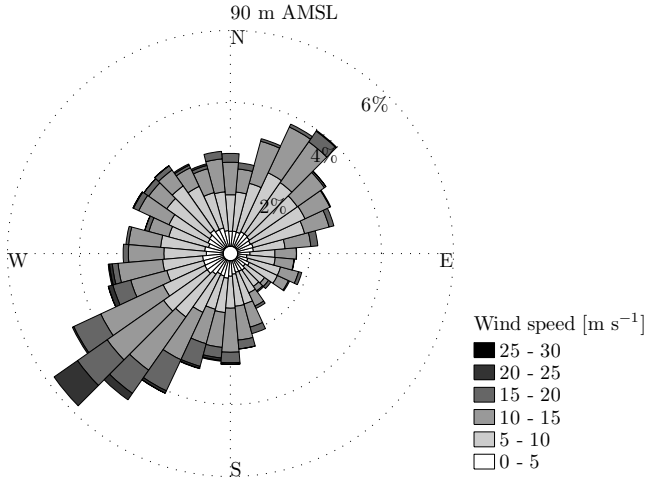

Figure 17: The wind rose at Taqa at 90 m AMSL

The winds at Taqa mainly come from the south-west and north-east sectors (Fig. 17). For the less dominant wind direction, the south-east, the flow might be influenced by the land nearby. The vertical wind speed profiles correspondent to these sectors (5 and 6), where the land is closest to the gas rig (~ 45 km) do not seem to face over/under-speeding due to the roughness change at the coastline (Fig. 18). Simulations carried out with WAsP at the wind

lidar measuring heights reveal a very little over-speeding due to roughness and at all levels this is less than 0.1%.

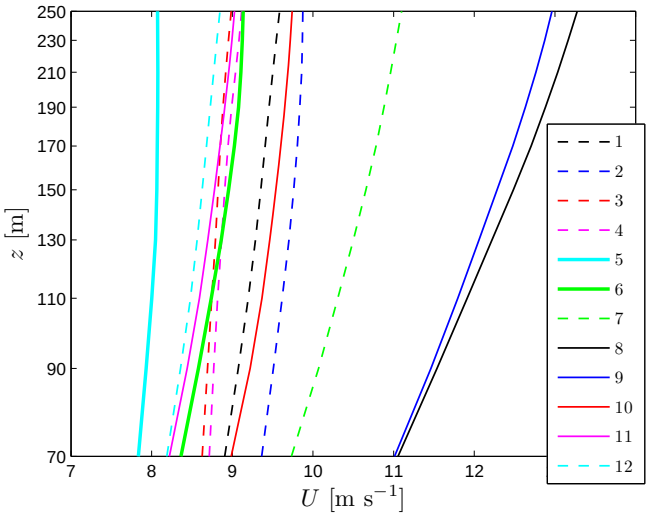

Figure 18: *Mean vertical wind speed profiles per sector at Taqa*

Figure 19 shows the vertical wind shear rose at 100 m AMSL at Taqa. As with the previous two stations, most of the α values are observed in the range 0–0.125 for most of the sectors. For those sectors where the wind is channeled by the English channel (8 and 9), the vertical wind shear slightly increases compared to the long-fetch sectors (11–12).

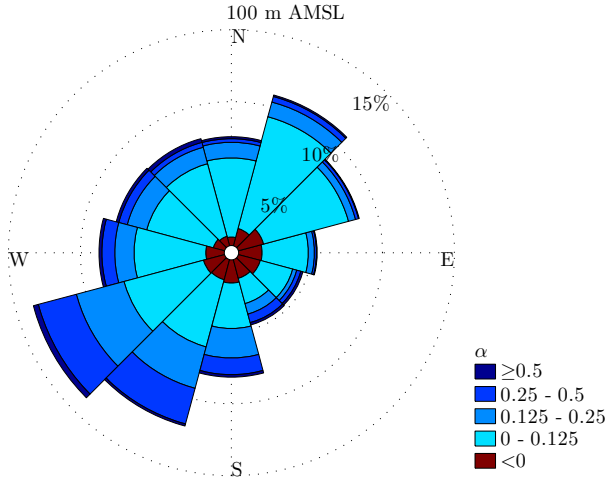

Figure 19: *The vertical wind shear rose at 100 m AMSL at Taqa*

The range of α values for all sectors is shown in Fig. 20. The centroid of the distribution (0.0540) is lower than the theoretical neutral one (0.076), which is a consequence of the relative steep mean vertical wind speed profiles in Fig. 18, where all of them bend upwards. Also vertical wind shear values within the range 0.1–0.3 in Fig. 20 are less frequent compared to the peak value than for the Utsira and Horns Rev II cases.

The diurnal and monthly evolutions of the α-values measured at 100 m AMSL from March 1, 2010, to February 28, 2011, are illustrated in Fig. 21. As shown for the previous two stations, there is very little diurnal variation of α. The seasonal variation does not follow the behavior of the previous stations so well, although α is still higher for the winter months.

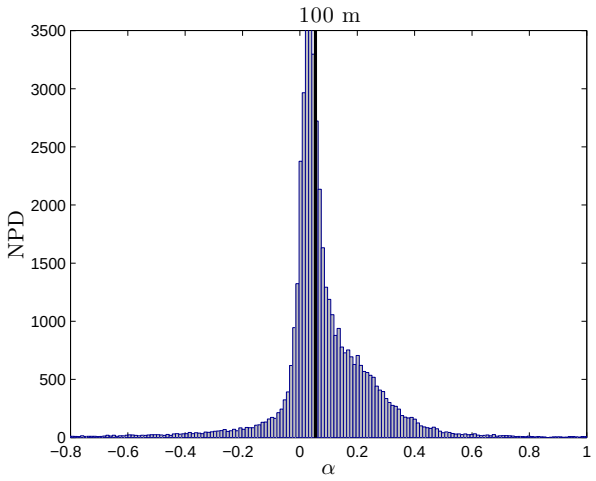

Figure 20: *All-sector distribution of the vertical wind shear at 100 m AMSL at Taqa. The solid black line represents the centroid of the distribution* $\alpha = 0.0540$

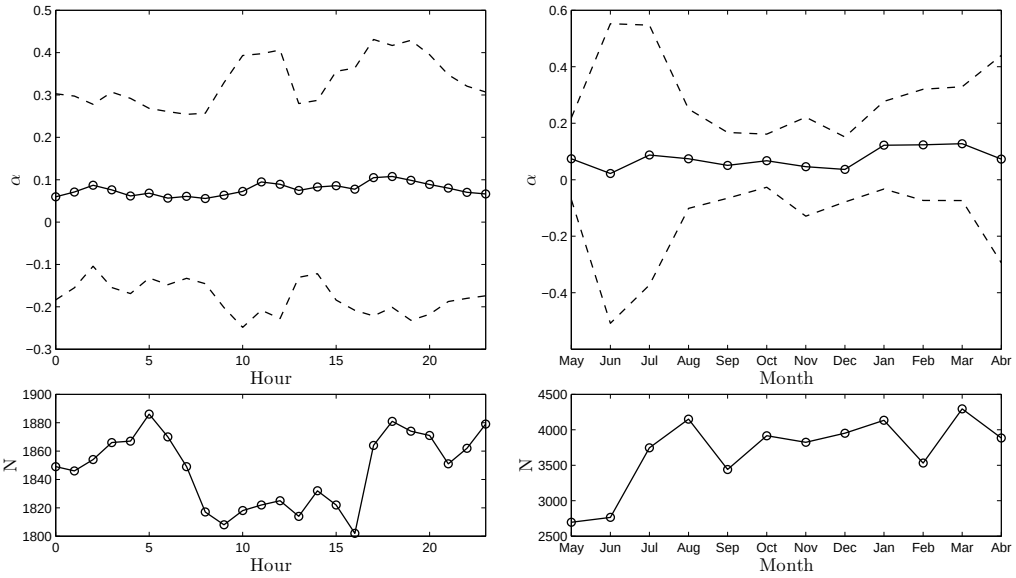

Figure 21: *(top) Diurnal (left) and monthly (right) evolution of the all-sector mean vertical wind shear at 100 m AMSL at Taqa. The dash lines represent the mean±1 standard deviation. (bottom) Number of 10-min measurements used for the calculations on top*

Siri

This wind lidar was placed on the Siri oil platform and is the sensor installed the furthest offshore. The first four measurements are performed at 40, 60, 80 and 100 m ALL. According to the lidar installation report (Kindler, 2010c), the unit was installed at 45 m AMSL. The wind lidar first three measurements are then at 85, 105 and 125 AMSL, thus the wind shear can be estimated at 95 and 115 m AMSL. Assuming that the CFD and wind tunnel results of Stickland et al. (2010) for the Horns Rev II are also valid for the Siri platform, wind lidar measurements performed above 108 m AMSL do not need to be corrected for flow distortion. Therefore, the two first wind lidar measurements might be slightly distorted. However, we do not apply any correction, since these corrections were estimated based on the geometry of the Horns Rev II platform and their implementation at Siri highly increases the uncertainty of the analysis.

The winds at Siri mainly come from the north-west sector and almost no wind coming from

the north-east sector is observed (Fig. 22). However, this wind rose should be interpreted carefully since the amount of available measurements for the months November–May (mainly the winter months) is very low compared to the summer months (see Fig. 25-right bottom). Also as shown in Fig. 25-left bottom the amount of measurements close to and during night times reduces dramatically from that during day times.

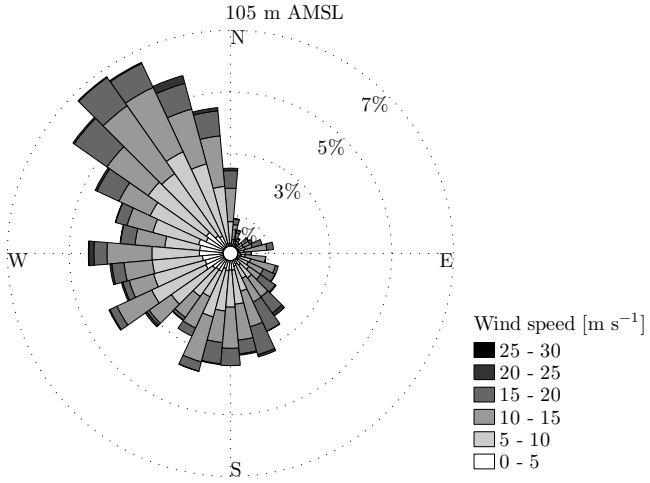

Figure 22: *The wind rose at Siri at 105 m AMSL*

Figure 23 shows the vertical wind shear rose at 95 m AMSL at Siri. Most of the α values are observed in the range 0–0.125 for most of the sectors, as with the previous stations. Interestingly, in sector 12 the amount of values within the range $\alpha < 0$ is large in percentage, which corresponds to that sector pointing to the 'infinite' fetch.

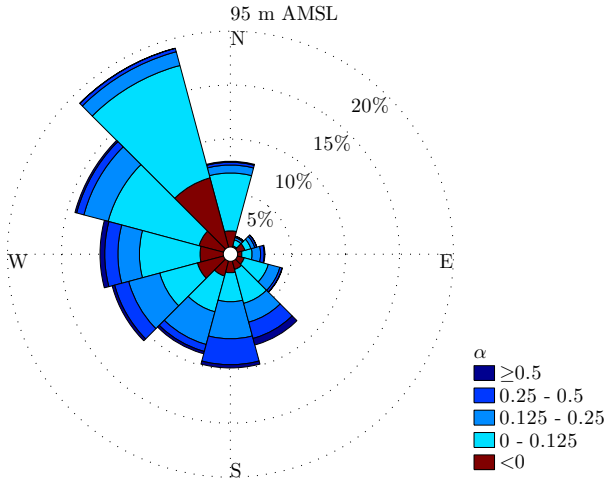

Figure 23: *The vertical wind shear rose at 95 m AMSL at Siri*

The range of α values for all sectors is shown in Fig. 24. The centroid of the distribution (0.0550) is also lower than the theoretical neutral one (0.076), as at Taqa. This is mainly because of the low α values measured within the most predominant wind direction. The distribution of α is however more close to those at Utsira and Horns Rev II.

The diurnal and monthly evolutions of the α-values measured at 95 m AMSL from June 2, 2010, to May 14, 2011, are illustrated in Fig. 25. After May 14, 2011, there is a lack of measurements until middle of June 2011. As shown for the previous stations, there is very little diurnal variation of α, although the amount of measurements during day time is much higher than during night time. The seasonal variation follows the behavior of the Utsira and Horns

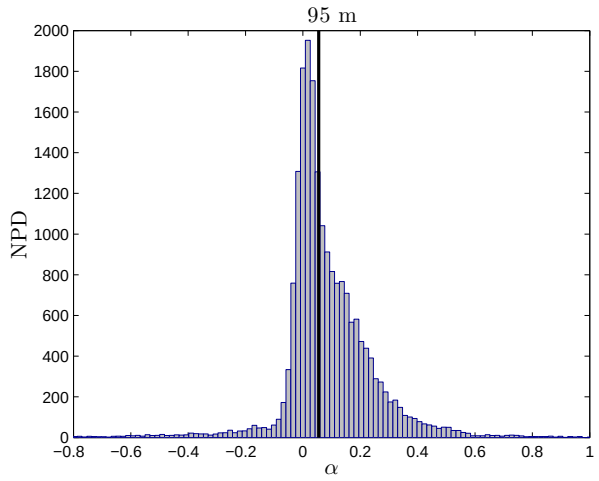

Figure 24: *All-sector distribution of the vertical wind shear at 95 m AMSL at Siri. The solid black line represents the centroid of the distribution* $\alpha = 0.0550$

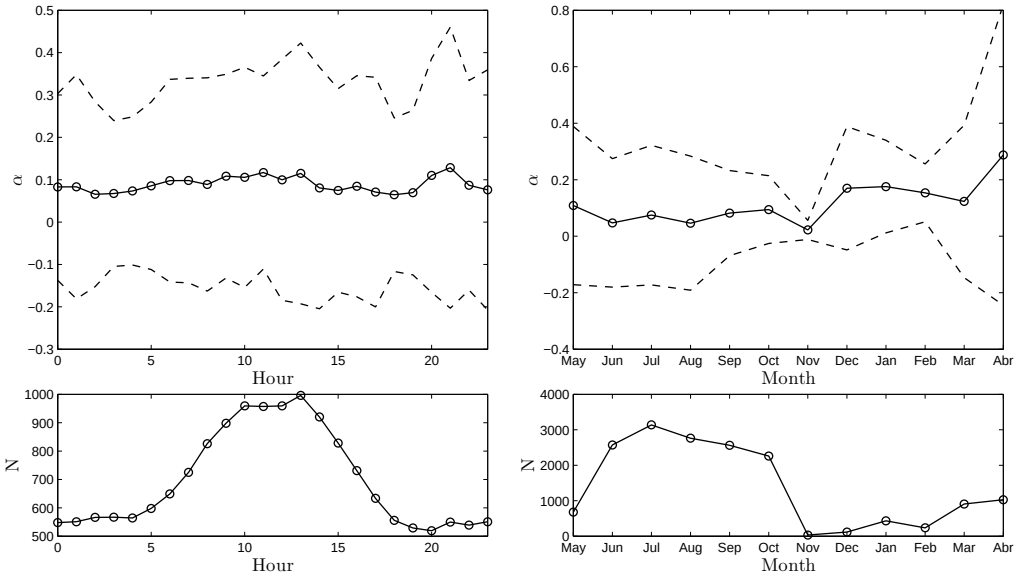

Figure 25: *(top) Diurnal (left) and monthly (right) evolution of the all-sector mean vertical wind shear at 95 m AMSL at Siri. The dash lines represent the mean±1 standard deviation. (bottom) Number of 10-min measurements used for the calculations on top*

Rev stations, where α is lower during the summer than during the winter months. However, at Siri the amount of available observations during the winter months is much lower than during summer months.

Jacky

There is no installation report for this wind lidar. The first four measurements are performed at 40, 60, 80 and 100 m ALL. The unit was installed at ~ 20 m AMSL (Andy Oldroyd, personal communication). The wind lidar first four measurements are then at 60, 80, 100 and 120 m AMSL, thus the wind shear can be estimated at 70, 90 and 110 m AMSL. No corrections are applied to the data, since no study was made on the structure where the unit was deployed. Data are mainly from the months of August and September 2011 because most of the data did not pass the filter requirements (see Section 3).

For these two months mainly, the winds at Jacky come from both the north-west and south-west sector (Fig. 26). However, we cannot be certain on the wind direction measured by the WindCube at Jacky because there is no installation report, which states that the WindCube wind retrieval algorithm corrects for the offset that the unit may have with the true north.

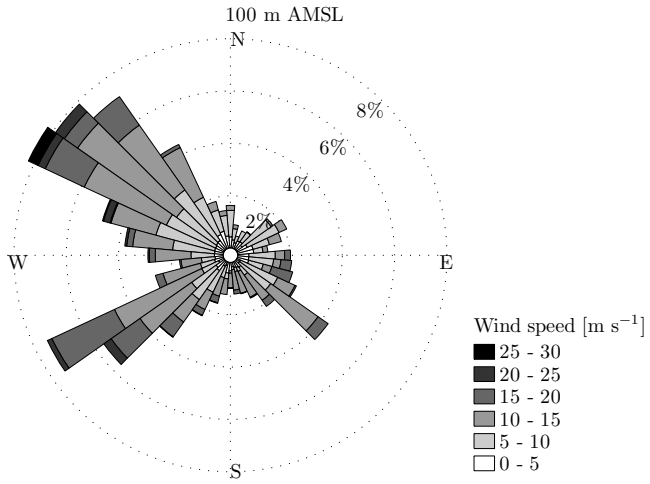

Figure 26: *The wind rose at Jacky at 100 m AMSL for the months of August and September 2011*

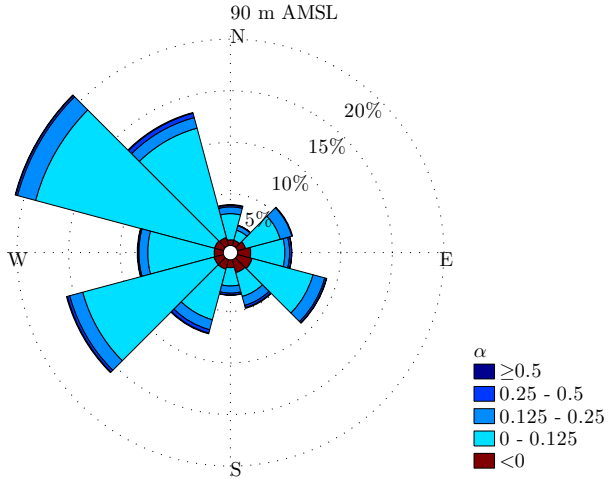

Figure 27: *The vertical wind shear rose at 90 m AMSL at Jacky*

Figure 27 shows the vertical wind shear rose at 90 m AMSL at Jacky. Most of the α values are observed in the range 0–0.125 for most of the sectors, as with the previous stations, and very few values are found below and above this range.

The range of α values for all sectors is shown in Fig. 28, where it is illustrated that the distribution is very similar to the right and to the left of the centroid. The centroid of the distribution (0.0550) is also lower than the theoretical neutral one (0.076), which is expected since the measurements used for the analysis correspond to the months where the water is generally warmer compared to the air temperature and therefore, unstable conditions might prevail (where α values are lower).

No seasonal variation is shown since the amount of data for most of the months is very low. The diurnal evolution of the α-values measured at 90 m AMSL from August 1, 2011, to September 30, 2011, are illustrated in Fig. (29). As shown for the previous stations, there is very little diurnal variation of α.

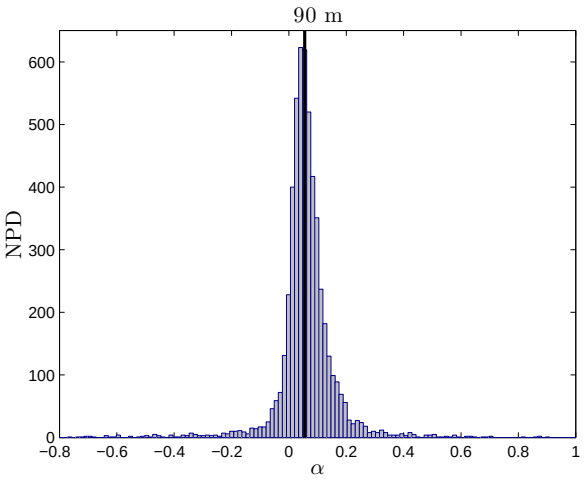

Figure 28: *All-sector distribution of the vertical wind shear at 90 m AMSL at Jacky. The solid black line represents the centroid of the distribution* $\alpha = 0.0550$

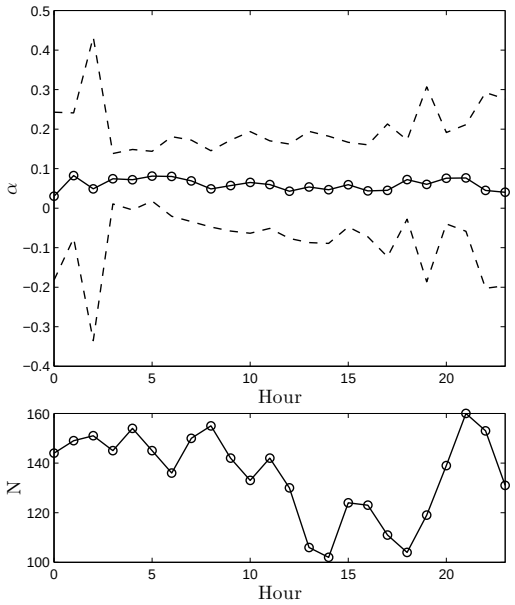

Figure 29: *(top) Diurnal evolution of the all-sector mean vertical wind shear at 90 m AMSL at Jacky. The dash lines represent the mean±1 standard deviation. (bottom) Number of 10-min measurements used for the calculations on top*

Schooner

There is no installation report for this wind lidar either. The first five measurements are performed at 40, 53, 63, 66, and 71 m ALL. The unit was installed at 36 m AMSL (Andy Oldroyd, personal communication). The wind lidar first four measurements are then at 76, 92, 99 and 102 m AMSL, thus the wind shear can be estimated at 84, 95.5 and 100.5 m AMSL. No corrections are applied to the data, since no study was made on the structure where the unit was deployed. The wind lidar data at Schooner do not show the complete year behavior, because there are large data gaps within the months November 2010 to February 2011.

For the eight months of data, the winds at Schooner mainly come from the south-west sector with almost no wind from the other four quadrants (Fig. 30). However, as with the Jacky wind lidar, we cannot be certain on the wind direction measured by this unit because we do not know if the wind retrieval algorithm corrects for any possible installation offset.

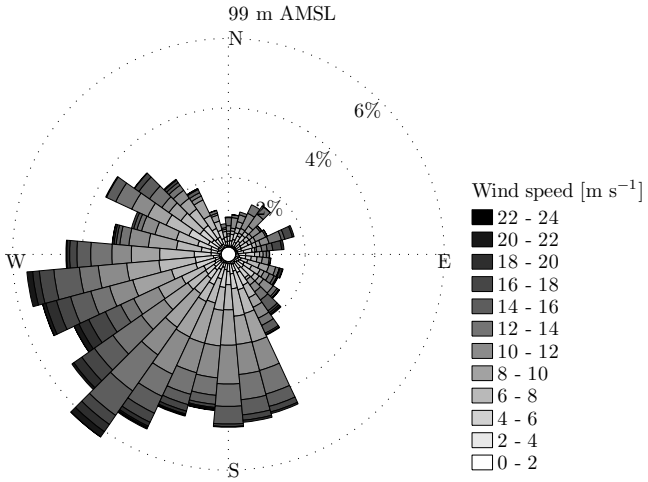

Figure 30: *The wind rose at Schooner at 99 m AMSL*

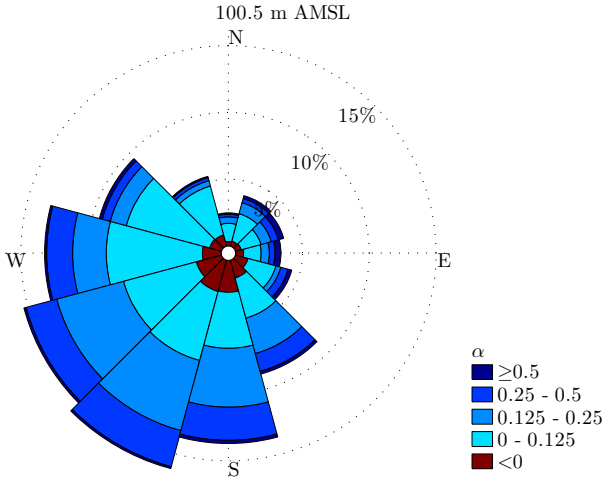

Figure 31: *The vertical wind shear rose at 100.5 m AMSL at Schooner*

Figure 31 shows the vertical wind shear rose at 100.5 m AMSL at Schooner. Relative high α values (above 0.125) are observed on most of the sectors, as well as a significant amount (in percentage) of values above 0.5.

The range of α values for all sectors is shown in Fig. 32. The centroid of the distribution (0.0840) is almost as high as that found at Horns Rev II where most of the wind is affected by the wake of the wind farm. This is mainly because there is a high amount of α values within the range 0.1–0.3.

The diurnal and monthly evolutions of the α-values measured at 100 m AMSL from March 6, 2011, to October 31 2011 are illustrated in Fig. (33). There is little diurnal variation of α, although the variation of the mean is higher compared to the other stations. It is difficult to analyze the seasonal variation, since there are no measurements within the winter months; however, in April, the variability of α is very high compared to the other months as shown in most of the previous stations.

Beatrice

There is no installation report for this wind lidar either. The measurements are performed at 10, 33, 48, 63, and 120 m ALL. The unit was installed at 42.5 m AMSL (Andy Oldroyd, personal communication). The wind lidar first four measurements are then at 52.5, 75.5, 90.5

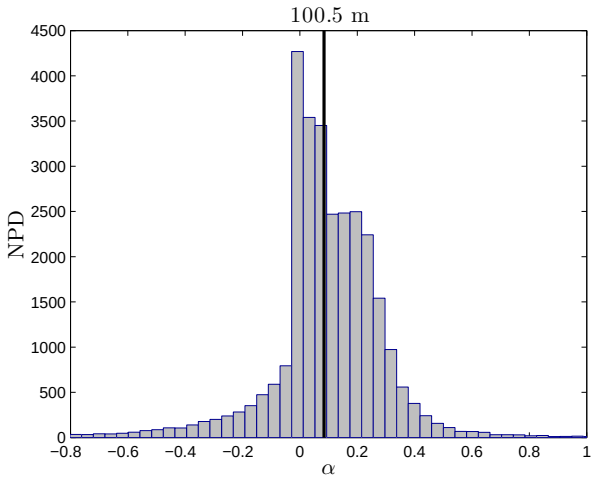

Figure 32: All-sector distribution of the vertical wind shear at 100.5 m AMSL at Schooner. The solid black line represents the centroid of the distribution $\alpha = 0.0840$

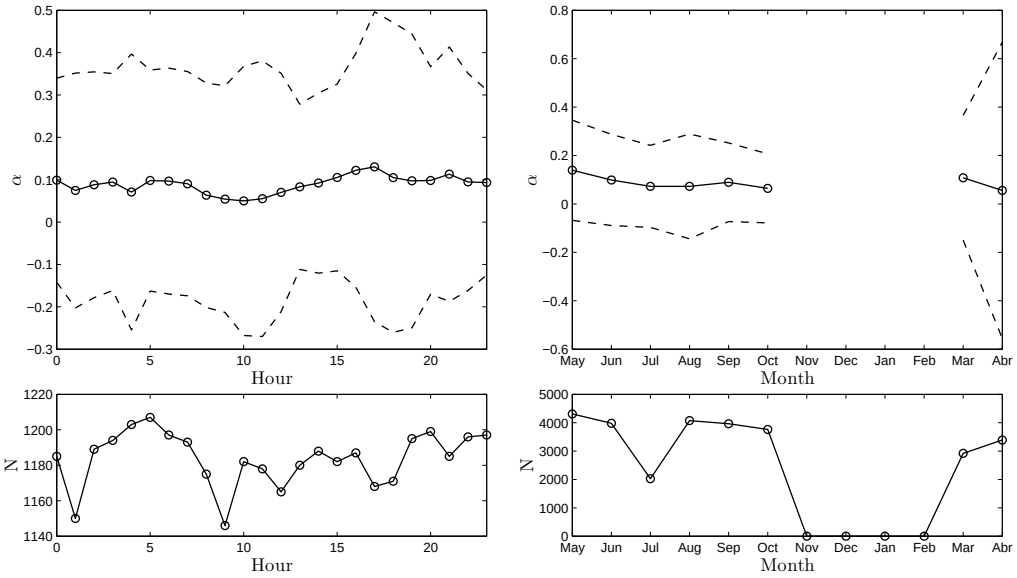

Figure 33: (top) Diurnal (left) and monthly (right) evolution of the all-sector mean vertical wind shear at 100.5 m AMSL at Schooner. The dash lines represent the mean±1 standard deviation. (bottom) Number of 10-min measurements used for the calculations on top

and 105.5 m AMSL, thus the wind shear can be estimated at 64, 83 and 98 m AMSL. No corrections are applied to the data, since no study was made on the structure where the unit was deployed. The wind lidar data at Beatrice only covers four months from November 2010.

The winds at Beatrice mainly come from the north-west and north-east sectors with almost no wind coming from the south-west sector (Fig. 34). However, this wind rose should be interpreted carefully since 1) Only four months are considered and 2) the wind lidar at Beatrice is a ZephIR unit and there might be an ambiguity of 180° in the wind direction retrieval algorithm (Courtney et al., 2008).

Figure 35 shows the vertical wind shear rose at 98 m AMSL at Beatrice. Although, most of the α values are observed in the range 0–0.125 for most of the sectors, as with most of the previous stations, there is a high amount of values in the high (>0.5) and low (<0) ranges. The range of α values for all sectors, shown in Fig. 36, reveals a rather symmetric distribution (around the centroid). The centroid of the distribution (0.0520) is also lower than

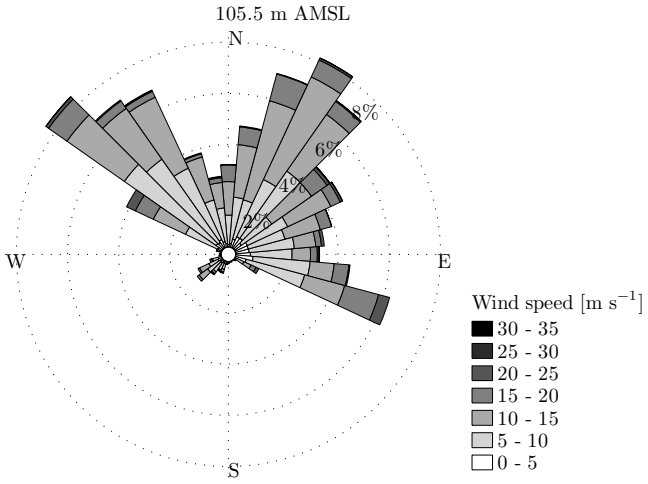

Figure 34: *The wind rose at Beatrice at 105 m AMSL for four months of measurements only*

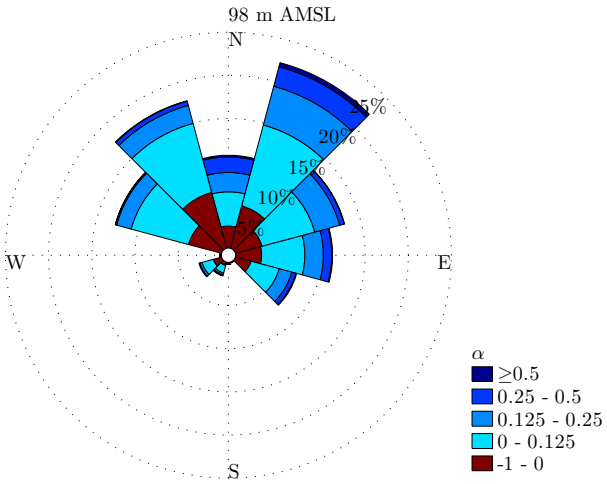

Figure 35: *The vertical wind shear rose at 98 m AMSL at Beatrice for four months of measurements only*

the theoretical neutral one (0.076) as found at most of the nodes where the measurements are not orographically or wake distorted.

The diurnal and monthly evolutions of the α-values measured at 95 m AMSL from November 10, 2010, to February 25, 2011, are illustrated in Fig. 37. After May 14 2011 there is a lack of measurements until middle of June 2011. As shown for the previous stations, there is little diurnal variation of α. Interestingly, for the four months of available data, α highly increases along these winter months as observed at the other stations with sufficient data for the same period.

4.2 Meteorological mast nodes

Three of the meteorological mast nodes from the NORSEWInD network do not observe winds close to or above 100 m. Therefore, for those nodes the analysis is performed at the highest level where vertical wind shear is observed. Also, as shown in Table 1, there is no 'processed' data (i.e. corrected for mast and boom distortion) from most of the met mast nodes, so for those nodes raw data are used. Also the processed and corrected datasets are highly reduced for the nodes at Egmond aan Zee and Fino 1 (those stored in the NORSEWInD database, Table 1) and therefore raw data are also used when possible.

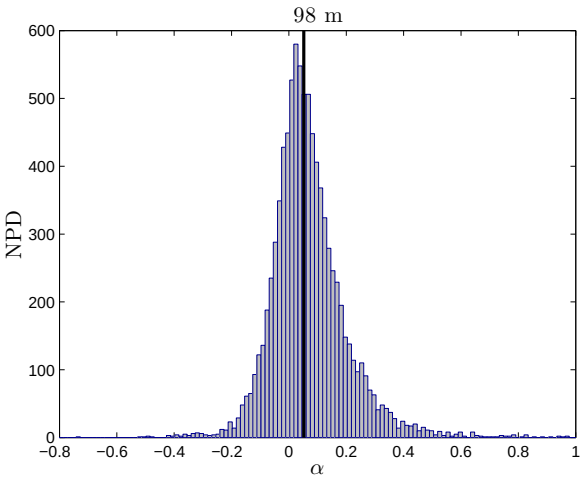

Figure 36: *All-sector distribution of the vertical wind shear at 98 m AMSL at Beatrice. The solid black line represents the centroid of the distribution* $\alpha = 0.0520$

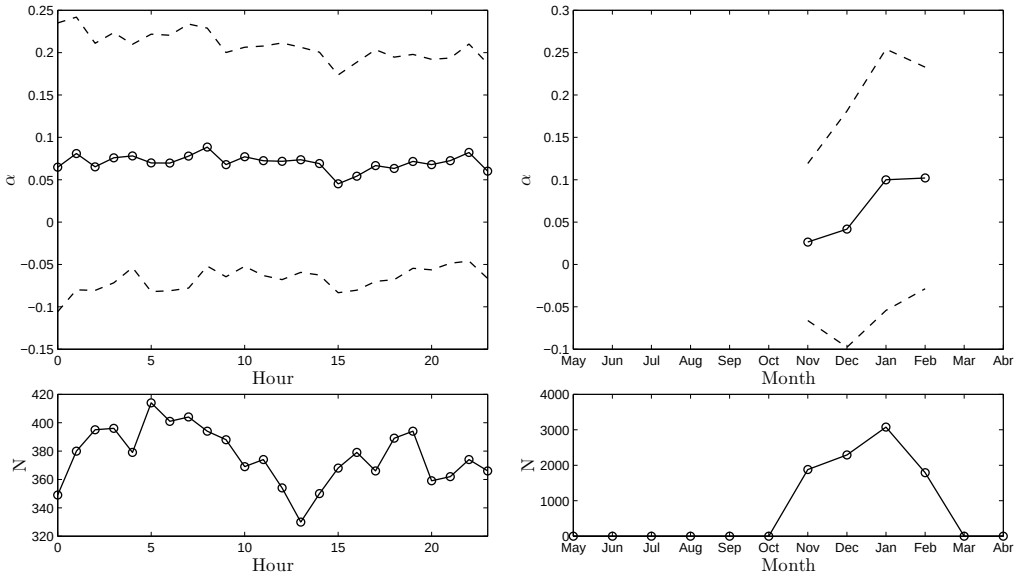

Figure 37: *(top) Diurnal (left) and monthly (right) evolution of the all-sector mean vertical wind shear at 98 m AMSL at Beatrice. The dash lines represent the mean±1 standard deviation. (bottom) Number of 10-min measurements used for the calculations on top*

M7 – Horns Rev I

Based on the highest levels where wind speed measurements are available at the mast (50, 60 and 70 m AMSL), α is derived at 55 and 65 m AMSL.

The winds at M7 mainly come from the west sectors with almost no wind coming from the north-east sector (Fig. 38). This means that most of the wind is wake affected by the Horns Rev I wind farm and thus the wind shear measured at 55 and 65 m AMSL will be closed to the hub height of the turbines and assuming that the center of the wake is kept at hub height, the observed wind shears are lower than those for non-wake sectors.

Figure 39 shows the vertical wind shear rose at 55 m AMSL at M7. We do not use the values observed at 65 m AMSL because from these data, as well as from previous studies (Peña et al., 2009), the 70 m wind speed measurement (performed by a cup anemometer on a pole) systematically shows a higher wind speed compared to the extrapolated 70 m value using the lower measurement levels. This results in unrealistic high vertical wind shear values

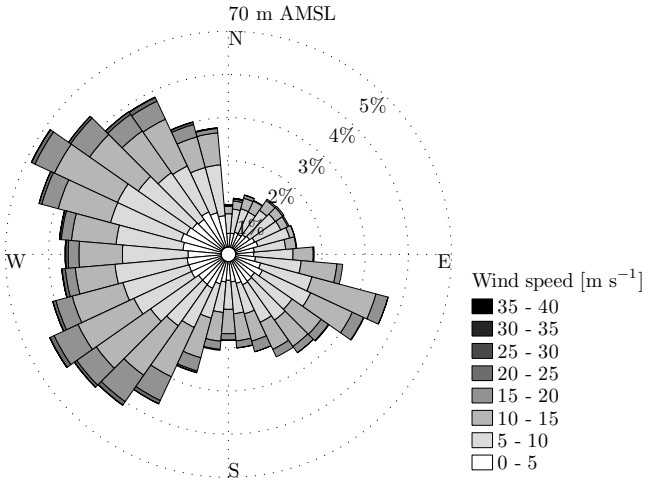

Figure 38: *The wind rose at M7 at 70 m AMSL*

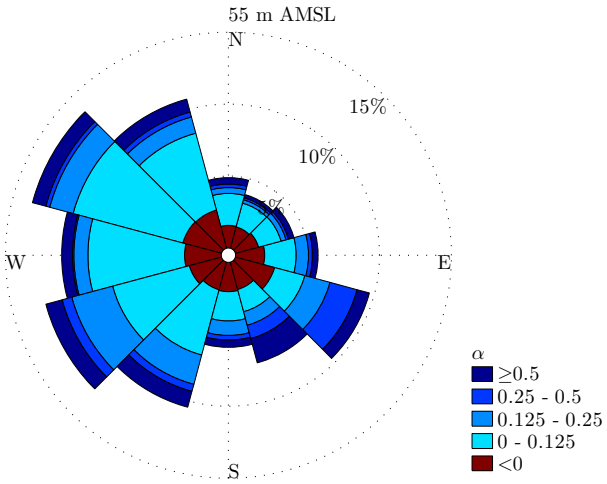

Figure 39: *The vertical wind shear rose at 55 m AMSL at M7*

and is a consequence of underprediction of the wind speed of the low levels and overprediction of the pole measurements. Most of the α values are observed in the range 0–0.125 for most of the sectors, as with most of the previous stations.

The range of α values for all sectors, shown in Fig. 40, also reveals a symmetric distribution (around the centroid). The centroid of the distribution (0.0480) is much lower than the theoretical neutral one (0.080) as expected from the wake deficit of the wind farm.

The diurnal and monthly evolutions of the α-values measured at 55 m AMSL from January 1, 2004, to December 15, 2009, are illustrated in Fig. (41). As shown, the uncertainty in both diurnal and monthly evolutions is too high, due mainly to extreme positive and negative values of α. The uncertainty is however higher for the winter than for the summer period, as expected.

Greater Gabbard

The meteorological mast at Greater Gabbard measures winds using cup anemometers located on booms at 315° and 135° up to 82.5 m AMSL. The measurement at 86.5 m AMSL is probably performed on a pole but there is no report on the mast to confirm this. A preliminary analysis of the mast measurements reveals that the measurements performed on the boom at 135° are systematically different to those performed at 315°. The variability of estimated

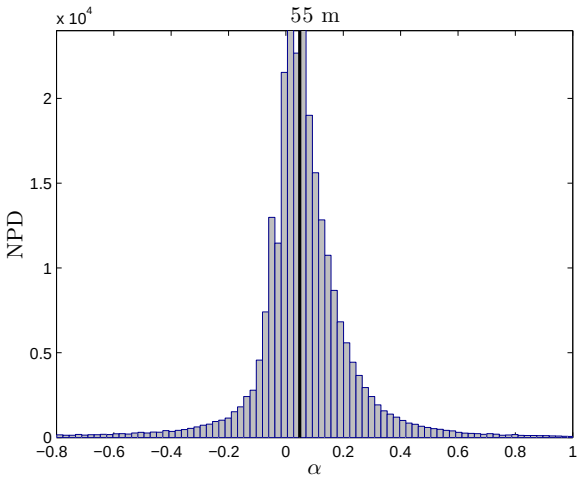

Figure 40: All-sector distribution of the vertical wind shear at 55 m AMSL at M7. The solid black line represents the centroid of the distribution $\alpha = 0.0480$

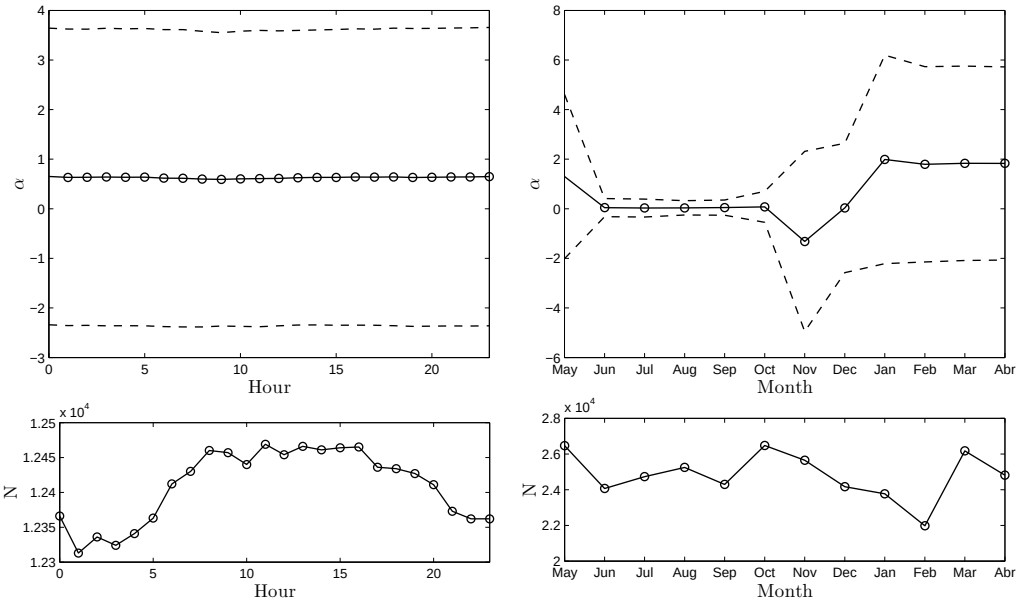

Figure 41: (top) Diurnal (left) and monthly (right) evolution of the all-sector mean vertical wind shear at 55 m AMSL at M7. The dash lines represent the mean±1 standard deviation. (bottom) Number of 10-min measurements used for the calculations on top

vertical wind shears from the measurements at 135° is unrealistically high and therefore we decide to use those at 315° only. As at M7 at Horns Rev I, the pole measurements at 86.5 m AMSL are systematically and unrealistically higher compared to those extrapolated from the lower measurement levels. Therefore, α is here estimated at 77.5 m (between the two measurement levels on the booms at 315°).

The winds at Greater Gabbard mainly come from the south-west sectors (Fig. 42), similar to those measured by the wind lidar at Schooner.

Figure 43 shows the vertical wind shear rose at 77.5 m AMSL at Greater Gabbard. For all sectors, half of the α values are within the range 0–0.125 and there is a high amount of values in the low range (<0).

The range of α values for all sectors is shown in Fig. 44. The distribution is not symmetric around the centroid, as found at most of the stations. The centroid of the distribution (0.1220) is also higher, as at the Schooner node, than the theoretical neutral one (0.077)

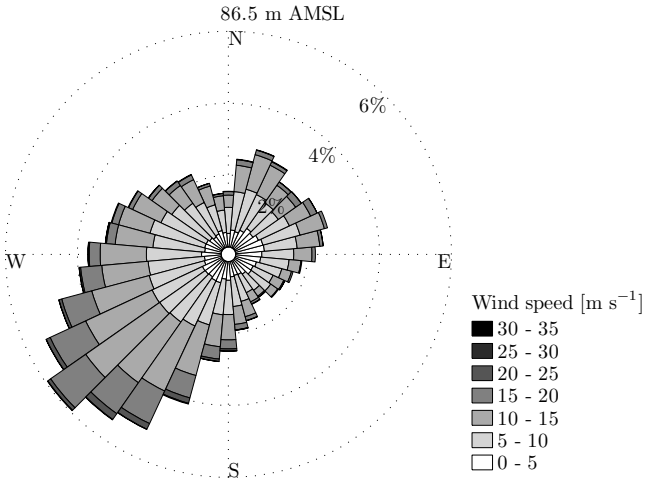

Figure 42: *The wind rose at Greater Gabbard at 86.5 m AMSL*

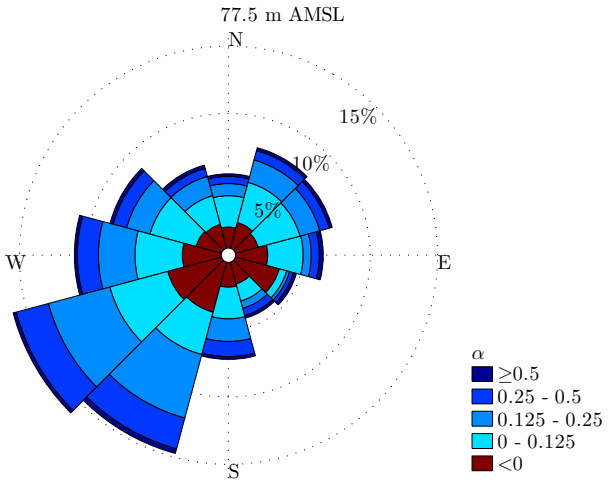

Figure 43: *The vertical wind shear rose at 77.5 m AMSL at Greater Gabbard*

The diurnal and monthly evolutions of the α-values measured at 77.5 m AMSL from February 1, 2006, to January 31, 2010, are illustrated in Fig. 45. The uncertainty in both diurnal and monthly evolutions is too high, similar to the findings at the M7 mast, and an attempt to plot the results with a much lower range of α values, like those at the wind lidar nodes, does not reveal any clear diurnal or seasonal evolution.

Lillgrund

Based on the highest levels where wind speed measurements are available at the mast (40, 63 and 65 m AMSL), α is derived at 51.5 and 64 m AMSL. The winds at Lillgrund are rather evenly distributed along the wind sectors as observed from Fig. 46, except from the north sector where no winds are measured. There are two measurement levels for wind direction at Lillgrund (18 and 61 m AMSL) and for both time series the wind rose does not show northerly winds. We do not have information related to the placement of the wind vanes at the met mast at Lillgrund but such a lack of winds might be an artifact of the measurements.

The met mast at Lillgrund is located south west of the Lillgrund wind farm and thus winds from the directions 345–100° will be affected by the wake of the wind farm. The wind shear measured at 51.5 and 64 m will be affected by the low wind shear from the wake of the wind turbines which will have its center around hub height.

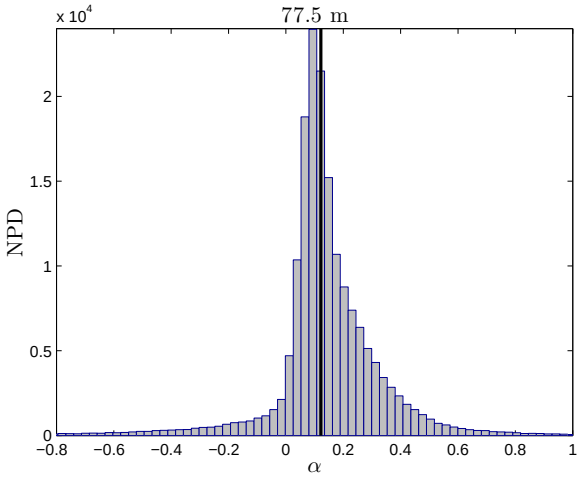

Figure 44: All-sector distribution of the vertical wind shear at 77.5 m AMSL at Greater Gabbard. The solid black line represents the centroid of the distribution $\alpha = 0.1220$

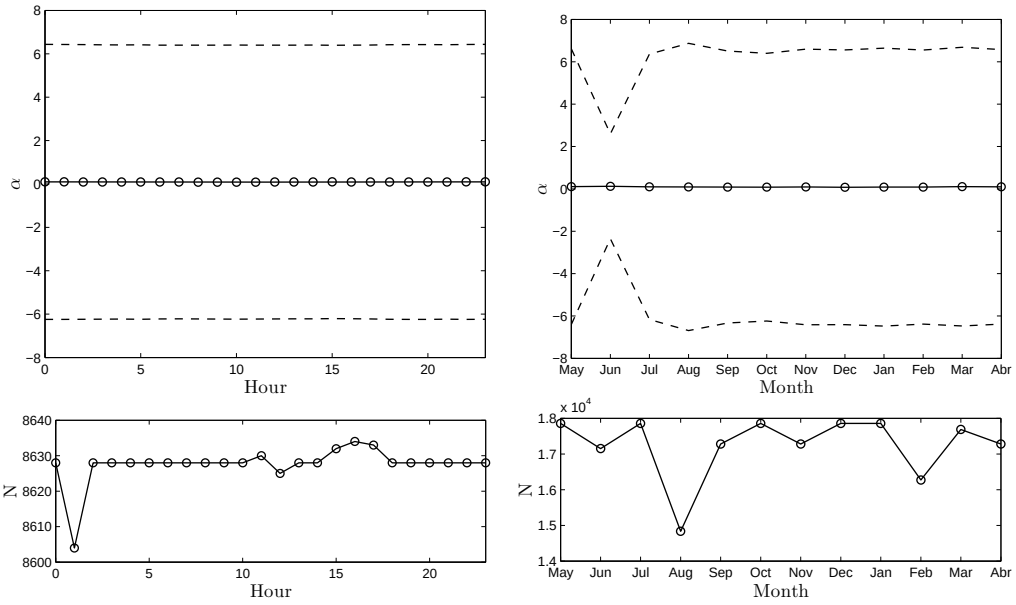

Figure 45: (top) Diurnal (left) and monthly (right) evolution of the all-sector mean vertical wind shear at 77.5 m AMSL at Greater Gabbard. The dash lines represent the median±1 standard deviation. (bottom) Number of 10-min measurements used for the calculations on top

Figure 47 shows the vertical wind shear rose at 51.5 m AMSL at Lillgrund. We do not use the values observed at 64 m AMSL because from these data, the 65 m wind speed measurement (performed by a cup anemometer on a pole) systematically shows a higher wind speed compared to the extrapolated 65 m value using the lower measurement levels (very similar to the findings at M7). Most of the α values are observed in the range 0–0.125 for all the non-wake affected sectors, as with most of the previous stations, and those wake affected clearly show a good number of negative wind shear values.

The range of α values for all sectors, shown in Fig. 48, also reveals a symmetric distribution (around the centroid). The centroid of the distribution (0.0550) is much lower than the theoretical neutral one (0.080) as expected from the large number of measurements which are wake-affected by the wind farm.

The diurnal and monthly evolutions of the α-values measured at 51.5 m AMSL from January

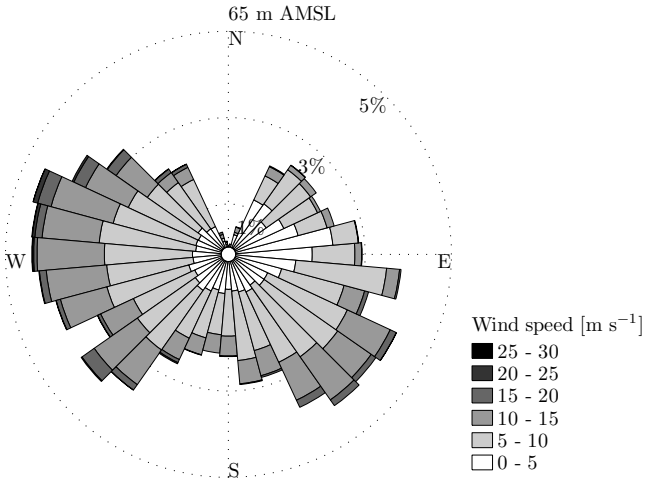

Figure 46: The wind rose at Lillgrund at 65 m AMSL

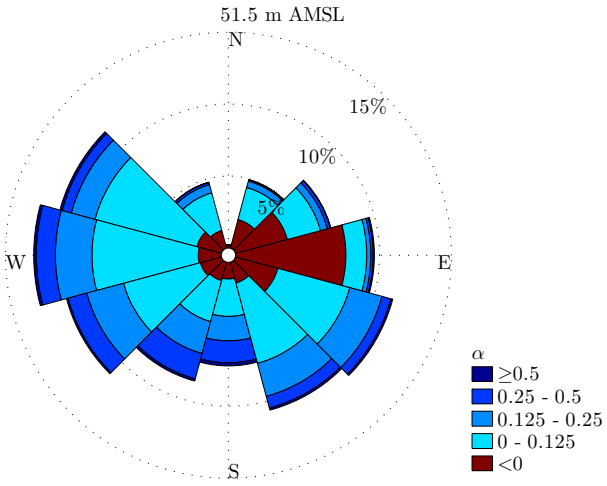

Figure 47: The vertical wind shear rose at 51.5 m AMSL at Lillgrund

1, 2009, to December 31, 2009, are illustrated in Fig. (49). As shown, the uncertainty in both diurnal and monthly evolutions is high, due mainly to extreme positive and negative values of α (for this case we have chosen to use the results for the cup anemometers located on booms at 360° since they show the lowest uncertainty). There is no clear evidence of systematic diurnal or monthly variation of the vertical wind shear. The uncertainty however is clearly highest in spring and lowest in autumn..

Høvsøre

Wind speed measurements are available from cup anemometers located on booms at 180°. The highest wind speed measurement is located at 116.5 m and corresponds to a pole measurement. Here, we do not use this measurement since it is not 'aligned' with the other lower cup measurements and thus might experience a different mast effect. The highest levels where wind speed measurements are available at the mast are therefore at 80 and 100 m AGL, so α is derived at 70 and 90 m AGL.

The winds at Høvsøre mainly come from the west, although there is a good number of winds coming from south-east (Fig. 50). Almost no wind comes from the north sector where turbines are tested at Høvsøre (see Fig. 51). Also from the map of Høvsøre, it can be seen that the wind is influenced by the North Sea, west of the meteorological mast and that it is

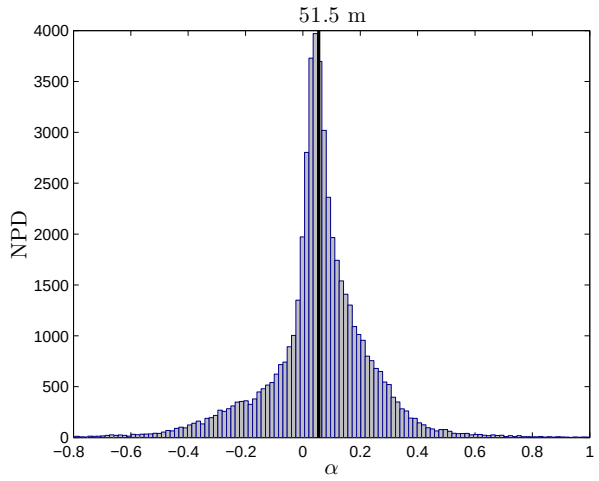

Figure 48: *All-sector distribution of the vertical wind shear at 51.5 m AMSL at Lillgrund. The solid black line represents the centroid of the distribution* $\alpha = 0.0550$

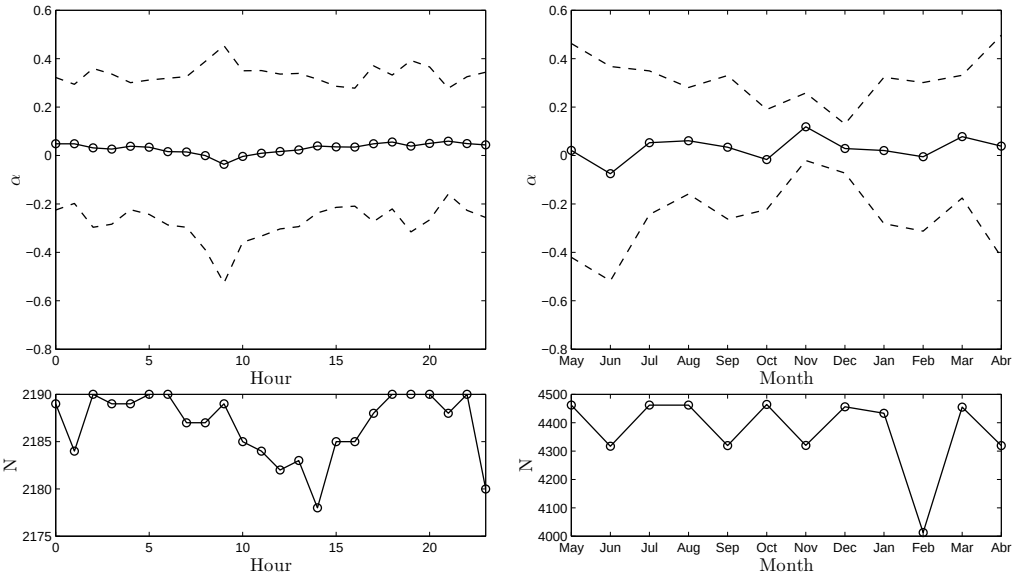

Figure 49: *(top) Diurnal (left) and monthly (right) evolution of the all-sector mean vertical wind shear at 51.5 m AMSL at Lillgrund. The dash lines represent the mean±1 standard deviation. (bottom) Number of 10-min measurements used for the calculations on top*

relatively flat and homogenous for the east 'land' sector (30–125°).

Figure 52 shows the vertical wind shear rose at 90 m AMSL at Høvsøre. Most of the α values are observed in the range 0–0.125 for all the 'sea' sectors and in the range 0.25–0.50 for all the 'land' sectors. This is mainly due to the surface properties at Høvsøre; for the west sector the roughness length of the vertical wind speed profile is lowest, thus predicting low values of vertical wind shear, whereas for the more rough terrain and higher roughness length within the land sector, the vertical wind shear is higher.

We will concentrate this analysis on the east 'land' sector, as mean to compare all other offshore nodes' results with 100% onshore winds observed at Høvsøre. Also, winds coming from the west combine the effect of the new land surface and the marine boundary layer (MBL) further upstream (Floors et al., 2011). The range of α values for the land sectors, shown in Fig. 53, also reveals a relative symmetric distribution (around the centroid). The centroid of the distribution (0.228) is higher than the theoretical neutral value obtained

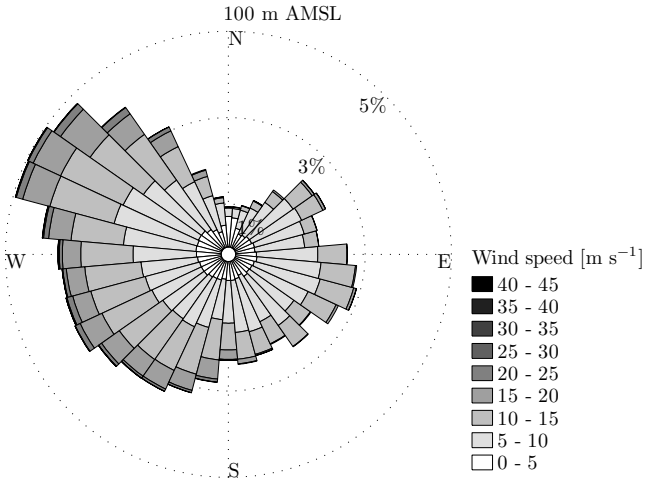

Figure 50: *The wind rose at Høvsøre at 100 m AGL*

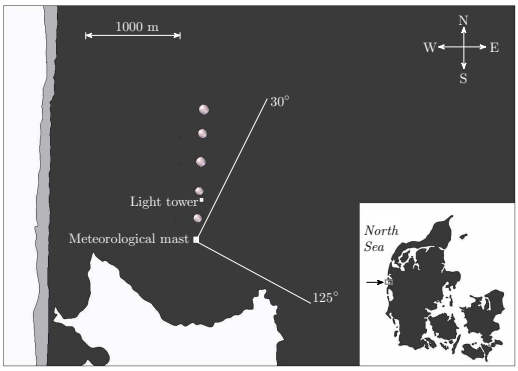

Figure 51: *The meteorological mast at the Høvsøre test station in Denmark*

assuming $z_o = 0.016$ as in (Peña, 2009) (0.120). This is expected, since for this land sector low-level jets and BLHs can be observed relatively low in the atmosphere and the wind profile experiences a high wind shear around 80–100 m under stable atmospheric conditions (Peña et al., 2010a,b).

The diurnal and monthly evolutions of the α-values measured under the land east sector at 90 m AMSL from January 1, 2005, to December 31, 2011, are illustrated in Fig. 54. As shown, the uncertainty in both diurnal and monthly evolutions is high and rather constant. There is a substantial difference between the diurnal behavior found at Høvsøre compared to those of the other offshore stations; at Høvsøre, the vertical wind shear is clearly highest in the early morning and night times and lowest during the daytime. This is expected as for this wind sector the winds come from the land and the land surface rapidly experiences the changes in temperature during the day from solar irradiation which results in many convective situations (with low vertical wind shears around noon) and many stable conditions (with high vertical wind shear values) during nightime from the cooling of the ground surface. The monthly evolution does not show any distintive variation, although May and June months show slightly lower vertical wind shears than the other months. This is because at Høvsøre at any time of the year, it is possible to observe a good amount of stable and unstable situations within this land sector.

Fino 1

In this analysis we work with the raw data from Fino 1, since the amount of 'corrected' data is too low. Based on the highest levels where wind speed measurements are available at the

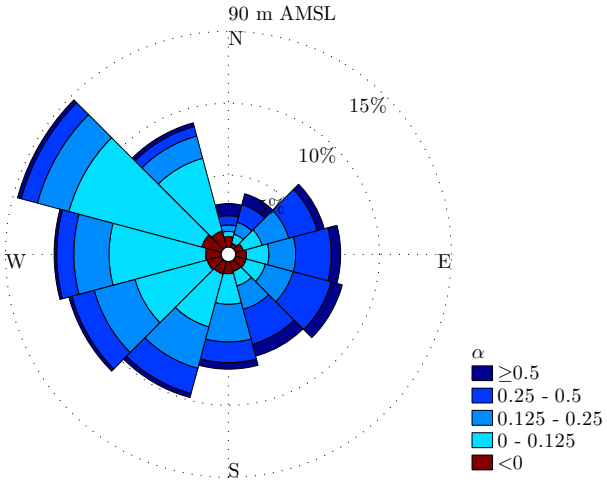

Figure 52: *The vertical wind shear rose at 90 m AGL at Høvsøre*

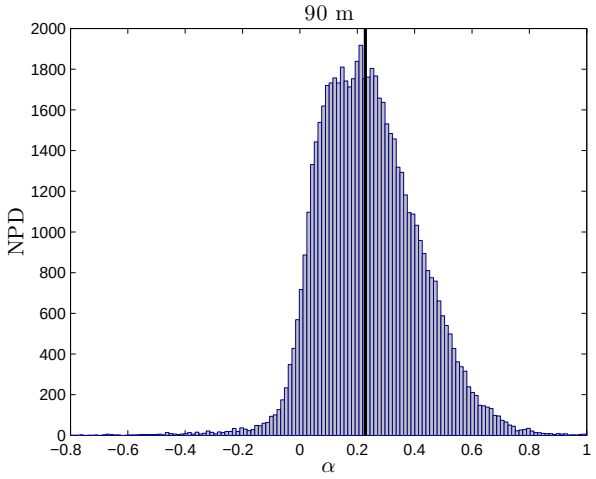

Figure 53: *Land-sector distribution of the vertical wind shear at 90 m AGL at Høvsøre. The solid black line represents the centroid of the distribution* $\alpha = 0.2280$

mast (80, 90 and 100 m AMSL), α is derived at 85 and 95 m AMSL.

According to the wind rose from the measurements in the NORSEWInD database, the winds at Fino 1 mainly come from the south-west sectors with almost no wind coming from the east sectors (Fig. 55). This is not an effect of the wake of the Alpha Ventus wind turbines east of the Fino 1 platform as they were erected in 2009 and the measurements here analyzed are until 2007. The nearly lack of wind directions at all measurement heights on some east sectors does not seem to be realistic and might be an artifact of the measurements. We do know that the wind speed and direction measurements at Fino 1 experience severe flow distortion due to the mast and boom structure and the helipad platform.

Figure 56 shows the vertical wind shear rose at 85 m AMSL at Fino 1. We do not use the values observed at 95 m AMSL because an a priori analysis revealed a totally unrealistic range of α values. As mentioned, at Fino 1 the effect of the mast structure on the measurements is very severe and wind shear computations, which require two wind speed measurements become even more affected. Further, the wind speed measurement at 100 m AMSL faces a much different distortion of the mast, since the cup anemometer is within a rod cage. The other cup anemometers might be more distorted than the 100-m one, but the effect of the mast on them is relatively similar. Although, the effect is similar for the side-mounted cup anemometers, the vertical wind shear values might become too positive or negative, as it is

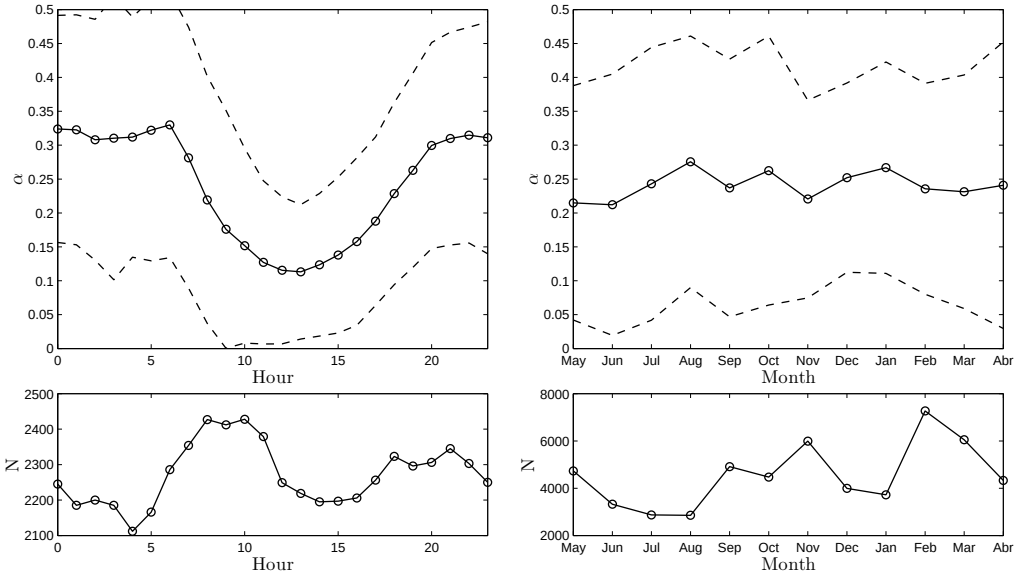

Figure 54: (top) Diurnal (left) and monthly (right) evolution of the land-sector mean vertical wind shear at 90 m AGL at Høvsøre. The dash lines represent the mean±1 standard deviation. (bottom) Number of 10-min measurements used for the calculations on top

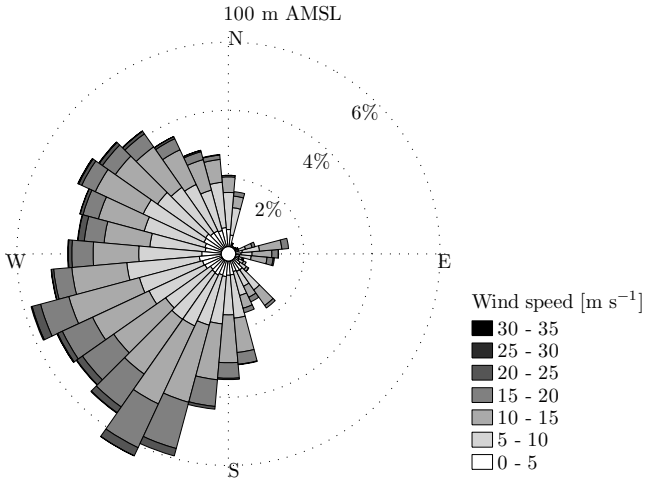

Figure 55: The wind rose at Fino 1 at 100 m AMSL

shown for sector 11 in Fig. 56. Most of the α values are observed in the range 0–0.125 for most of the sectors, as with most of the previous offshore stations.

The range of α values for all sectors, shown in Fig. 57, also reveals a symmetric distribution (around the centroid), but in this case it is evident the large number of very positive and negative α values. The centroid of the distribution (0.065) is slightly lower than the theoretical neutral one (0.077).

The diurnal and monthly evolutions of the α-values measured at 85 m AMSL from January 1, 2004, to December 31, 2006, are illustrated in Fig. (58). As shown, there is no distinct diurnal variation of α and its uncertainty is rather constant. α does not seem to highly vary on a monthly basis and only the variation in uncertainty is evident; highest in spring and lowest in autumn.

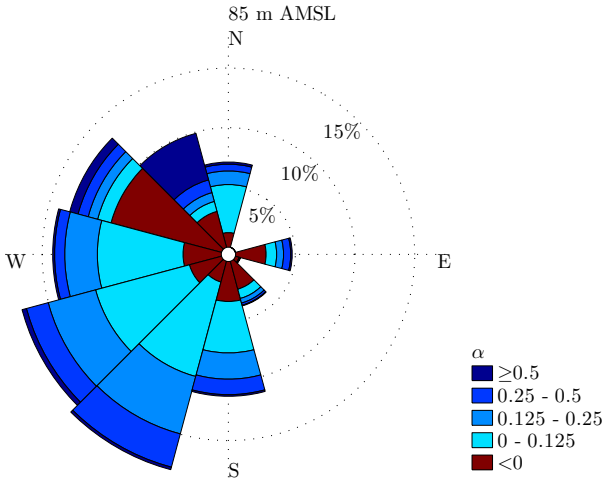

Figure 56: *The vertical wind shear rose at 85 m AMSL at Fino 1*

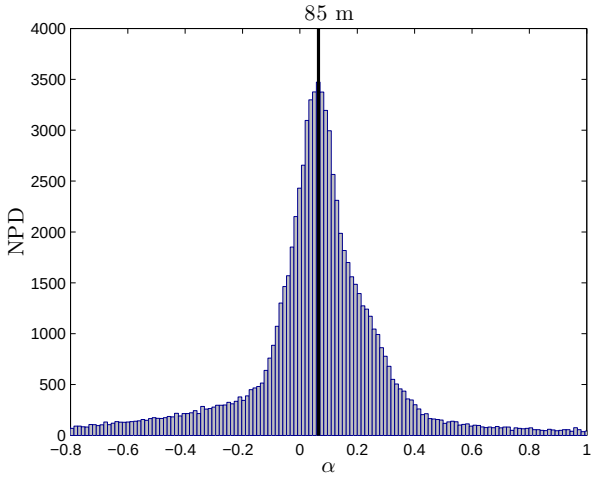

Figure 57: *All-sector distribution of the vertical wind shear at 85 m AMSL at Fino 1. The solid black line represents the centroid of the distribution* $\alpha = 0.0650$

Fino 2

In this analysis we also work with the raw data from Fino 2. Based on the highest levels where wind speed measurements are available at the mast (82, 92 and 102 m AMSL), α is derived at 87 and 97 m AMSL.

The winds at Fino 2 mainly come from the west and east sectors with few winds from the north and south (Fig. 59). The same behavior for the wind rose has been observed from another set of data at Fino 2 and from simulations performed with the advanced weather research and forecasting (WRF) model (Peña et al., 2011). As for Fino 1, the measurements at Fino 2 experience severe flow distortion due to the mast and boom structure.

Figure 60 shows the vertical wind shear rose at 87 m AMSL at Fino 2. We do not use the values observed at 97 m AMSL because an a priori analysis revealed an unrealistic range of α values, as for the highest vertical wind shear measurement at Fino 2. As mentioned, at Fino 2 the effect of the mast structure on the measurements is also severe. The wind speed measurement at the highest level (102 m AMSL) is not 'aligned' with those at the lower levels and over-predicts the wind speed compared to the extrapolated value using the lower heights (Peña et al., 2011). The vertical wind shear rose at 87 m reveals most of the observations within the range 0–0.125, except for the north sector.

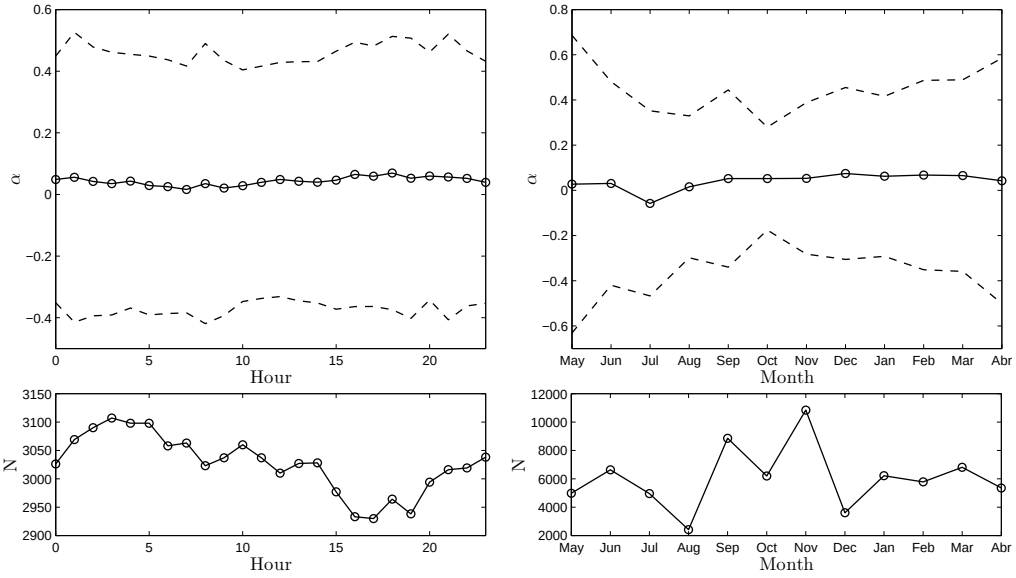

Figure 58: (top) Diurnal (left) and monthly (right) evolution of the all-sector mean vertical wind shear at 85 m AMSL at Fino 1. The dash lines represent the mean±1 standard deviation. (bottom) Number of 10-min measurements used for the calculations on top

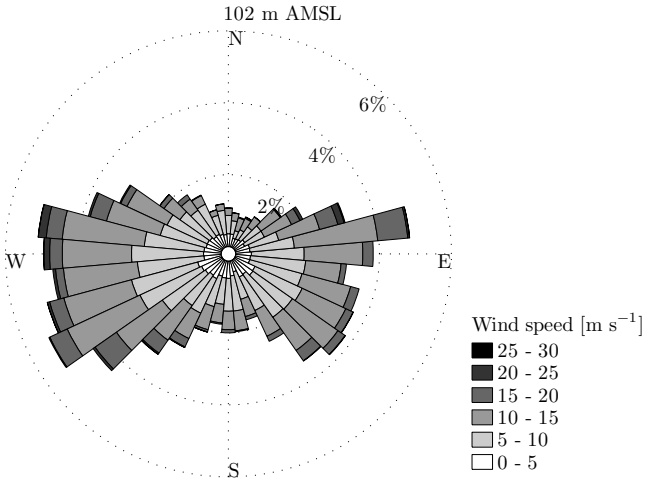

Figure 59: The wind rose at Fino 2 at 102 m AMSL

The range of α values for all sectors, shown in Fig. 61 does not reveal a symmetric distribution, but rather one close to those observed at most wind lidar nodes. The amount of very positive and negative α values is very high (although much lower when compared to the 97 m values). The centroid of the distribution (0.075) is nearly the same theoretical neutral one (0.077).

The diurnal and monthly evolutions of the α-values measured at 87 m AMSL from May 1, 2008, to April 30, 2010, are illustrated in Fig. 62. As illustrated, there is no distinct diurnal variation of α and its uncertainty is rather constant. α does not seem to highly vary on a monthly basis and only the variation in uncertainty is evident; highest in late spring and lowest in late autumn, as for Fino 1, although the amount of measurements in both periods is high and low, respectively.

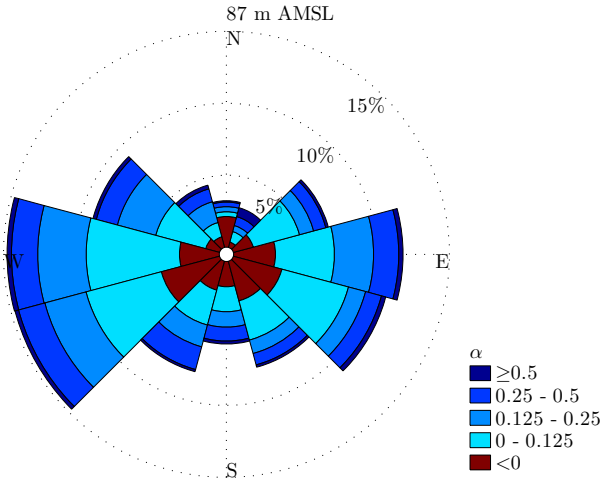

Figure 60: *The vertical wind shear rose at 87 m AMSL at Fino 2*

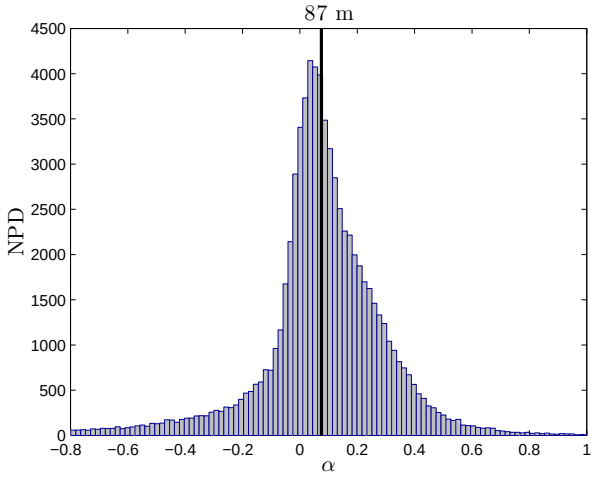

Figure 61: *All-sector distribution of the vertical wind shear at 87 m AMSL at Fino 2. The solid black line represents the centroid of the distribution* $\alpha = 0.0750$

Egmond aan Zee

For this analysis we also work with the raw data from Egmond aan Zee, since the amount of 'processed' data is 20 times lower than the raw data (Table 1). Based on the three different levels where wind speed measurements are available at the mast (21, 70 and 116 m AMSL), α is derived at 45.5 and 93 m AMSL. Egmond aan Zee is the only of the met mast here analyzed where there are redundant instruments at all levels. For the wind speed measurements, there are three cup anemometers separated each other 120°. For each 10-min in the time series, we select the cup anemometer, which faces the lowest mast distortion based on the findings of Sathe (2009).

The winds at Egmond aan Zee mainly come from the south east with few winds from the north and south east (Fig. 63), in accordance to the findings by Sathe et al. (2011) using data from the mast for another period. The met mast at Egmond aan Zee is located west of the Egmond aan Zee wind farm and the measurements are then affected by the wake of the wind farm (from the moment the wind farm started to operate, i.e. about October 2006, whereas the NORSEWInD database covers measurements from July 2005 to December 2012).

Figure 64 shows the vertical wind shear rose at 93 m AMSL at Egmond aan Zee. As observed for most wind lidar nodes, the largest amount of α values is found between the

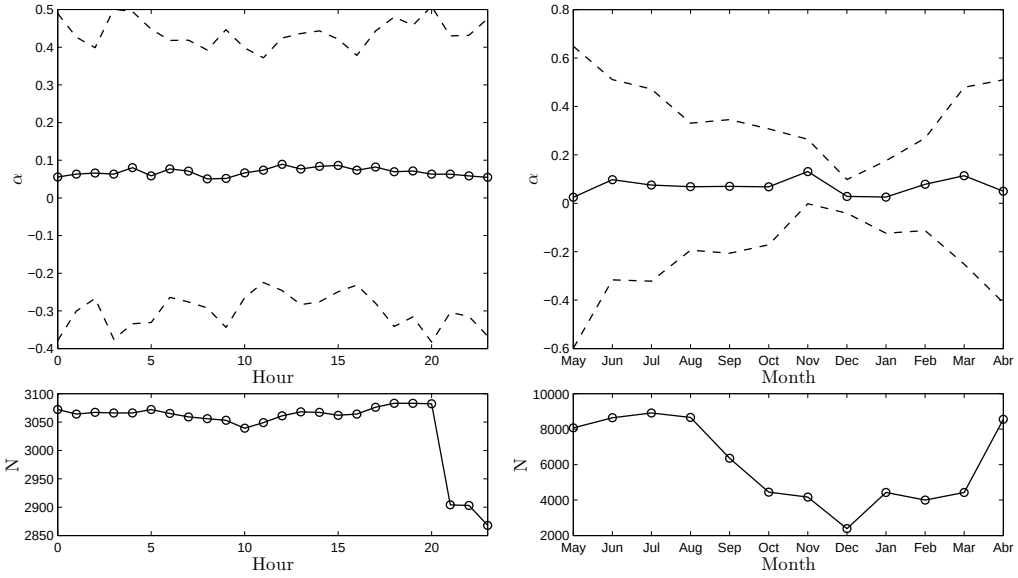

Figure 62: (top) Diurnal (left) and monthly (right) evolution of the all-sector mean vertical wind shear at 87 m AMSL at Fino 2. The dash lines represent the mean±1 standard deviation. (bottom) Number of 10-min measurements used for the calculations on top

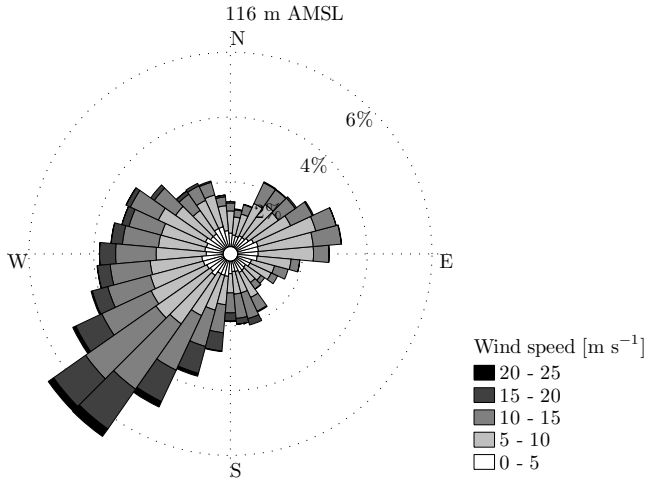

Figure 63: The wind rose at Egmond aan Zee at 116 m AMSL

range 0–0.125. Within the wind directions where the measurements are affected by the wind farm, the wind shear does not become highly negative, as for the Lillgrund met mast, although the hub height of the turbines at the wind farm is 90 m AMSL and the center of the wake is about that height as well.

The range of α values for all sectors, shown in Fig. 65, does not reveal a symmetric distribution, but rather one close to those observed at most wind lidar nodes, with a 'bump' on the range 0.1–0.3. There are not many negative α values. The centroid of the distribution (0.056) is rather low compared to the theoretical neutral (0.077).

The diurnal and monthly evolutions of the α-values measured at 93 m AMSL from July 1, 2005, to June 30, 2008, are illustrated in Fig. 66. From the mean values there is a slight diurnal variation of α; lower values around daytime and higher during nigh time. When analyzing the median instead of the mean, the same diurnal variability is observed although more pronounced (not shown). When analyzing the mean or median values of α in a monthly basis, it is observed slightly lower values during autumn and higher during spring time. The monthly uncertainty is highest in summer and lowest in winter but the amount of data is also higher and lower in

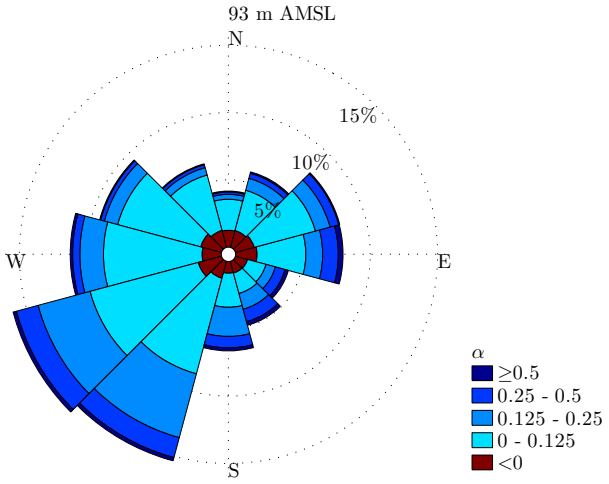

Figure 64: *The vertical wind shear rose at 93 m AMSL at Egmond aan Zee*

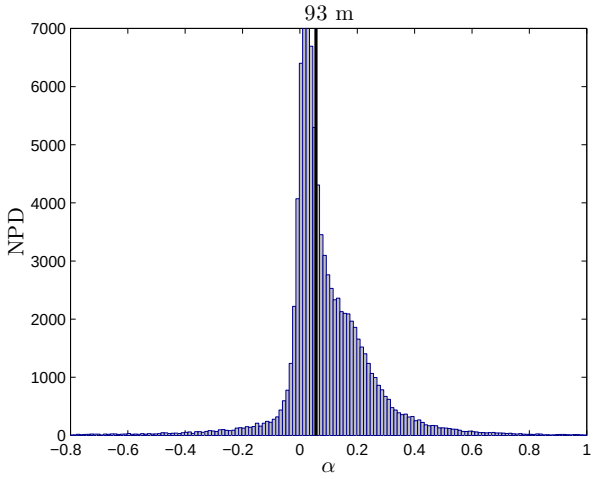

Figure 65: *All-sector distribution of the vertical wind shear at 93 m AMSL at Egmond aan Zee. The solid black line represents the centroid of the distribution* $\alpha = 0.056$

the same periods, respectively.

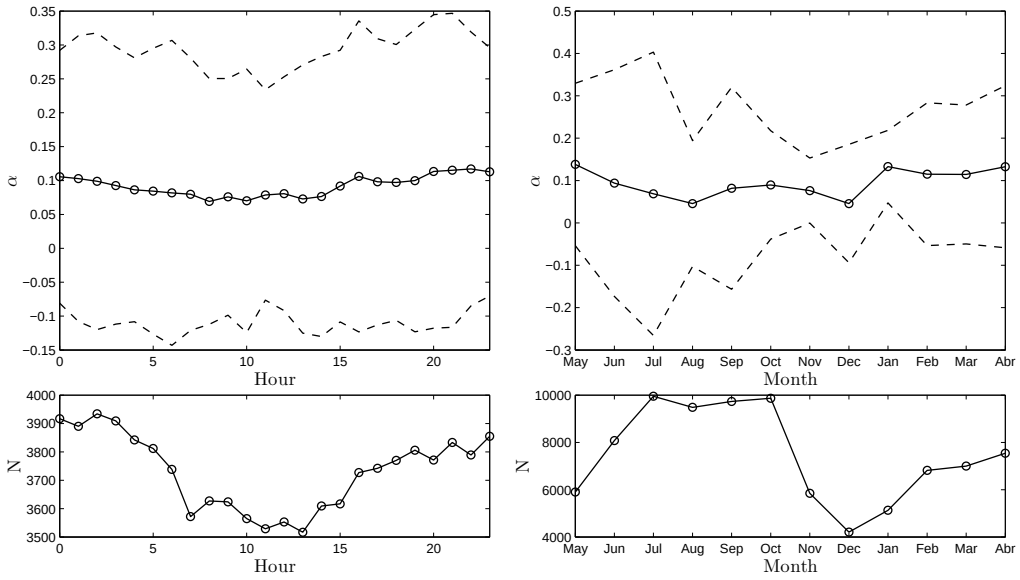

Figure 66: (top) Diurnal (left) and monthly (right) evolution of the all-sector mean vertical wind shear at 93 m AMSL at Egmond aan Zee. The dash lines represent the mean±1 standard deviation. (bottom) Number of 10-min measurements used for the calculations on top

5 Multi-variational correlation analysis

The multi-variational correlation analysis is here aimed to derive and analyze the dependency of the vertical wind shear on:

1. Fetch (distance to shore) per wind direction
2. Wind speed
3. Season
4. Atmospheric stability

In Section 4, we already obtained an overview on the behavior of the vertical wind shear per node and direction. Here we complement the analysis and provide a better outlook of the results.

5.1 Fetch dependency

The vertical wind shear α is analyzed for each NORSEWInD node within each wind sector at the available height closest to 100 m AMSL. For each wind sector and node, the mean fetch or distance to shore has been extracted. An example of the procedure is shown in Fig. 67 for the Jacky wind lidar node.

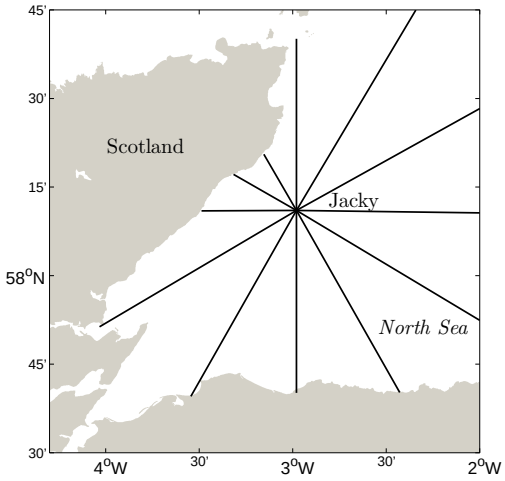

Figure 67: Fetch dependency per wind direction on the Jacky wind lidar node. The solid lines show the distance to shore for each 30° sector

The α values are then derived per sector within the range $[-1, 1]$ in order to avoid 'contamination' due to very low and high observed α values. The results for all NORSEWInD nodes, except for the Høvsøre one, are shown in Fig. 68. For each node, there are 12 points representing the 12 wind sectors.

Assuming that the atmospheric stability is close to neutral in the long term for each of the nodes and wind sectors, we then obtain from MOST in Eq. (13):

$$\alpha = \frac{1}{\ln\left(z/z_o\right)}, \tag{23}$$

which means that α increases with increasing roughness. The roughness over the sea can be modeled using Charnock's relation (Eq. 4), and so,

$$\alpha = \left[\ln\left(\frac{z}{\alpha_c\ u_*^2/g}\right)\right]^{-1}. \tag{24}$$

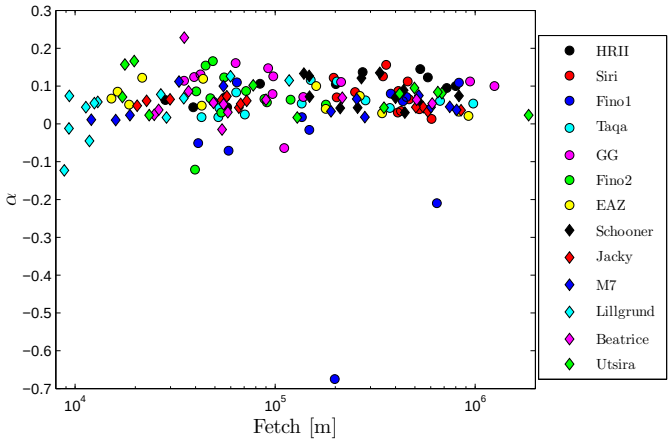

Figure 68: Fetch dependency of the vertical wind shear close to 100 m AMSL for all NORSEWInD nodes and all wind sectors

It is rather complicated to understand the behavior of α with fetch. Higher wind speeds are expected to be observed further offshore, which implies an increase of u_* (and so the roughness), resulting in decreasing α values with fetch. However, when approaching the coast, the values of α_c increase and so the roughness (Sempreviva et al., 1990). Also, depending on how far offshore the vertical wind speed profile is analyzed, one can observe the internal boundary layer (IBL) formed at the land-sea transition. If the observation height is low (high), the vertical wind shear will be driven by the sea (land), and α will be low (high). The 'inflection' point of the vertical wind speed profile, i.e. the height where the wind profile turns from offshore to onshore, depends on many parameters including atmospheric stability. Based on the study of Floors et al. (2011), the IBL generated from the sea-land transition at Høvsøre develops a kink in the wind profile at ∼80 m AGL within the first 1700 m (i.e. a ratio of 1:21.25). Following this result we expect lower vertical wind shears after the first 2125 m offshore (assuming an observation height of 100 m AMSL) and higher and close to onshore values for shorter fetches.

Figure 68 however presents a good number of outliers of the trend, which is a rather constant α value close to 0.1. From the work in Section 4, we found that the Fino 1 node shows very few or no data in sectors 2, 3 and 5, a considerable amount of negative α values in sectors 4, 6 and 11 and positive values in sector 12. The wind farm at Lillgrund is within the directions 345–100°, i.e. sectors 1–4. Fino 2 presents a considerable amount of negative α values in sectors 1. At Beatrice the winds coming from sectors 6–10 are dubious. The wind farm at Horns Rev II affect the wind lidar observations in sectors in sectors 8–1. For the wind farm at Egmond aan Zee the wake-affected sectors are 12–5. The wake of the Horns Rev I wind farm affects sectors 9–11. The wind lidar measurements at Utsira are always affected by the orography of the island. For the Jacky wind lidar node, the amount of data is too low. When all the values of these sectors (and nodes in the case of Utsira and Jacky) are extracted the dependency on fetch of the NORSEWInD nodes is illustrated in Fig. 69.

As illustrated there is no clear indication of a decreasing α value with distance from the coast. Therefore, we restrict the data even further either to those nodes, where we know that the wind lidar has been properly evaluated at Høvsøre prior to deployment and that there is an installation report of it, or to the mast data from which the vertical wind shear has been analyzed based on selecting the redundant wind speed measurement, which best fits the wind conditions. The results are shown in Fig. 70, which does not indicate a general trend for the four nodes evaluated, although the Siri wind lidar and the Egmond aan Zee nodes reveal a decreasing trend for α for increasing fetch.

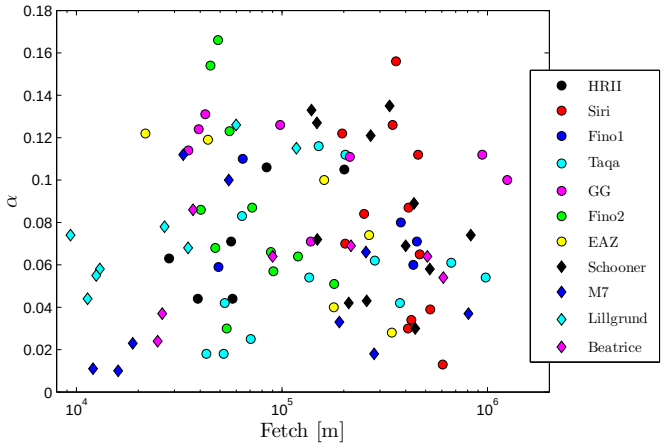

Figure 69: Fetch dependency of the vertical wind shear close to 100 m AMSL for selected NORSEWInD nodes and wind sectors

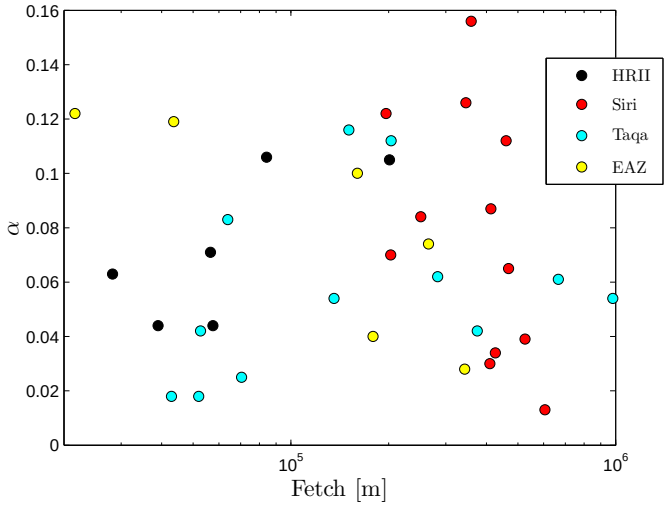

Figure 70: Fetch dependency of the vertical wind shear close to 100 m AMSL for NORSEWInD nodes where there is lower uncertainty on the observations

5.2 Wind speed dependency

The dependency of the vertical wind shear α on wind speed is analyzed for each NORSEWInD node at the available height closest to 100 m AMSL (the wind speed is computed at the height where α is also calculated). The scatter of such a dependency is very high, so a moving averaging method has been used to derive the trend of α with wind speed. An example of the α dependency on wind speed at Egmond aan Zee for each 10-min observation is shown in Fig. 71 together with the moving average. The figure clearly illustrates that α increases with wind speed and that a very high degree of scatter is found, particularly at low wind speeds where α is often observed under the negative range.

Figure 72 illustrates the result of the moving average for all NORSEWInD nodes, except for that at Høvsøre, since those measurements correspond to the land sector where the roughness is not a function of wind speed. The range of wind speeds analyzed is 5–25 m s^{-1}, which corresponds to most observations at most nodes. Most of the nodes show increasing α values with increasing wind speed, although some exceptions (Horns Rev II, M7, Greater Gabbard).

It is also illustrated the theoretical relation between α and the wind speed at 100 m AMSL assuming Charnock's relation, neutral atmospheric conditions and using the logarithmic wind profile, i.e. combining Eqs. (3) and (24). For most nodes, α is well predicted by such relation within the range 5–10 m s^{-1} and is under-predicted for wind speeds higher than 10 m s^{-1}.

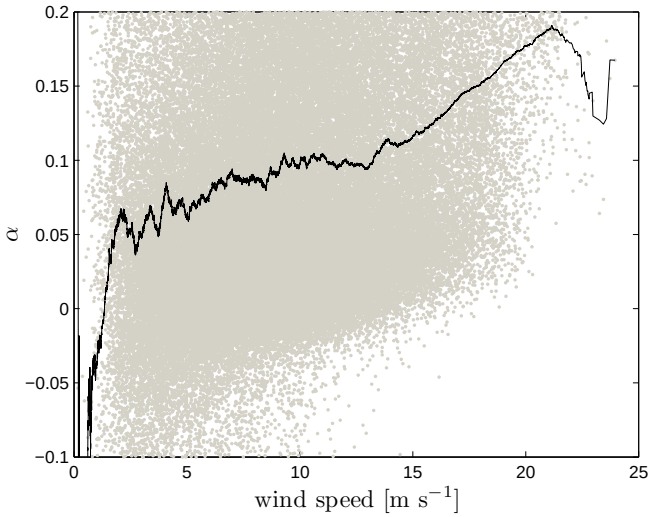

Figure 71: Wind speed dependency of the vertical wind shear at Egmond aan Zee at 93 m AMSL. The grey dots represent each 10-min α estimation and the solid black line the moving average

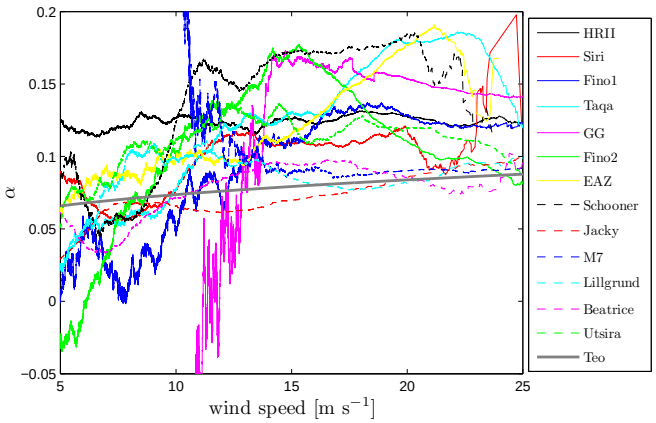

Figure 72: Wind speed dependency of the vertical wind shear close to 100 m AMSL for all offshore NORSEWInD nodes. The theoretical neutral wind speed dependency is shown in the solid grey line

The result of the relation using a lower level, e.g. 70 m AMSL, which is close to the height where α has been computed for some of the masts, does not change the differences at all.

By removing data and nodes based on the same criteria, as those explained in Section 5.1, the result shows nearly the same tendencies and values as illustrated in Fig. 73. For the Horns Rev II wind lidar, removing the wake-distorted data do not affect the nearly constant α behavior with wind speed. The filtered Fino 1 and Egmond aan Zee data appear to be smoother in the lowest range of wind speeds. No improvement is found neither at M7 nor at Greater Gabbard.

5.3 Seasonality dependency

The dependency of the vertical wind shear α on seasonality is also analyzed for each NORSEWInD node at the available height closest to 100 m AMSL. The α values have been classified in four different seasons: Winter for the months of December, January and February (hereon as DJF); Spring for March, April and May (MAM); Summer for June, July and August (JJA) and Autumn for September, October and November (SON). The data for the Beatrice wind

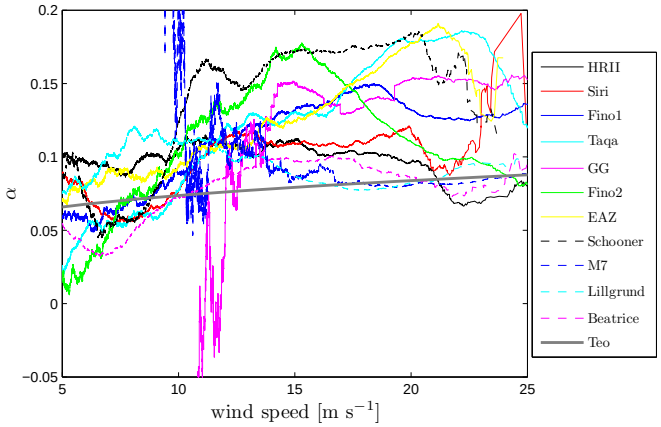

Figure 73: *Wind speed dependency of the vertical wind shear close to 100 m AMSL for selected NORSEWInD nodes and wind sectors. The theoretical neutral wind speed dependency is shown in the solid grey line*

lidar only cover one season and therefore is left out from the analysis. Data are also not available for the DJF period at the Schooner wind lidar and for the DJF and MAM periods at the Jacky wind lidar node. We already filter the data based on the same criteria from the previous two sections. As in Section 5.1, the α values are derived per season within the range $[-1, 1]$ in order to avoid 'contamination' due to very low and high observed α values.

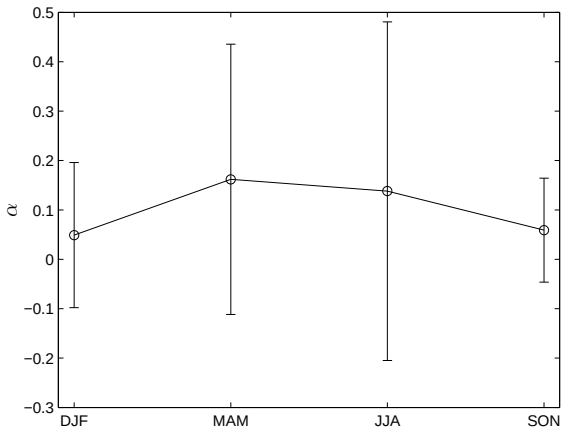

Figure 74: *Seasonality dependency of the vertical wind shear at 96 m AMSL for the Horns Rev II wind lidar. The error bars denote* ± 1 *standard deviation*

We first show a typical example of the α behavior with seasonality for the Horns Rev II wind lidar node in Fig. 74. It is illustrated that for this offshore site, α is highest in Spring and lowest between Autumn and Winter. This was already observed in Section 4, where the lowest α values are encountered between September and December for most of the offshore nodes. As already mentioned, such a behavior is a combination between the wind systems in the North Sea and the fact that the locations are over water: In Spring the North Sea is still very cold due to the past Winter period (it will take longer for the sea to warm up than the surrounding land), but the air has warmed up faster and so stable conditions are very often observed leading to relatively high wind shears. Around late Autumn, the conditions turn often to be unstable, since the air has cooled down much faster than the sea (which is still rather warm from the summer) and therefore the wind shears will be generally the lowest. Interesting, during winter time in the North Sea there are often storms and so the variability of the wind is the highest and so of the vertical wind shear, as we can observe from the error bars in the figure.

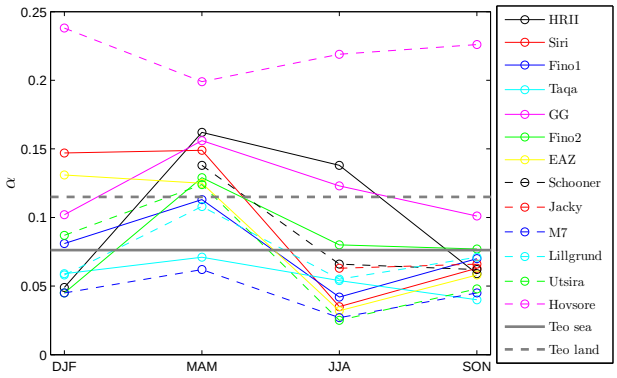

Figure 75: Seasonality dependency of the vertical wind shear close to 100 m AMSL for selected NORSEWInD nodes, directions and seasons. The theoretical neutral α values for a typical offshore site ($z_o = 0.0002$ m) and for a onshore site ($z_o = 0.015$ m) are shown in the grey lines

Figure 75 illustrates the results of the α dependency on seasonality for most of the NORSEWInD nodes. All these offshore NORSEWInD nodes show the highest α values in Spring and the lowest in Autumn (and sometimes even in Summer or Winter depending on the node). Interestingly, the behavior is reversed at the Høvsøre node, since this is an onshore site, where only winds coming from land are taken into account for the analysis. Also, it is clear that at Høvsøre the vertical wind shear is much higher than at all offshore nodes, since the roughness length at Høvsøre is about two orders of magnitude higher than the sea one. We also add two lines in the graph that correspond to the α values estimated at 100 m AMSL offshore and at 90 m AGL onshore assuming neutral conditions (Eq. 23). As shown, for both onshore and offshore cases, the lines are generally below the observations, particularly, at the onshore Høvsøre node. This behavior might be related to a general slightly stable atmosphere over the North Sea and stable conditions for northeasterly winds at Høvsøre, which lead to higher values of α than predicted assuming neutral conditions.

5.4 Atmospheric stability dependency

The dependency of the vertical wind shear α on atmospheric stability can only be analyzed at the NORSEWInD stations where there is either sonic anemometer or temperature measurements at two different levels. Thus, this restricts the analysis to the met mast nodes: Høvsøre, M7, Fino 1, Fino 2 and Egmond aan Zee.

Two different categories have been studied from the observations: Unstable and stable atmospheric conditions. The measure of such conditions is obtained by deriving the potential temperature difference between two levels close to the surface (highest minus lowest level). In case of availability of a sea temperature close to the surface, this is used for the analysis. Unstable and stable conditions are then found for negative and positive potential temperature differences, respectively. At Høvsøre, positive and negative heat fluxes indicate unstable and stable conditions, respectively.

We already filter the data based on the same criteria from the previous three sections. The α values are derived per stability class within the range $[-1, 1]$ in order to avoid 'contamination' due to very low and high observed α values.

We first show a typical example of the α behavior with atmospheric stability for the Egmond aan Zee met mast in Fig. 76. It is illustrated that for this offshore site, α is higher during stable than unstable conditions. Stable conditions are often observed in Spring and unstable in Autumn and so the connection to the seasonality behavior in the previous section. It is also clear that the variability of wind shear in stable conditions is much higher than in unstable, due to the storms found in winter time, as well as low boundary layers and presence of low-level jets during stable conditions.

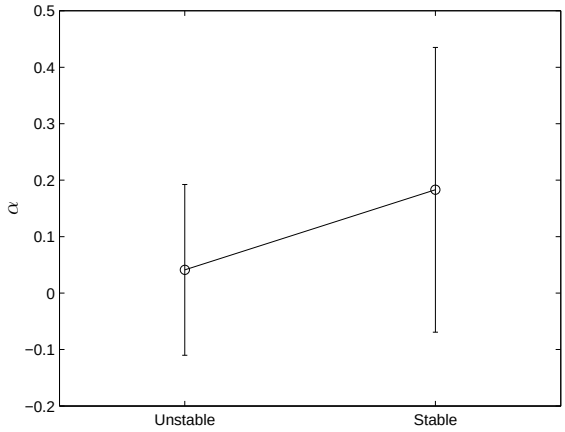

Figure 76: Atmospheric stability dependency of the vertical wind shear at 93 m AMSL for the Egmond aan Zee met mast. The error bars denote ± 1 standard deviation

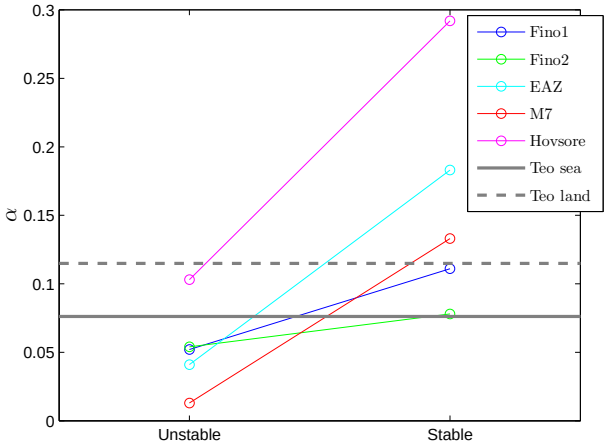

Figure 77: Seasonality dependency of the vertical wind shear close to 100 m AMSL for selected NORSEWInD nodes and directions. The theoretical neutral α values for a typical offshore site ($z_o = 0.0002$ m) and for an onshore site ($z_o = 0.015$ m) are shown in the grey lines

Figure 77 illustrates the results of the α dependency on atmospheric stability for most of the NORSEWInD met mast nodes. All these NORSEWInD nodes (offshore and onshore) show a higher α value for stable than for unstable conditions. For both stabilities, the vertical wind shear at Høvsøre is much higher than that at all offshore nodes. As shown, for the offshore and onshore cases, the theoretical lines are in between the results for the two stability categories. For the unstable conditions, the results for all nodes are within a smaller range of α values than the results for stable conditions, which is related to the high variability of the wind under states where the atmosphere is warmer than the ground/sea.

6 NWP data for wind shear modeling

In this section, we evaluate the ability of a numerical weather prediction (NWP) model to predict atmospheric-like parameters, which can be used for the modeling of the vertical wind shear. Most of the evaluation is documented in the paper entitled **Atmospheric stability and turbulent fluxes at Horns Rev – and intercomparison of sonic, bulk and WRF model data** by Peña and Hahmann (2012), published in the Wind Energy journal. Here we provide an small version of it.

The idea of the paper is to compare different atmospheric parameters, which can be either observed from sonic or bulk measurements or modeled with a NWP model at an offshore site in the North Sea. For vertical wind shear modeling/analysis, we would like to be able to accurately model the turbulent fluxes, temperatures and wind speed. However, as it is shown in the paper, a NWP model lacks of proper modeling of such parameters when the analysis is performed on a 'short-term' basis, i.e. when looking at 10-min, 30-min, 1-hour or few days averages. Interestingly, the NWP model seems to be able to provide nearly the same distributions (with the same properties) of the inverse of the Obukhov length when compared to long-term observations. This is important as a recent theory has been suggested (see Section 2.2), where the long-term observations of the inverse of the Obukhov length are used to estimate the correction of the long-term vertical wind speed profile. Therefore, assuming that the NWP model also provides a good estimate of the long-term distribution of atmospheric stability at other offshore locations (in Section 7 we perform the analysis for the other NORSEWInD nodes), one can use it to derive the long-term corrections of the vertical wind speed profile, e.g. at all NORSEWInD wind lidar nodes, where there are no measurements of atmospheric stability.

Abstract

Direct estimations of turbulent fluxes and atmospheric stability were performed from a sonic anemometer at 50-m height on a meteorological mast at the Horns Rev wind farm in the North Sea. The stability and flux estimations from the sonic measurements are compared against bulk results from a cup anemometer at 15-m height and potential temperature differences between the water and the air above. Surface flux estimations from the WRF model are also validated against the sonic and bulk data. The correlation between the sonic and bulk estimates of friction velocity is high and the highest among all velocity comparisons. From the sonic-bulk-WRF intercomparison, it is found that the atmospheric stability measures at the sonic height tend to be closer to the neutral value than the WRF and bulk estimates, which are performed within an air layer closer to the surface, not only from a systematic bulk and WRF under-prediction of the friction velocity when compared to the sonic value, but also because of the lower magnitude of the sonic heat flux compared to that from the WRF simulations. Although they are not measured, but parameterized or estimated, the bulk-WRF comparisons of friction velocity and 10-m wind speed show good agreement. It is also shown that on a long-term basis, the WRF and bulk estimates of stability are nearly equal and that a correction towards a slightly stable atmospheric condition has to be applied to the long-term wind profile at Horns Rev and at other locations over the North Sea, the correction being larger for points close to the coast.

6.1 Introduction

Since 1999, the meteorological conditions in the Danish North Sea have been continuously measured in association with the planning and harvesting of Denmark's offshore wind power. As part of this initiative, the meteorological mast M2 was installed to better understand the flow regime in which the wind turbines of the Horns Rev wind farm were to operate. In 2001, the installation of the wind farm began southeast of M2 and since westerly winds are

predominant in this area of the North Sea, the measurements at M2 are not often influenced by the wind farm's wake. Therefore, a number of meteorological studies have been carried out using M2-data. These range from validation of remote sensing instrumentation (Hasager et al., 2008; Peña et al., 2009), analysis and modeling of wind profiles (Peña and Gryning, 2008; Peña et al., 2008), atmospheric stability (Sathe et al., 2011) and wind variability (Vincent et al., 2011).

Direct sonic-bulk flux comparisons have not been performed at Horns Rev. In Peña et al. (2008); Sathe et al. (2011); Vincent et al. (2011), the atmospheric stability was estimated from bulk relations, which include the bulk Richardson number ($\mathrm{Ri_b}$). Only in Peña et al. (2008), atmospheric stability relations from measurements using a sonic anemometer, which directly estimates the turbulent fluxes, were compared to bulk relations estimated from conventional temperature difference and wind speed observations. Our analysis therefore centers on direct estimations of atmospheric stability measures such as the Obukhov length L, since the effects of the air layer stratification on, e.g. the wind profile and the turbulence spectra, can be accounted for from the evaluation of such parameter.

The knowledge of atmospheric stability is not only important to characterize the meteorological conditions, but is also addressed using the observations at this particular site, because the efficiency in extracting energy from the wind of a number of offshore wind farms has been observed to have a strong dependency on stability. For example, Jensen (2007) found more than 6% difference in annual mean array efficiency for the Horns Rev wind farm when comparing data under unstable and stable conditions. Further, Barthelmie and Jensen (2010) analyzed data from the Nysted wind farm in the Danish Baltic Sea and observed that the losses in array efficiency under stable compared to neutral conditions increased with wind speed up to 8.1%, whereas the efficiency slightly improved under unstable compared to neutral conditions.

Because it is difficult and expensive to perform accurate estimates of atmospheric stability, particularly in offshore conditions, it is of high interest to validate the estimations of the turbulent fluxes, and thus stability, from NWP models such as the Advanced Research WRF (ARW-WRF; Weather, Research and Forecasting model) (Wang et al., 2009) against the sonic observations and the bulk estimations. This is important since these models, which can produce data for a long period in a relatively inexpensive fashion, are extensively being used not only for weather prediction, but also for wind-energy related activities such as wind resource assessment (Byrkjedal and Berge, 2008), wind profile studies (Hahmann and Peña, 2010) and short-term wind power forecasting (Cutler et al., 2008).

Another possible outcome from the output of NWP models is the estimation of the long-term atmospheric stability. It is becoming common practice to use NWP models to generate long-term wind speed time series at locations with few or no observations, but it is rather novel to determine the long-term stability correction of the long-term wind profile for wind resource predictions (Kelly and Gryning, 2010). Therefore, it is important to validate the ability of the NWP models to estimate such long-term corrections, since at most of the potential wind energy sites and in many current wind resource campaigns, there is a lack of atmospheric stability observations.

Here, we try for the first time to evaluate the ability of the WRF model outputs to determine the long-term stability correction. In principle, we would like to use sonic measurements to derive such correction because a sonic anemometer directly estimates the turbulent fluxes. However, sonic data do not span for a long period at M2 and the instrument was installed at 50 m so the sonic fluxes might not be representative for the surface layer in which bulk and WRF estimates are available.

We here first introduce a number of means to derive turbulent fluxes and stability measures from sonic, bulk and WRF-model data from observations at the Horns Rev site. We then compare the paired sonic-bulk, sonic-WRF and bulk-WRF estimations. The long-term stability corrections at the site and within a wide area in the North Sea are then presented as well as a discussion and concluding remarks.

6.2 Theory

A direct way to account for the static atmospheric stability is by estimating the Obukhov length, a length scale related to the ratio of the momentum to the heat turbulent flux, since the functions that correct the vertical wind shear and temperature gradient in the surface layer, i.e. the ϕ_m and ϕ_h functions from MOST (Monin and Obukhov, 1954), are universal dimensionless functions of the dimensionless stability parameter z/L. Here we present three different methods for estimating L.

Sonic fluxes

From high-frequency three-dimensional sonic anemometer measurements, time series of the longitudinal, transversal and vertical wind speed components, u, v and w, respectively, (and for some instruments a temperature time series) can be used to directly estimate the kinematic turbulent fluxes. We are particularly interested in the kinematic momentum fluxes $\overline{u'w'}$ and $\overline{v'w'}$ and the kinematic virtual heat flux $\overline{w'\theta'_v}$.

L can be directly estimated from the turbulent fluxes as from Eq. (6). A sonic anemometer (indicated with the subscript $_{\mathsf{s}}$) measures the friction velocity directly, so $u_* = u_{*\mathsf{s}}$, but it does not directly measure $\overline{w'\theta'_v}$, but a slightly higher quantity,[2] $\overline{w'\theta'_v} + 0.1\overline{T}\ \overline{w'q'}$ (Kaimal and Gaynor, 1991), where q is the water vapor specific humidity. The sonic temperature is also not equal to T, but this has a negligible effect on the estimates of L from Eq. (6).

Bulk fluxes

In the absence of high-frequency measurements, bulk formulae can be used to derive the turbulent fluxes. From the combination of bulk estimates of the momentum, heat and humidity fluxes, an estimation of z/L based on $\mathsf{Ri_b}$ is given for unstable and stable conditions, respectively,

$$\frac{z}{L} = C_1\ \mathsf{Ri_b} \quad \text{and} \tag{25}$$

$$\frac{z}{L} = \frac{C_1\ \mathsf{Ri_b}}{1 - C_2\ \mathsf{Ri_b}}. \tag{26}$$

Grachev and Fairall (1996) validated Eq. (25) with $C_1 = 10$ for the range $-1 \leq \mathsf{Ri_b} \leq 0$ and Eq. (26) with $C_1 = 10$ and $C_2 = 5$ implying a critical $\mathsf{Ri_b} = 0.2$ with

$$\mathsf{Ri_b} = -\frac{g\ z\ \Delta\theta_v}{\overline{T}\ \overline{U}^2}, \tag{27}$$

where Δ refers to the difference between the values at the surface and the height z, and U is the magnitude of the horizontal wind vector.

For the estimation of u_* from observations of U at a given level z, a bulk coefficient for momentum or drag coefficient C_D can be used (Smith, 1980). However, C_D varies depending on z/L and U. Instead, we estimate u_* using the diabatic wind profile (Eq. 5). z_o can be parameterized using the model of Charnock (1955) (Eq. 4). u_* can then be computed from Eq. (5) using the wind speed observation at one height, estimating ψ_m from z/L in Eqs. (25) and (26) and assuming z_o as in Eq. (4). This procedure has already been applied in Peña et al. (2008) and Badger et al. (2010) for comparison with sonic and synthetic aperture radar data, respectively.

WRF fluxes

The WRF model numerically solves prognostic equations for quantities such as the wind speed, air temperature, and specific humidity. The averaged subgrid-scale fluxes are parameterized

[2] without taking into account the crosswind correction, which depends on the configuration of the instrument

and they represent a combination of the effects of the land surface (if the grid point is over land), surface layer and planetary boundary layer (PBL) parameterizations.

Over the ocean, the surface heat flux is calculated using a bulk formula dependent on the difference in temperature between the surface and the first model level. The calculation is coupled to the PBL scheme via surface exchange coefficients that depend on z_o (determined from Charnock's relation) and MOST relations. Surface diagnostic fields (e.g. the 2-m temperature and 10-m wind components) are computed in the surface layer scheme.

6.3 Site, measurements and model setup

The Horns Rev wind farm is located in the North Sea 12–17 km from the Danish west coast (Fig. 78-left). A meteorological mast M2 was erected before the construction of the wind farm and measured the wind conditions until May 2007 when it was removed. For this study, we use M2-measurements of wind speed from two Risø cup anemometers at 15 m AMSL, wind direction from a wind vane at 28 m AMSL, temperature from sensors at 13 m AMSL and 4 m below mean sea level (BMSL), relative humidity at 13 m AMSL and pressure at 55 m AMSL. These measurements are stored as 10-min values and represent the bulk data. When estimating parameters related to $\Delta\theta$ such as $\mathrm{Ri_b}$, the surface sea temperature (SST) is assumed to be equal to that measured at 4 m BMSL. This, as found by Peña et al. (2008) when comparing the 4 m BMSL temperatures to a satellite SST product, is a valid assumption at Horns Rev.

A Metek USA-1 sonic anemometer was installed at 50 m AMSL on M2, shortly after the erection of the mast, and measured time series of u, v, w and T until 2005. These were recorded at 12 Hz and the fluxes are estimated over 10-min periods from the linearly detrended signals.

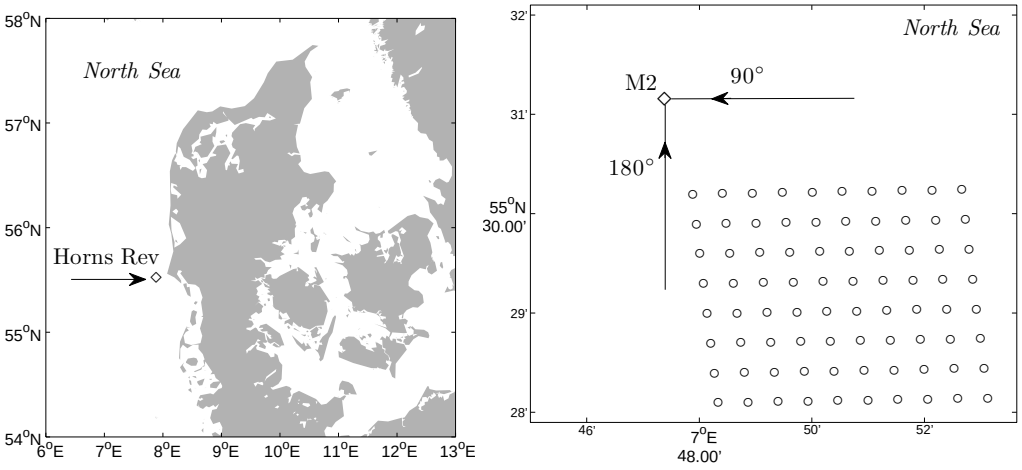

Figure 78: Horns Rev wind farm in the Danish North Sea (left) and layout of the wind farm (right) indicating the location of M2 (diamond) and the turbines (circles).

Data filtering and treatment

The sonic and cup anemometer data are selected for wind directions $\geq 180°$ and $\leq 90°$ to avoid the effect of the wake of the wind farm (Fig. 78-right). From the analysis of the wind speed ratio from the two cup anemometers at 15 m (mounted on the southwest and northeast booms) as function of the wind vane direction, Peña et al. (2009) found that the mast was installed with an offset of 34° from the north as shown in Fig. 79. The 15-m wind speed is then selected from one or the other cup according to the wind direction to avoid the direct mast shade. The sonic anemometer, on the contrary to the wind vane, was mounted

in relation to the mast north, i.e. the sonic wind direction shows the 34° offset compared to the wind vane values.

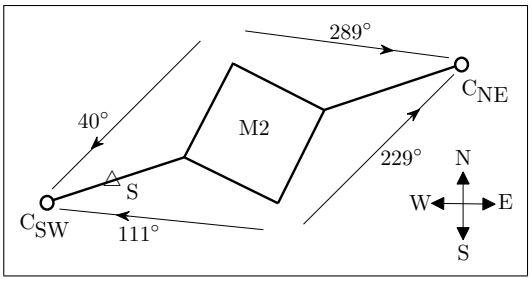

Figure 79: Top view of M2 at Horns Rev. C_{NE} and C_{SW} are respectively the northeast and southwest cup anemometers at 15 m and S the sonic anemometer at 50 m height.

The sonic anemometer was mounted on the southwest boom with a shorter distance to the mast compared to that of the cup anemometer and the influence of the mast on the sonic measurements is extremely high. In flat and homogenous terrain, the surface-layer momentum flux $\overline{u'w'}$ must be negative, but sometimes becomes positive in the MBL under, e.g. conditions where the waves are not generated by the surface winds such as swells (Carlsson et al., 2009). From the sonic data, there are many cases where $\overline{u'w'} > 0$, particularly for a well-defined range of sonic wind directions (Fig. 80-left). Therefore, when using the sonic data, the sonic wind directions 100–270° are the only ones used.

The correspondence between sonic and wind vane directions is also used as a filter, whenever sonic data are analyzed. The wind vane is a more robust instrument than the sonic anemometer, it is less influenced by turbulence and is located further out on the boom. Thus, wind directions that differ by more than $34 \pm 20°$ from the wind vane direction are also filtered. As a summary, Fig. 80-right illustrates the direction ranges of sonic data used in this study.

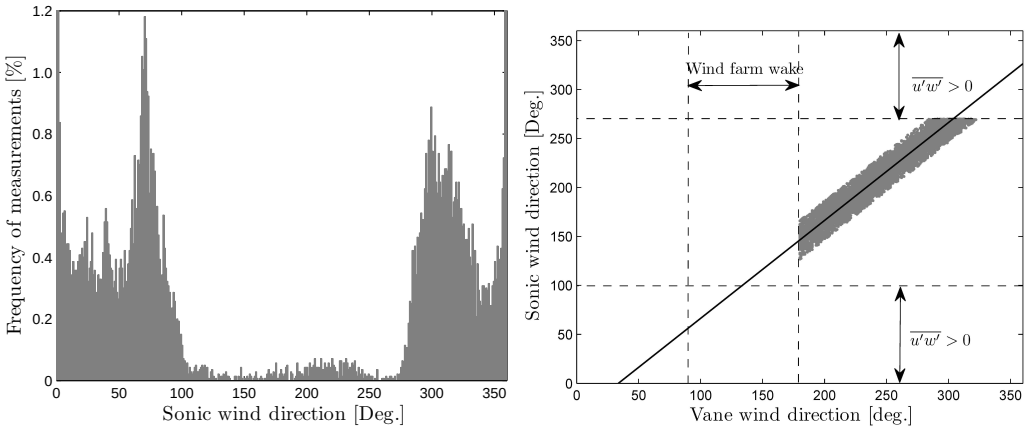

Figure 80: Availability of sonic anemometer observations for the range of sonic wind directions where $\overline{u'w'} > 0$ (left) and wind direction ranges of sonic anemometer observations used in the study (right).

No filters are applied based on the wind speed values, since we require as many measurements as possible, but whenever sonic estimates are compared, only data with $u_* \geq 0.02$ m s^{-1} are used, because L becomes too small for comparison purposes and MOST is not longer valid. The sonic kinematic heat flux $\overline{w'T'}_s$ is corrected for crosswind contamination using the findings in Liu et al. (2001).

WRF model setup

The dynamical downscaling carried out with the WRF model uses the technique developed by Hahmann et al. (2010), but using Newtonian relaxation terms toward the large-scale analysis (also known as grid or analysis nudging). Grid nudging is done for the outer domains only. Initial and boundary conditions and the gridded fields used in the nudging are taken from the NCEP/NCAR reanalysis II Kanamitsu et al. (2002) at 2.5° resolution. The SSTs are obtained at 0.25° horizontal resolution and temporal resolution of 1 day. The simulation covers the period from January 1, 1999 to December 31, 2009 with hourly outputs.

The model domain configuration is shown in Fig. 81. It has 41 vertical levels with the model top at 50 hPa. The lowest 4 vertical levels are located at approximately 21, 74, 123 and 163 m AMSL. The outer domain has a horizontal grid spacing of 45 km and the nested inner domain 15 km. In this study we use outputs from the grid point closest to the M2 mast in the 15 km domain. The model setup uses the Yonsei University (YSU) PBL scheme (Hong et al., 2006), which is classified as a first-order closure scheme. This scheme is selected because it is the most commonly used in the WRF community (Storm et al., 2009; Hu et al., 2010). In the convective boundary layer, it uses a non-local boundary layer vertical diffusion scheme with diffusivity as a function of the local wind shear and local Richardson number. The scheme also includes a non-local gradient adjustment term for heat and momentum tendencies. For the stable boundary layer, the diffusion coefficient is based on the bulk Richardson number between the surface layer and the top of the boundary layer.

We also use the following physical parametrization options: Thompson graupel scheme (Thompson et al., 2004), Kain-Fritsch cumulus parametrization (Kain and Fritsch, 1990), rapid radiative transfer model scheme for longwave radiation (Mlawer et al., 1997), Dudhia scheme for shortwave (Dudhia, 1989) and MM5 similarity theory surface layer scheme (Skamarock et al., 2008). Land surface processes are the Noah land surface scheme (Chen and Dudhia, 2001), where land use categories are derived from the USGS 24-category data.

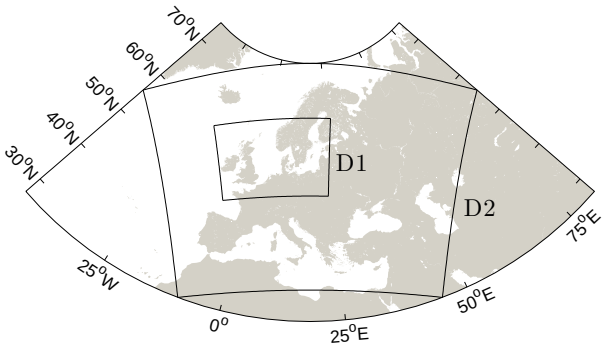

Figure 81: Domain configuration of the WRF runs. The outer and inner domain are indicated as D2 and D1, respectively.

6.4 Results of the sonic, bulk and WRF intercomparison

For each of the comparisons (sonic vs bulk, sonic vs WRF and bulk vs WRF), we present the results related to the velocity scales, temperature scales, and finally for stability in 2D histograms, where the shading indicates the amount of data.

Comparison of sonic and bulk estimations

Due to the height difference between the sonic and cup anemometers (50 and 15 m, respectively), it is difficult to directly compare the sonic with the cup wind speed. However, the velocity scales are compared by plotting the sonic friction velocity $u_{*\mathsf{s}}$ as function of the cup

wind speed at 15 m $\overline{U_{15}}$ (Fig. 82-left). u_* increases more than linearly with increasing wind speeds as predicted for neutral conditions when Charnock's relation, Eq. (4) with $\alpha_c = 0.0144$, is used in combination with the logarithmic wind profile, i.e. Eq. (5) with $\psi_m = 0$ (dashed line in Fig. 82-left). However, a statistical best-fit to the data (solid line in Fig. 82-left) shows that $\overline{U_{15}}$ is slightly overpredicted when z_o is parameterized using Charnock's relation, particularly at very high wind speeds (e.g. for $\overline{U_{15}} = 10.00$ m s^{-1}, 'Charnock's' prediction gives 11.06 m s^{-1})

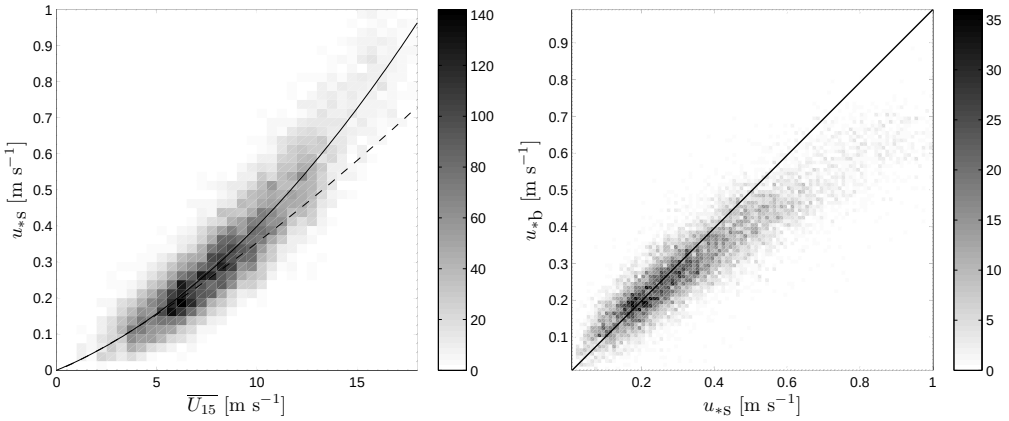

Figure 82: Comparison of the velocity scales measured by the sonic and cup anemometers. (Left) Sonic friction velocity, u_{*s}, as a function of the 15-m cup wind speed, $\overline{U_{15}}$. The dashed line is the prediction for neutral conditions combining Charnock's relation, Eq. (4) with $\alpha_c = 0.0144$, and the diabatic wind profile, Eq. (5), and the solid line the best fit to the data. (Right) Bulk friction velocity u_{*b} against u_{*s}. The colorbar indicates the amount of data in each 2D bin.

A 'bulk' friction velocity $u_{*\mathrm{b}}$ based on the cup wind speed $\overline{U_{15}}$ can be estimated combining the diabatic wind profile and Charnock's relation, Eqs. (5) and (4) with $\alpha_c = 0.0144$, where ψ_m is computed from estimations of z/L from $\mathrm{Ri_b}$. This is shown and compared to $u_{*\mathrm{s}}$ in Fig. 82-right, where $u_{*\mathrm{b}}$ is only underpredicted for high u_* values. The underprediction is explained in Fig. 82-left: for the same $\overline{U_{15}}$-value, $u_{*\mathrm{s}} \geq u_{*\mathrm{b}}$. The statistics are: a linear correlation coefficient (R) of 0.90 and a slope (m) of 0.80 (using a linear regression through zero) for 13439 (N) 10-min observations (after the filtering procedure explained before, only 27 10-min observations show $\mathrm{Ri_b} \geq 0.2$ and are not used for the comparisons).

When deriving bulk stability estimates at Horns Rev, most of the uncertainty comes from the temperature difference measurements, which translates to uncertainty in the estimates of the heat flux. This was found by Sathe et al. (2011), where the uncertainty contribution on the estimation of $\mathrm{Ri_b}$ of both air and sea temperatures (with individual uncertainties of $0.354°$C) was 4 orders of magnitude larger than that of the wind speed (with an individual uncertainty of 0.076 m s^{-1}) for near-neutral conditions. For the derivation of $\mathrm{Ri_b}$ in Eq. (27), the kinematic heat flux $\overline{w'T'}$ is parameterized as,

$$\overline{w'T'} = C_h \; \Delta\theta \; U, \tag{28}$$

where C_h is the bulk heat transfer coefficient. A linear relation between $\overline{w'T'}$ and $\Delta\theta \; U$ cannot be expected because C_h varies as function of $\Delta\theta$, U and z (Smith, 1980). Further, due to the uncertainty in the temperature difference measurements, a much larger scatter will be observed than that for the momentum flux estimations (in Fig. 82-right for u_*). This is illustrated in Fig. 83 when the sonic kinematic heat flux $\overline{w'T'}_{\mathrm{s}}$ is plotted against the bulk flux $\Delta\theta \; \overline{U_{15}}$. For the unstable observations ($\overline{w'T'}_{\mathrm{s}} > 0$), C_h tends to be rather linear, whereas for the stable observations ($\overline{w'T'}_{\mathrm{s}} < 0$), C_h reduces close to neutral conditions. Both of these behaviors were also observed by Smith (1980), from observations in the Dutch North Sea by Oost et al. (2000) and observations at two sites in the Baltic Sea by Rutgersson et al. (2001).

This indicates that a constant C_h cannot directly be used in Eq. (28) without additional stability corrections.

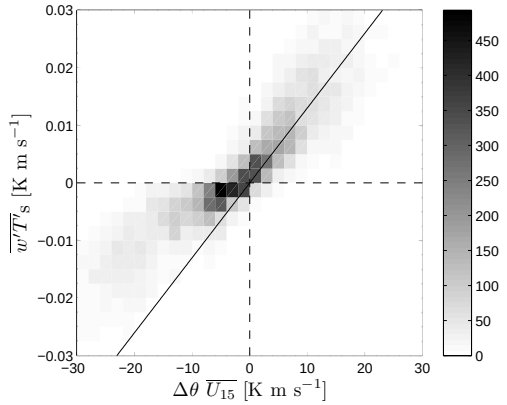

Figure 83: Sonic kinematic heat flux $\overline{w'T'}_s$ as function of the bulk flux $\Delta\theta\ \overline{U_{15}}$. The solid line represents their relation for a bulk heat transfer coefficient $C_h = 1.30 \times 10^{-3}$. The colorbar indicates the amount of data in each 2D bin.

Fig. 84 shows the comparison of the sonic Obukhov length L_s against Ri_b from the bulk measurements, so Eq. (25) can be validated for the unstable observations and Eq. (26) for the stable data. The error between the estimate from Eq. (25) and the unstable data is lower than that between the estimate using Eq. (26) and the stable observations, which is expected, since the bulk estimates are performed well inside the MBL, whereas the sonic observations might be out of the surface MBL in stable conditions. For both, a better correspondence is found when $C_1 = 6.78$ instead of $C_1 = 10$, which agrees with the findings of Friehe (1977) for the range -20 K m s$^{-1} < \Delta\theta\ \overline{U} < 20$ K m s^{-1}, where most of the observations lie (see Fig. 83). Furthermore, for both unstable and stable conditions, the scatter is larger close to near-neutral conditions (the lowest values to the left and bottom in Figs. 84-left and right) in agreement to the uncertainty analysis of L of Vincent et al. (2011) and Sathe et al. (2011).

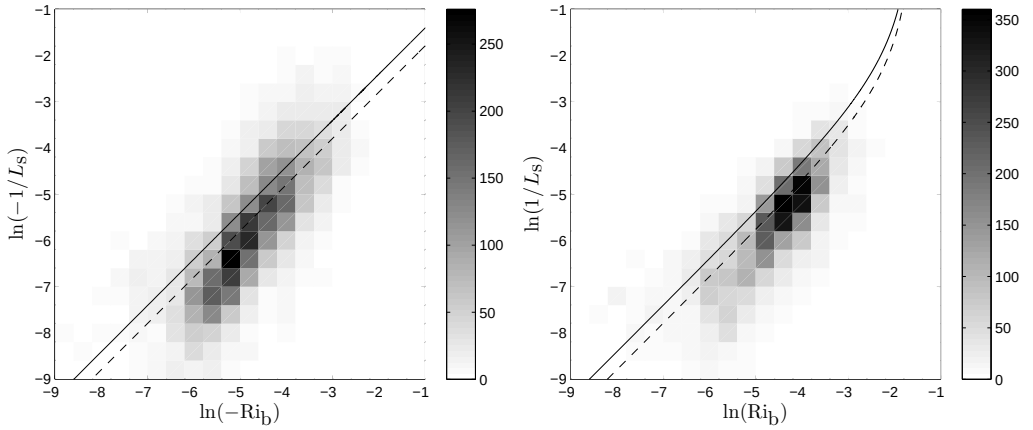

Figure 84: Comparison of the estimates of the bulk Richardson number Ri_b and the sonic Obukhov length L_s for unstable (left) and stable (right) conditions. The solid lines represent Eqs. (25) and (26) for $C_1 = 10$ and $C_2 = 5$ and the dashed lines use $C_1 = 6.78$ instead. The colorbar indicates the amount of data in each 2D bin.

The comparison of L-estimates between the sonic and bulk observations is shown in Fig. 85. There are almost no previous references on L-validations, apart from the qualitative findings in Sušelj and Sood (2010), so taking into account the nature of the comparison, the statistics are rather good for $1/L$: R $= 0.80$ and m $= 1.17$ for N $= 11606$ (a lower N than that for the

velocity scales, because $1/L$ needs to be limited to the range -0.02 m$^{-1} \leq 1/L \leq 0.02$ m^{-1}, otherwise it takes extremely large values for very unstable and very stable conditions). The bulk estimate $1/L_b$ is generally higher than the sonic estimate $1/L_s$, because the values of u_* close to the surface are nearly the same as those at 50 m, whereas the gradient of $\overline{w'T'}$ in the surface layer is much larger (Gryning et al., 2007b), so $1/L$ from Eq. (6) generally increases with height in the surface layer.

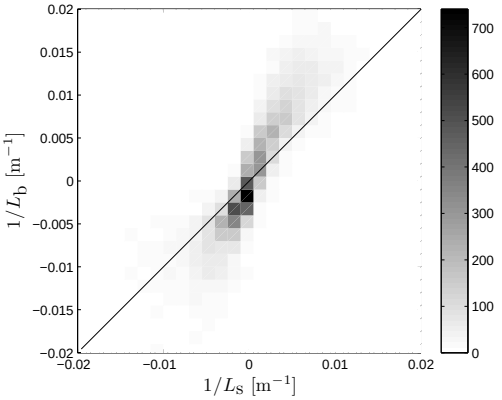

Figure 85: Comparison of the estimates of the sonic and bulk Obukhov lengths, L_s and L_b. The colorbar indicates the amount of data in each 2D bin.

Comparison of sonic and WRF estimations

Figure 86-left illustrates the comparison between the sonic and the WRF-parameterized heat fluxes, $\overline{w'T'}_s$ and $\overline{w'T'}_{WRF}$. Although the scatter is large for both unstable and stable conditions, due mostly to uncertainty on the WRF model output, there is agreement (same trend and nearly always the same sign) between the heat fluxes (R $= 0.70$ and m $= 1.12$ for N $= 3708$). In relation to the findings from the comparison between the sonic and bulk data above, $\overline{w'T'}_s$ (estimated at 50 m) is also lower than the surface-layer value that is estimated by the WRF parametrization, as we expected because the magnitude of the heat flux rapidly decreases with height in the lowest part of the boundary layer (Gryning et al., 2007b).

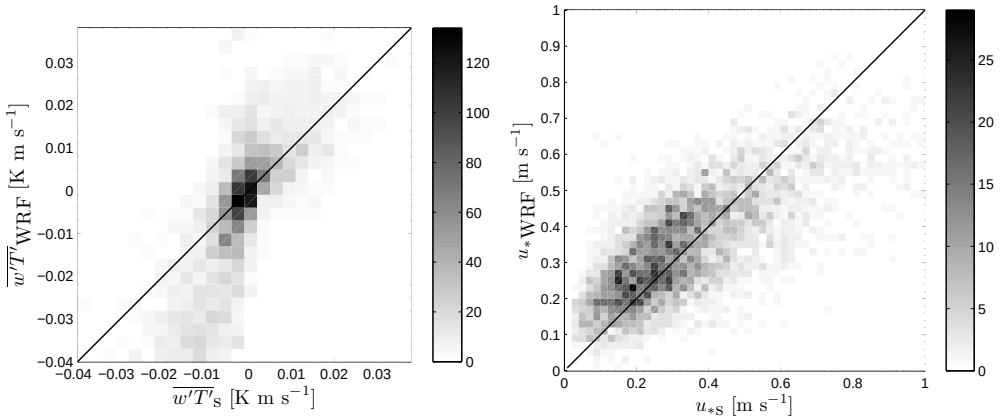

Figure 86: Comparison of the turbulent fluxes from the sonic and the WRF runs. (Left) WRF heat flux $\overline{w'T'}_{WRF}$ against the sonic value $\overline{w'T'}_s$. (Right) WRF friction velocity u_{*WRF} against the sonic value u_{*s}. The colorbar indicates the amount of data in each 2D bin.

The comparison for the friction velocity (Fig. 86-right) between the WRF runs u_{*WRF} and the sonic values u_{*s} is not as good as that between sonic and bulk estimates in terms of

correlation (R $= 0.70$ vs 0.90). In analogy to those results in Fig. 82-right where $u_{*\mathrm{s}} > u_{*\mathrm{b}}$, $u_{*\mathrm{s}} > u_{*\mathrm{WRF}}$ for high wind speeds, resulting in m $= 0.95$.

For L (Fig. 87), the tendency of the WRF estimations L_{WRF} is to follow the sonic values particularly at the ranges where most of the results are concentrated, i.e. close to near-neutral conditions, but the scatter becomes rather large (R $= 0.56$ and m $= 0.95$) for the more extreme stable and unstable conditions.

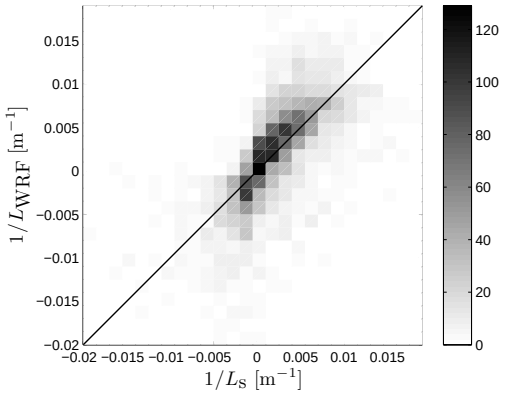

Figure 87: Comparison of the estimates of the sonic and WRF-parameterized Obukhov lengths, L_s and L_{WRF}, respectively. The colorbar indicates the amount of data in each 2D bin.

Comparison of bulk and WRF estimations

We could first compare the WRF-modeled temperatures against the observations at M2. Unfortunately, the comparison of the water-air temperature difference is not trivial, because SSTs are supplied to WRF as lower boundary conditions and remain constant for 24 hours. Therefore, we derive L_{WRF} from the parameterized fluxes, which are part of the model outputs, instead of estimating a WRF-based $\mathrm{Ri_b}$. The potential air temperature from the WRF model at 2 m, θ_{WRF}, is nevertheless compared with the observations at 13 m, $\overline{\theta_{13}}$, (Fig. 88) and shows very good agreement (R $= 0.98$ and m $= 0.99$ for N $= 18862$).

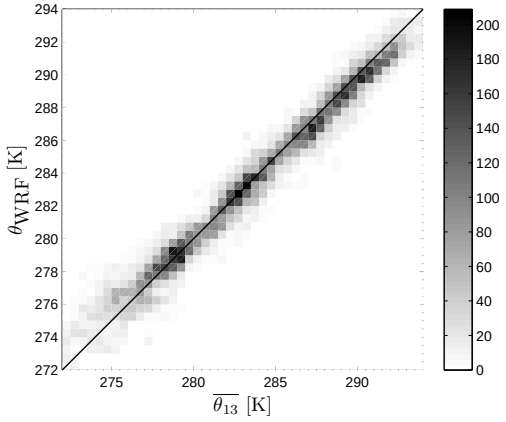

Figure 88: Air potential temperature comparison between the WRF parameterized 2-m level θ_{WRF} and the measurements at 13-m on M2 $\overline{\theta_{13}}$. The colorbar indicates the amount of data in each 2D bin.

The heat fluxes are not compared, since it is rather difficult to parameterize a bulk heat flux from the highly non-linear behavior of C_h as shown in Fig. 83. For the velocity scales, the comparisons are shown in Fig. 89. Although neither $u_{*\mathrm{WRF}}$ nor $u_{*\mathrm{b}}$ are computed from

observations of the momentum flux, both show good agreement (R $= 0.78$ and m $= 1.02$) as illustrated in Fig. 89-left. For this case, the bulk- and WRF-underestimations of u_*, which were observed when compared to the sonic values, compensate mainly because WRF, as our bulk formulation, estimates u_* close to the surface (in contrast with the sonic observations) and computes z_o using an extended version of Charnock's relation in a similar way to our bulk formulation, although in WRF an extra scaling factor of 1.59×10^{-5} m is added to the right term in Eq. (4) using $\alpha_c = 0.0185$.

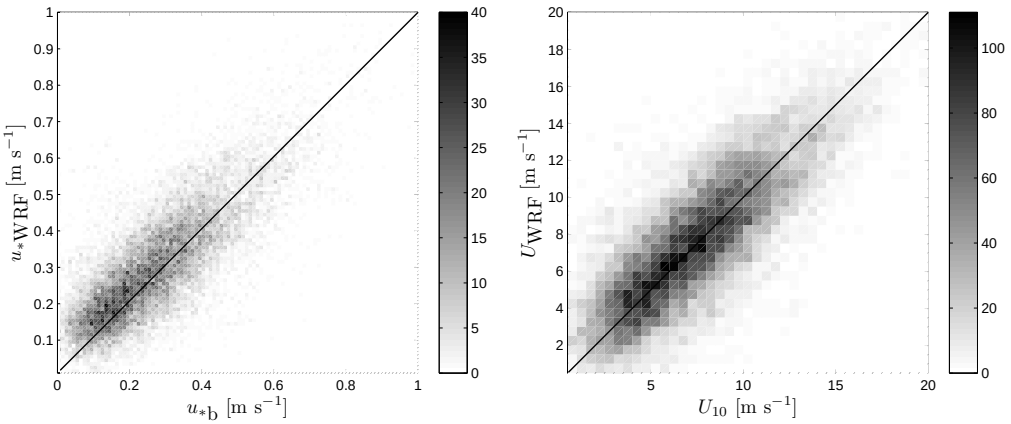

Figure 89: Comparison of the velocity scales measured by the sonic and those parameterized from WRF. (Left) WRF friction velocity u_{*WRF} against the bulk value u_{*b}. (Right) WRF wind speed at 10 m U_{WRF} against the bulk extrapolated wind speed at 10 m U_{10}. The colorbar indicates the amount of data in each 2D bin.

Since we can estimate or observe all variables in Eq. (5), this can be used to extrapolate $\overline{U_{15}}$ down to the 10-m level U_{10}. Fig. 89-right shows the comparison between the WRF-parameterized 10-m wind speed U_{WRF} and U_{10}. As for the bulk-WRF u_* comparison, the agreement is rather good (m $= 0.98$) with a slightly lower correlation (R $= 0.77$), because U_{10} is evaluated using the estimation of $u_{*\mathrm{b}}$ and more uncertainty is added from the height extrapolation.

Finally, the L-WRF estimations L_{WRF} follow closely the bulk values for the most frequently observed near-neutral ranges (Fig. 90). The scatter for all stability conditions is nevertheless large (R $= 0.51$). Due to the outliers, where the bulk method predicts very unstable and stable conditions, while WRF estimates tend to be more neutral, the relation between them is far from 1 (m $= 0.46$). However, it is important to notice that given the nature of the comparison (for these two methods L is evaluated from parameterizations, instead of using observations of the turbulent fluxes), the agreement is satisfactory.

6.5 Atmospheric stability correction for the long-term wind profile

Since the period where the bulk estimations are performed is much longer than that where the sonic measurements are available (so the amount of available bulk data is also much greater than the sonic one), the long-term stability correction is calculated from the bulk estimations and compared to that computed by the WRF model. Using the bulk estimations and Eq. (19), $\{\sigma_+, \sigma_-\} = \{0.0118\ \mathrm{m}^{-1}, 0.0170\ \mathrm{m}^{-1}\}$, and using the WRF modeled parameters $\{\sigma_+, \sigma_-\} = \{0.0113\ \mathrm{m}^{-1}, 0.0147\ \mathrm{m}^{-1}\}$.

The result of the histogram of $1/L$ estimations can then be compared to the predicted P from Eq. (17). Figure 91 shows the result for both bulk and WRF estimations, where the normalized probability density is well-predicted by the function in Eq. (17) for $\{C_+, C_-\} = \{3, 3\}$. This is a new finding, because Kelly and Gryning (2010) analyzed land observations

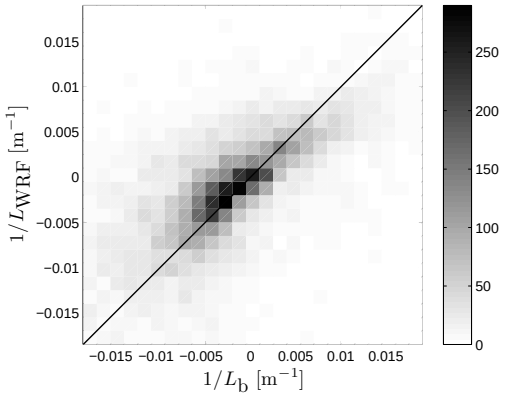

Figure 90: *Comparison of the estimates of the bulk and WRF-parameterized Obukhov lengths, L_B and L_{WRF}, respectively. The colorbar indicates the amount of data in each 2D bin.*

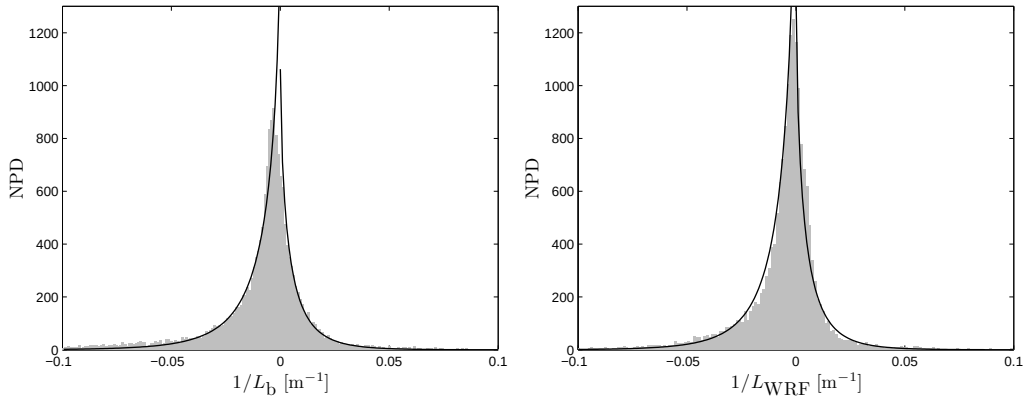

Figure 91: *Normalized probability density (NPD) of $1/L$. The estimations of $1/L$ using the bulk method (left) and the WRF outputs (right) are shown in the grey bars and the predictions from Eq. (17) in the solid black lines.*

only, where $\{C_+, C_-\} = \{1, 3\}$ fit better the measurements. The correction $\langle\psi_m\rangle$ as function of height is shown based on both the WRF model and bulk estimations in Fig. 92-left, where it is found that in both cases and on a long-term basis, the wind profile has to be corrected slightly to the stable side at Horns Rev. In the figure the 'short-term' stability corrections for the limits of neutral conditions from the wind profile study of Peña et al. (2008) (i.e. $|L| = 500$) are also illustrated and it is observed that although the long-term stability correction at Horns Rev is slightly stable, it is nearly within the near-neutral range.

The above analysis for $\langle\psi_m\rangle$ is made on a long-term basis of paired bulk/WRF estimations/outputs of the turbulent fluxes. We can also take all hourly outputs from the WRF model for a wider area and create a map of $\langle\psi_m\rangle$ for any given height by estimating $\sigma_\pm$ at each grid point. Figure 92-right shows the $\langle\psi_m\rangle$-map at 70 m AMSL for a large area of the North Sea, where it is observed that close to the coasts, the long-term wind profile has to be corrected more to the stable side than in the middle of the North Sea, with even higher 'stable' values when approaching the Great Britain island, probably due to the shadow of the land (with predominant westerly winds), which can be noticed kilometers away from the coastline.

6.6 Discussion

We use the WRF model outputs directly, without 'cleaning' the effects of the mesoscale orography and roughness for the comparison against the estimations from the sonic and bulk

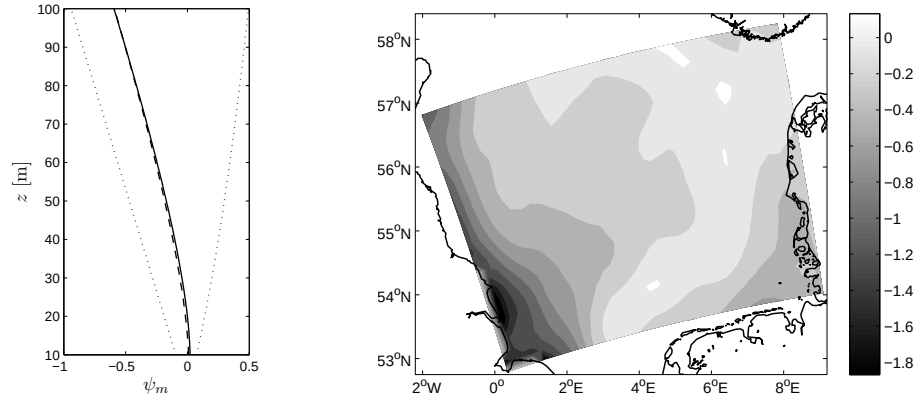

Figure 92: (Left) The wind profile stability correction ψ_m as function of height. The long-term values from the bulk and WRF estimations at Horns Rev are shown in solid and dashed lines, respectively. The dotted lines represent the theoretical values for near stable ($L = 500$ m) and near unstable atmospheres ($L = -500$ m). (Right) Map of the long-term stability correction $\langle\psi_m\rangle$ (indicated in the colorbar) at 70 m AMSL for an area of the North Sea derived from the WRF model.

methods because at this offshore site the terrain is naturally flat and homogenous and the difference between the modeled and the actual z_o is very small. When using the WRF model output over land, these 'effects' are embedded in the model results and therefore cannot be directly used for performing accurate wind power calculations. Even at Høvsøre, a flat site at the west coast of Denmark, the difference between modeled and observed z_o-values can result in errors of $\sim 50\%$ for u_*, and therefore similar errors in wind speeds and much larger in stability are found (Hahmann and Peña, 2010).

A similar bulk-sonic comparison to that in Fig. 82 was performed in Peña et al. (2008) using the Horns Rev data for a shorter period. There, a better agreement is found for u_*, because a drag criterion is used as a filter for sea states where Charnock's relation is not valid. Here we do not apply such a criterion, since we are analyzing all possible situations, but an improvement in the comparison is again found when filtering due to very high and low drag coefficients.

When the estimates of $\mathrm{Ri_b}$ and $1/L_\mathrm{s}$ are illustrated in Fig. 84, a slightly better agreement is found by comparing their relations with those from Eqs. (25) and (26) using $C_1 = 6.78$ instead of $C_1 = 10$. However, we do not estimate L_s using the 'better' C_1 value, because the sonic observations might be out of the surface MBL under a good number of atmospheric conditions, whereas the bulk estimates are performed well inside the surface MBL. Also, we cannot propose a better C_1 value than that of Grachev and Fairall (1996), because our bulk measurements are not performed with high resolution temperature sensors (± 0.354 °C), increasing the uncertainty in L particularly at near-neutral conditions where most of the observations lie and because the water temperature is not exactly the sea surface value.

The sonic u_*, computed at 50 m, is generally slightly higher than the bulk- and WRF-derived u_* values estimated close to the sea surface at high wind speeds. Although this might be due to inaccuracies in the z_o estimations from Charnock's relation, it agrees with the trend found at the Høvsøre site for unstable conditions (Gryning et al., 2007b), where u_* increases up to 60 m and then decreases following the profile shape of Zilitinkevich and Esau (2005).

A sensitivity analysis, taking into account the Charnock's parameter and the surface MBL height, was performed for the sonic-bulk comparison, based on the observed data. We notice that:

1. A change of α_c in Eq. (4) from 0.0144 (used in Sathe et al. (2011)) to 0.018 does not have effect on the statistics for the $1/L$ and u_* comparisons. It only changes the value of m from 0.80 to 0.82 for the u_* analysis, so one might assume that α_c is higher than 0.0144 at Horns Rev. However, Peña and Gryning (2008) found $\alpha_c = 0.012$ (even lower

than that in Sathe et al. (2011)) from the analysis of dimensionless wind profiles at M2. We therefore believe that the curvature in the u_* comparison is not due to under- or over-estimation of α_c, but because u_* at 50 m is higher than that close to the sea surface under unstable conditions, in agreement with the u_* profiles observed at Høvsøre under unstable conditions (Gryning et al., 2007b). Further, the WRF model uses Charnock's model with $\alpha_c = 0.0185$ and the comparison against the sonic data shows a similar underprediction of u_* by the WRF model, whereas compared to the bulk data (with $\alpha_c = 0.0144$) the agreement is better.

2. Estimating the height of the surface layer under stable conditions as 10% of the BLH (z_i), where $z_i = 0.12u_*/f_c$ and f_c is the Coriolis parameter as in Peña et al. (2008), and filtering the stable data, where the surface MBL is below the sonic height, most of the stable data ($\sim 80\%$) are filtered. The comparison of u_*, however, shows the same correlation (R$= 0.90$) with the slope m decreasing from 0.80 to 0.78. This little difference is because most of the stable data lie within the low wind speed range, where the sonic and bulk data better agree, so the effect on the comparison of u_* and $1/L$ is minimum.

6.7 Conclusions

Sonic fluxes estimated at 50 m are not always found to be representative for the surface layer, from an intercomparison between sonic observations, bulk estimations and WRF modeled and parameterized outputs at the Horns Rev offshore site. At high wind speeds, the sonic value $u_{*\mathsf{s}}$ tends to be higher than $u_{*\mathsf{b}}$ and the WRF-output $u_{*\mathsf{WRF}}$, indicating a slight increase of u_* with height in the surface MBL, since the sonic is placed at 50 m, whereas the WRF and bulk estimates are performed close to the sea surface. The highest correlations for the velocity scales are found for the sonic-bulk comparison (R $= 0.90$), where the diabatic wind profile is used in combination with Charnock's relation to estimate $u_{*\mathsf{b}}$.

It is shown that C_h and, although not explicitly, C_D strongly vary as functions of wind speed, stability and height, thus, it is difficult to directly estimate the momentum and heat fluxes from wind speed and temperature difference measurements. In unstable conditions, C_h is found to be close to $C_h = 1.3 \times 10^{-3}$, and in stable conditions, it generally gives lower values, but also under such states the relation $\overline{w'T'}_{\mathsf{s}} < \overline{w'T'}$ is expected, because of the difference between the heights where the sonic and the "bulk" instruments are placed.

Although well related (m $= 1.17$), the bulk and sonic estimations of L show that the local stability observations tend to approach neutral conditions with increasing heights in the surface MBL, which is expected, since u_* is nearly constant with height in the surface MBL, whereas the magnitude of $\overline{w'T'}$ rapidly decreases with height. This is confirmed from the sonic-WRF comparison, where $\overline{w'T'}_{\mathsf{s}}$ is closer to zero than $\overline{w'T'}_{\mathsf{WRF}}$. The trend can also be observed from the sonic-WRF L-comparison, but within the near-neutral stability range only, since whenever WRF outputs are used, the scatter largely increases in unstable and stable conditions and the statistics deteriorate (R $= 0.56$).

The relation between the bulk and WRF estimations/parameterizations is very good for temperature and velocity scales (m ~ 1) with higher correlation for the temperature (R $= 0.95$) than for the velocities (R ~ 0.78). This is somehow expected because some of the WRF outputs are partly based on bulk parameterizations in the model. The correlation between bulk-WRF L-estimations is however the lowest (R $= 0.51$), mainly because of the uncertainty in the temperature difference observations and that inherent in the model.

On a long-term basis, the stability correction to the wind profile $\langle \psi_m \rangle$ computed from the bulk estimations and the WRF outputs at Horns Rev show nearly the same results and variation with height, i.e. the long-term wind profile must be slightly corrected to the stable side. Finally, it is also estimated from the WRF outputs that the long-term wind profile generally requires a more stable correction close to the coasts than in the middle of the North Sea.

7 Vertical extrapolation methodology for offshore wind resources

Based on the relations, analysis and data that have been presented in the previous sections, it is now clear that the only way to extrapolate offshore wind speed observations to lower or higher heights is by (at least):

1. Estimating atmospheric stability measures
2. Modeling the variant sea roughness length

When the extrapolation is performed based on 'short-term' wind speed measurements, i.e. 10-min, 30-min or 1-hour time averages, one needs to estimate the atmospheric stability corrections on these same time averages and, as already mentioned, there are no means to derive atmospheric stability measures at most NORSEWInD offshore nodes. Only at M7, Fino 1, Fino 2 and Egmond aan Zee, there are observations from which one can infer atmospheric stability using bulk or gradient Richardson number methods (no sonic measurements available).

An alternative is to use NWP models' results for 'short-term' estimations of atmospheric stability, but as shown in Section 6, such models are quite inaccurate to predict 'short-term' parameters like turbulent fluxes, which are needed to estimate the Obukhov length, Eq. (6), and the corrections to the logarithmic wind profile, i.e. ϕ_m in Eqs. (7) and (8). However, as also shown in Section 6, one can use the NWP model outputs of the turbulent fluxes to obtain the long-term atmospheric stability variation and correction of the long-term vertical wind speed profile. This is the basic approach we will use for performing an analysis of the extrapolation of offshore wind resources for the NORSEWInD nodes.

7.1 Methods

Profile methods

One can in fact estimate the unknown parameters in Eq. (5), i.e. u_*, z_0 and ψ_m by fitting the equation to wind speed observations of at least two height levels and assuming both a roughness model such as that of Charnock in Eq. (4) and an expression for ψ_m. When using Charnock's model, the value of its parameter α_c has to be specified. Unless otherwise stated, we have used $\alpha_c = 0.0144$ based on Garratt (1977) and Sathe et al. (2011) and the ψ_m forms in Eqs. (7) and (8).

For the NORSEWInD lidar nodes, however, wind speed and direction measurements are performed from ∼60 m to ∼300 m at 10 levels (for the WindCube wind lidars) and at 5 levels (for the Beatrice wind lidar). In this range of heights, the profile method becomes very uncertain because the models used are valid for the surface layer only.

Long-term analysis

For the long-term analysis, we extract information from the WRF model, using the setup described in Section 6, of the surface temperature, the friction velocity, surface heat flux and BLH at each NORSEWInD node for the period of time, where data from each of the nodes were available.

Bulk and gradient Richardson number

When temperatures observations at two different levels are available, it is possible to estimate atmospheric stability as shown in Section 6 by using the bulk Richardson number (when one of the temperatures corresponds to that of the sea surface) or by the gradient Richardson number when two air temperatures are available (as shown in Appendix B) for the Fino 3 measurements.

7.2 Results

Horns Rev II

For this node we can use the profile method to estimate the turbulent fluxes, although the heights used for the u_* and L derivations are most of the time above the surface layer (66 and 86 m AMSL). Figure 93 illustrates the behavior of α (estimated at 76 m AMSL from the observations using Eq. 11) with atmospheric stability (expressed in terms of $1/L$). As expected, α increases with stable atmospheric conditions. A good number of points are shown where the profile-estimated $1/L$ value is very close to zero (indicating neutral conditions), although the correspondent α value appears within a wide range of values. These 'outliers' are artifacts of the profile method to estimate stability. Another artifact is the rather low scatter of the plot and the trend, which appears to be well predicted by the theory (the black lines). This is because α is also computed (as the turbulent fluxes in the profile method) using the wind speed measurements at the first two levels. Therefore, we bias the turbulent fluxes estimations to be in agreement with MOST.

Interestingly, α slowly becomes over-predicted by MOST with atmospheric stability (solid line). This is expected from MOST in stable conditions, where the traditional atmospheric stability correction strongly increases the vertical wind shear and over-predicts the wind speed beyond the surface layer. Therefore, we can try to predict the behavior of α with stability, but correcting for the BLH for stable conditions, as in Eq. (16). The value of z_i here used is the mean of the BLH output from the WRF model at the node's nearest grid point using the concurrent model runs from Section 6 under stable conditions ($z_i = 431$ m). As shown, by correcting the vertical wind shear for the effect of the BLH, we predict α more accurately, although the WRF BLH estimation has a large uncertainty (Peña et al., 2012).

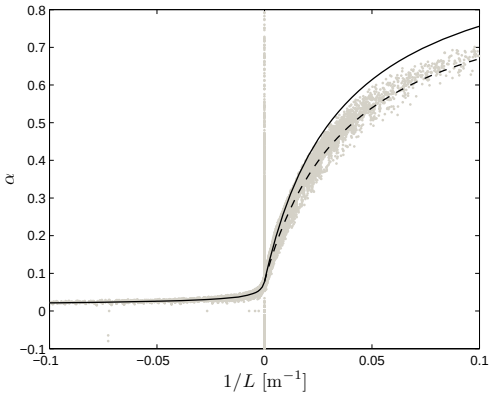

Figure 93: The behavior of α observed at 76 m AMSL at Horns Rev II with atmospheric stability. The solid and dashed lines show the theoretical expressions in Eqs. (13) and (16), respectively

Since, we do not have stability measures and the profile-derived fluxes are very inaccurate, we can also use the WRF outputs of the model setup described in Section 6 to perform a long-term stability analysis of the wind speed observations. Figure 94 (left) shows the distribution of $1/L$ values from WRF at Horns Rev (for model data that are concurrent with the observations). The theoretical distribution functions for both stable and unstable atmospheric conditions from Eq. (17), which are computed by first estimating $\sigma_\pm$ in Eq. (18) from the u_*, T and $\overline{w'\theta'_v}$ model outputs, are also plotted on top of the histograms and show very good agreement. By taken into account the frequency of stability conditions only, the centroid of the distribution is found at -0.0035 m^{-1}, which implies a general unstable predominance. However, when estimating the long-term stability correction $\langle\psi_m\rangle$ from Eq. (19), a small correction to the stable side is found (at 100 m, $\langle\psi_m\rangle = -0.37$). Therefore, the long-term vertical wind speed profile will show higher wind speeds compared to the neutral one, although unstable conditions are predominant.

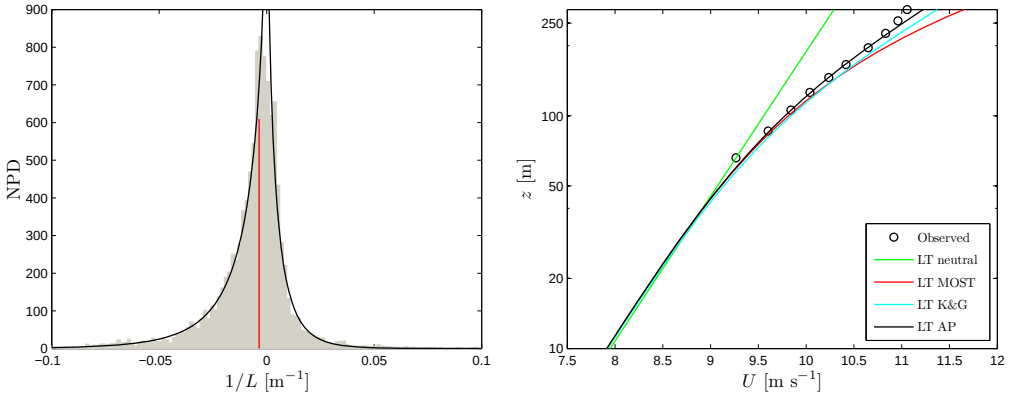

Figure 94: (left) Histograms of $1/L$ from the WRF outputs at Horns Rev II (grey bars). The theoretical distributions within the stable and unstable sides, Eq. (17), are shown in black solid lines and the centroid of the WRF $1/L$ values in the red line. (right) Long-term vertical wind speed profile from observations from the wind lidar at Horns Rev II (black circles) and the predictions using the long-term theory (see related text) for neutral conditions (LT neutral), MOST (LT MOST), the profile from Kelly and Gryning (2010) (LT K&G) and Eq. (22) (LT AP)

Figure 94 (right) illustrates the long-term vertical wind speed profile observed by the wind lidar at Horns Rev II, where all wind speeds have been averaged at each height, so they represent the term $\langle u(z) \rangle$ in Eq. (20). To perform predictions of the long-term vertical wind speed profile, we need to estimate the long-term friction velocity and stability correction, $\langle u_* \rangle$ and $\langle \psi_m \rangle$, respectively, z_o, L_m and z_m. L_m is a rather uncertain parameter (Kelly and Gryning, 2010) and by assuming a high value, we decrease its effect on the predicted vertical wind speed profile ($L_m = 1000$ m). z_m can be estimated using the WRF model outputs by averaging all BLH estimations ($z_m = 553$ m). $\langle u_* \rangle$ and z_o are estimated simultaneously using the observed long-term wind speed at the first level and Eqs. (4) and (20), i.e. MOST and Charnock's relation assuming $\langle \psi_m \rangle = 0$ ($\langle u_* \rangle = 0.28$ m s^{-1}). We do not use the mean WRF u_* value, since WRF tends to highly over-predict this output ($u_* = 0.34$ m s^{-1}). We do not use the profile-derived mean u_* either, since the wind speed levels used for its estimation are too high above the surface layer (we however find this value close to the first estimation $u_* = 0.27$ m s^{-1}). For $\langle \psi_m \rangle$, we use the above WRF derived values. Also shown in the plot are the long-term predictions (all using Charnock's relation): 1) from Eq. (20) assuming $\langle \psi_m \rangle = 0$ (LT neutral), 2) Eq. (20) (LT MOST), 3) Eq. (21) (LT K&G) and 4) Eq. (22) (LT AP). The LT neutral profile agrees only with the first height (since it is fitted to match it) and highly under-predicts the wind speed above the first wind speed level. LT MOST agrees well with the observations up to ~ 110 m AMSL and over-predicts the wind speed higher up. The two types of profiles that take into account the BLH, LT K&G and LT AP, correct for the wind speed over-prediction by MOST and show good agreement with the observations up to 250 m AMSL.

Siri

For this node, the heights used for the u_* and L derivations with the profile method are also most of the time above the surface layer (85 and 105 m AMSL). Figure 95 illustrates the behavior of α (estimated at 95 m AMSL from the observations) with atmospheric stability. α also increases with stable atmospheric conditions. Similar 'artifacts', as those for the Horns Rev II case, are found in the plot, as well as low scatter. The theoretical lines also predict the trend of the observations, agreeing well on the unstable side (negative $1/L$ values). For the stable side (positive $1/L$ values), α is also over-predicted by MOST with atmospheric stability due mostly to the BLH effect. By using Eq. (16) with z_i as the mean of the WRF BLH outputs

under stable conditions ($z_i = 454$ m), we under-predict the value of α, indicating either that the BLH value used is low or that other effects, such as baroclinicity, might be affecting the vertical wind shear at these rather high levels.

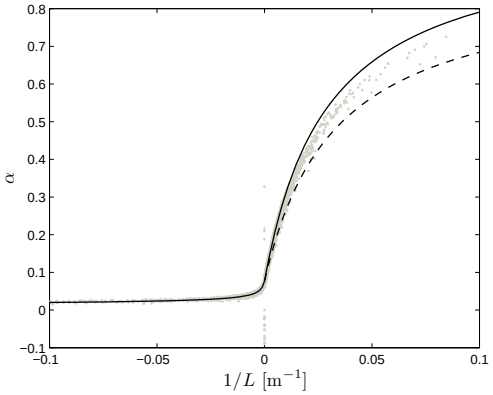

Figure 95: *Same as Fig. 93 but for the Siri wind lidar node at 95 m AMSL*

Figure 96 (left) shows the distribution of $1/L$ values from WRF at Siri. The theoretical distribution functions for both stable and unstable atmospheric conditions also show very good agreement with the histogram, although the period of analysis is less than one year with many gaps in the data due to a high decrease of wind lidar availability after four months of operation. The centroid of the distribution is found at -0.0010 m^{-1}, implying general unstable predominance. However, when estimating the long-term stability, a correction to the stable side is found (at 100 m, $\langle \psi_m \rangle = -0.72$). Therefore, the long-term vertical wind speed profile will also show higher wind speeds compared to the neutral one.

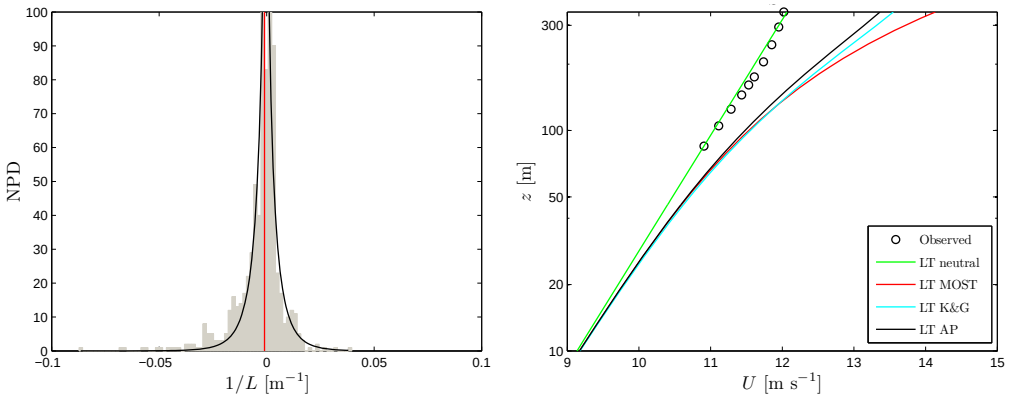

Figure 96: *As Fig. 94, but for the WRF outputs and observations from the wind lidar at Siri*

Figure 96 (right) illustrates the long-term vertical wind speed profile observed by the wind lidar at Siri. To perform predictions of the long-term vertical wind speed profile, we also assume $L_m = 1000$ m as at Horns Rev II. $z_m = 495$ m from the mean of the concurrent WRF model outputs. $\langle u_* \rangle$ and z_o are also estimated simultaneously using the observed long-term wind speed at the first level assuming $\langle \psi_m \rangle = 0$ ($\langle u_* \rangle = 0.33$ m s^{-1}). The mean WRF u_* value is also higher compared to this first-level fitted one ($u_* = 0.34$ m s^{-1}). The profile-derived mean u_* is also close to the first estimation ($u_* = 0.33$ m s^{-1}). For $\langle \psi_m \rangle$, we use the above WRF derived values. About the long-term predictions: the LT neutral profile agrees well with the observations up to 345 m AMSL, but this is mainly because u_* has been estimated high above the sea level (85 m AMSL) and might not represent the surface layer value. In other words, if more wind speed observations were available below 85 m AMSL, the LT neutral profile would not necessarily agree with the low level measurement or it would have been in

agreement with it but not with the high level ones. This is partly the reason of the apparent high disagreement between the other three profiles compared to the observations; if the LT neutral profile is moved to the left (by fitting the log profile to a lower level observation), those three other profiles might agree much better with the observations.

Taqa

For this node, the heights used for the u_* and L derivations with the profile method are most of the time above the surface layer (70 and 90 m AMSL). Figure 97 illustrates the behavior of α (estimated at 80 m AMSL from the observations) with atmospheric stability. α increases with stable atmospheric conditions, as expected. Similar 'artifacts', as those for the previous cases, are found in the plot, as well as low scatter. The theoretical lines predict the trend of the observations, agreeing well on the unstable side. For the stable side, α is again over-predicted by MOST with atmospheric stability. By using Eq. (16) with z_i as the mean of the WRF BLH outputs under stable conditions ($z_i = 333$ m), we under-predict the value of α. In this case this is mainly due to the low value used for the BLH (for the Horns Rev II case also using a high amount of data, the BLH is ∼100 m higher).

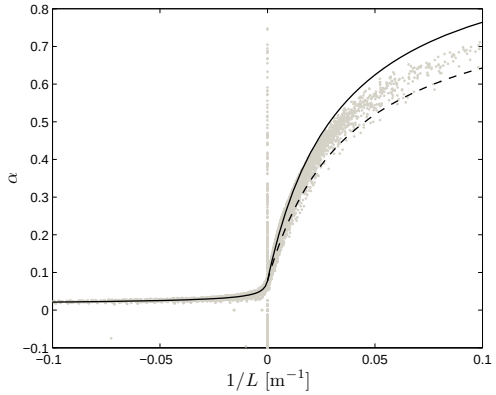

Figure 97: Same as Fig. 93 but for the Taqa wind lidar node at 80 m AMSL

Figure 98 (left) shows the distribution of $1/L$ values from WRF at Taqa. The theoretical distribution functions for both stable and unstable atmospheric conditions show very good agreement with the histogram as well. The centroid of the distribution is found at -0.0041 m^{-1}, also implying general unstable predominance. However, when estimating the long-term stability, a small correction to the stable side is again found (at 100 m, $\langle \psi_m \rangle = -0.40$).

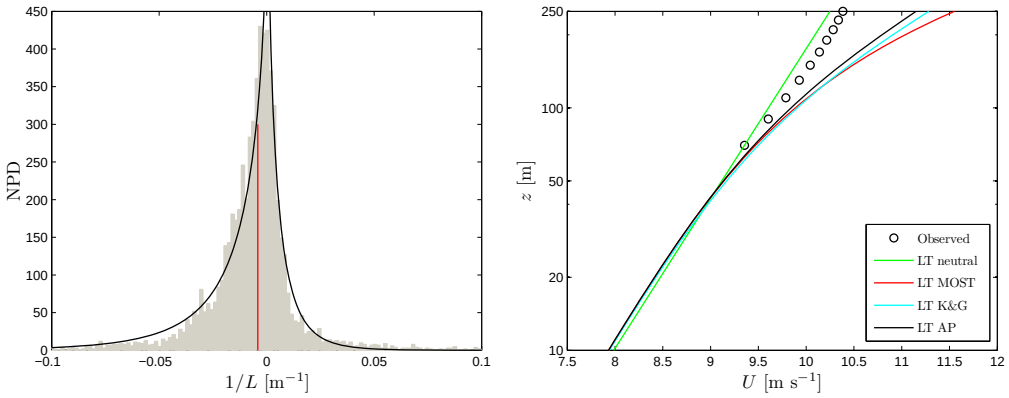

Figure 98: As Fig. 94, but for the WRF outputs and observations from the wind lidar at Taqa

Figure 98 (right) illustrates the long-term vertical wind speed profile observed by the wind lidar at Taqa. To perform predictions of the long-term vertical wind speed profile, we also

assume $L_m = 1000$ m as for the previous cases. $z_m = 508$ m from the mean of the concurrent WRF model outputs, showing the highest difference between all stability and stable only WRF BLH estimations (∼150 m). $\langle u_* \rangle$ and z_o are also estimated simultaneously using the observed long-term wind speed at the first level assuming $\langle \psi_m \rangle = 0$ ($\langle u_* \rangle = 0.28$ m s^{-1}). The mean WRF u_* value is also much higher compared to this first-level fitted one ($u_* = 0.33$ m s^{-1}). The profile-derived mean u_* is equal to the first estimation ($u_* = 0.28$ m s^{-1}). For $\langle \psi_m \rangle$, we use the above WRF derived values. About the long-term predictions: the LT neutral profile slightly under-predicts the observations up to 250 m AMSL. The other three profiles show an over-estimation of the wind speed. In this case we might be facing a similar problem to that found at Siri: the LT neutral wind profile fits well the first wind speed measurement (at 70 m AMSL), but this level might be above the surface layer. In reality, the LT neutral profile should fit much lower levels; thus it will appear more to the left in the graph, and so the other three profiles might fit better the observations. At Horns Rev II, these three profiles fit much better the observations than the LT neutral one, since the first wind speed levels are affected by the wake of the wind farm, so they already observe a reduced wind speed (similar to that found at lower levels).

Schooner

For this node, the heights used for the u_* and L derivations with the profile method are also most of the time above the surface layer (76 and 92 m AMSL). Figure 99 illustrates the behavior of α (estimated at 84 m AMSL from the observations) with atmospheric stability. α also increases with stable atmospheric conditions, as expected. Similar 'artifacts', as those for the previous cases, are found in the plot, as well as low scatter. The theoretical lines predict the trend of the observations, agreeing well on the unstable side as well. For the stable side, α is over-predicted by MOST with atmospheric stability. When using Eq. (16) with z_i as the mean of the WRF BLH outputs under stable conditions ($z_i = 289$ m–the lowest value from all nodes), we clearly under-predict the value of α. In this case, this is also mainly due to the low value used for the BLH. Unfortunately, we do not have means to evaluate these BLH estimations from the model at this node location.

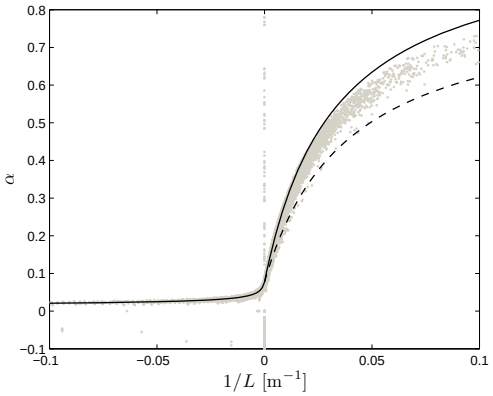

Figure 99: Same as Fig. 93 but for the Schooner wind lidar node at 84 m AMSL

Figure 100 (left) shows the distribution of $1/L$ values from WRF at Schooner. The theoretical distribution function for unstable atmospheric conditions shows very good agreement with the histogram and for the stable side the histogram shows a small peak ~ -0.025 m^{-1}. Some of the unstable data for this year of measurements might be missing as we find that the available data are about half of the total potential one. The centroid of the distribution is found at 0.0013 m^{-1}, implying–for the first time at the NORSEWInD nodes–general stable predominance. When estimating the long-term stability, a rather large correction to the stable side is found (at 100 m, $\langle \psi_m \rangle = -2.58$).

Figure 100 (right) illustrates the long-term vertical wind speed profile observed by the wind

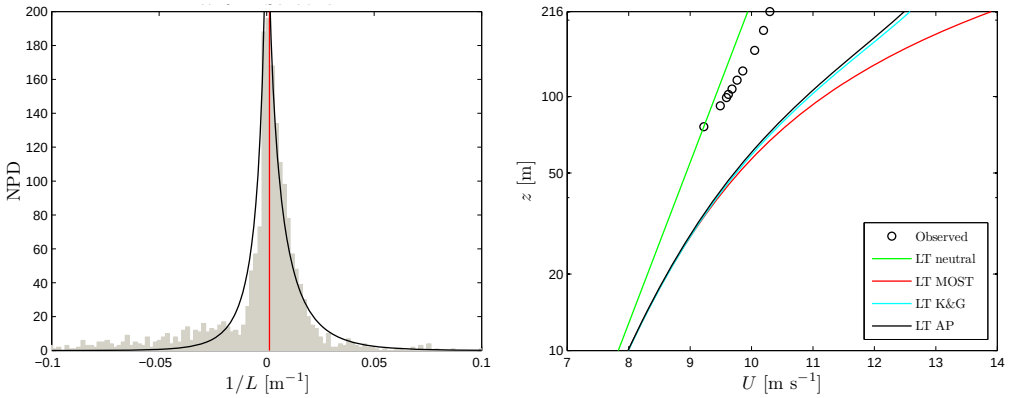

Figure 100: As Fig. 94, but for the WRF outputs and observations from the wind lidar at Schooner

lidar at Schooner. For the long-term vertical wind speed profile predictions, we also assume $L_m = 1000$ m as for the previous cases. $z_m = 309$ m from the mean of the concurrent WRF model outputs, showing the lowest value of all WRF BLH estimations. $\langle u_* \rangle$ and z_o are also estimated simultaneously using the observed long-term wind speed at the first level assuming $\langle \psi_m \rangle = 0$ ($\langle u_* \rangle = 0.27$ m s^{-1}). The mean WRF u_* gives the same value compared to this first-level fitted value. The profile-derived mean u_* is slightly lower ($u_* = 0.26$ m s^{-1}). For $\langle \psi_m \rangle$, we use the above WRF derived values. About the long-term predictions: we find the same results and problems as those from the analysis at Taqa, i.e. the LT neutral profile slightly under-predicting the observations up to 216 m AMSL and the other three profiles over-estimating the wind speed. For this case the LT K&G and LT AP profiles, which account for the BLH, show a very similar profile shape compared to the observations, whereas the LT neutral and LT MOST profile show much lower and higher vertical wind shears, respectively.

Jacky

For this node, the heights used for the u_* and L derivations with the profile method are probably in the upper boundary of the marine surface layer (60 and 80 m AMSL). Figure 101 illustrates the behavior of α (estimated at 70 m AMSL from the observations) with atmospheric stability. Although the amount of data is very few, α is observed to increase with stable atmospheric conditions. Similar 'artifacts', as those for the previous cases, are found in the plot. The theoretical lines predict the trend of the observations, agreeing well on the unstable side. For the stable side, α is over-predicted by MOST with atmospheric stability and when using Eq. (16) with z_i as the mean of the WRF BLH outputs under stable conditions ($z_i = 555$ m), we find very good agreement with the observations.

Figure 102 (left) shows the distribution of $1/L$ values from WRF at Jacky. It is clearly observed that the lack of observations increases the uncertainty and error of the long-term analysis at this node. The theoretical distribution function for unstable and stable atmospheric conditions anyway show rather good agreement with the histogram. The centroid of the distribution is found at -0.0039 m^{-1}, implying general unstable predominance (the measurements are performed between July and October where unstable conditions are often observed). When estimating the long-term stability, a slight correction to the unstable side–for the first time at a NORSEWInD node–is found (at 100 m, $\langle \psi_m \rangle = 0.40$). Therefore, the shape of the long-term vertical wind speed profiles should not differ much from the neutral log wind profile.

Figure 102 (right) illustrates the long-term vertical wind speed profile observed by the wind lidar at Jacky. For this node, the wind lidar measurements are probably affected by the platform where the instrument is deployed, as the first 5–6 levels show a characteristic flow distorted shape. Unfortunately, there is no installation report available from this node.

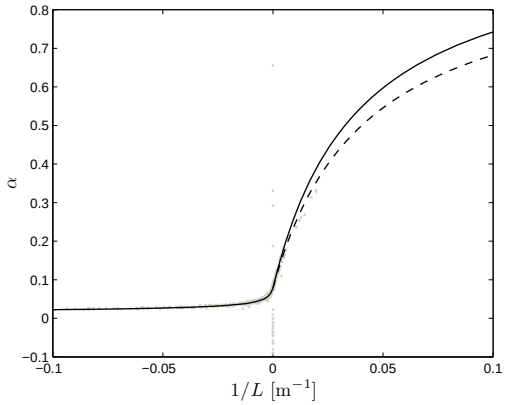

Figure 101: *Same as Fig. 93 but for the Jacky wind lidar node at 70 m AMSL*

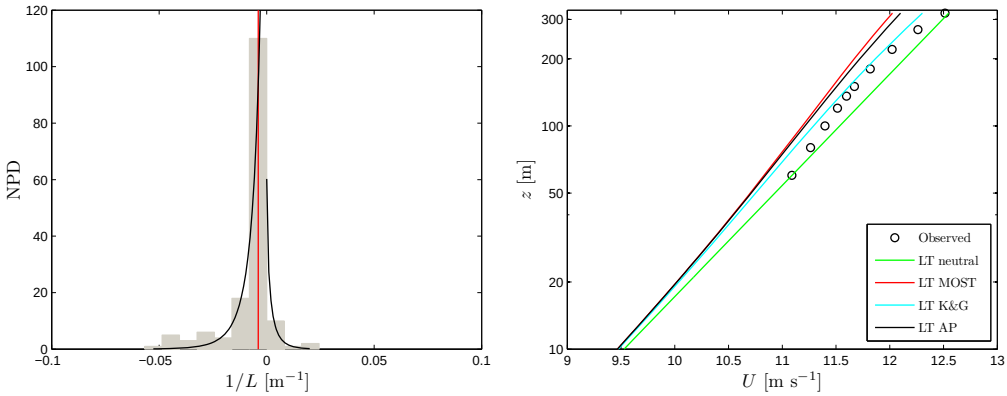

Figure 102: *As Fig. 94, but for the WRF outputs and observations from the wind lidar at Jacky*

Therefore, the analysis of the long-term vertical wind speed profile predictions does not allow for characterizing the wind profile at Jacky. For completeness, here we present the values used for the profiles in the plot. As for the previous cases, we assume $L_m = 1000$ m. $z_m = 592$ m from the mean of the concurrent WRF model outputs. $\langle u_* \rangle$ and z_o estimated simultaneously using the observed long-term wind speed at the first level assuming $\langle \psi_m \rangle = 0$ gives $\langle u_* \rangle = 0.35$ m s^{-1}). The mean WRF u_* gives a higher value ($u_* = 0.39$ m s^{-1}). The profile-derived mean u_* is equal to the WRF derived value. For $\langle \psi_m \rangle$, we also use the above WRF derived values.

Beatrice

At Beatrice, the heights used for the u_* and L derivations with the profile method are also in the boundary of the surface layer (52.5 and 75.5 m AMSL). Figure 103 illustrates the behavior of α (estimated at 64 m AMSL from the observations) with atmospheric stability. As expected, α increases with stable atmospheric conditions. Similar 'artifacts', as those for the previous cases, are found in the plot, as well as low scatter. The theoretical lines predict the trend of the observations, agreeing well on the unstable side. For the stable side, α is over-predicted by MOST with atmospheric stability. When using Eq. (16) with z_i as the mean of the WRF BLH outputs under stable conditions ($z_i = 538$ m–the higuest value from all nodes), the agreement of the predicted α value with the observations is very high.

Figure 104 (left) shows the distribution of $1/L$ values from WRF at Beatrice. The theoretical distribution function for unstable and stable atmospheric conditions show very good agreement with the histogram, although this is less smooth in the unstable side. This is probably due to the short period of measurements for this node (about three months), although the

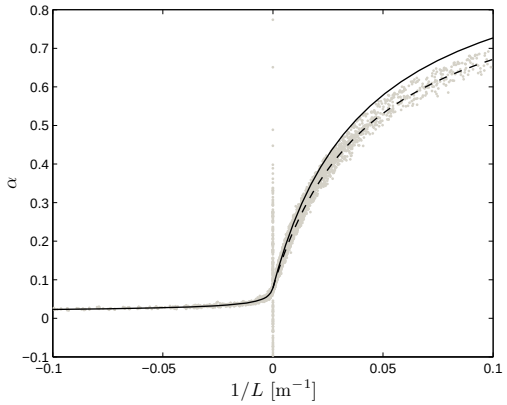

Figure 103: *Same as Fig. 93 but for the Beatrice wind lidar node at 64 m AMSL*

amount of available data is high. The centroid of the distribution is found at -0.0058 m^{-1}, implying general predominance of unstable conditions. However, when estimating the long-term stability, a slight correction to the stable side is found (at 100 m, $\langle \psi_m \rangle = -0.16$).

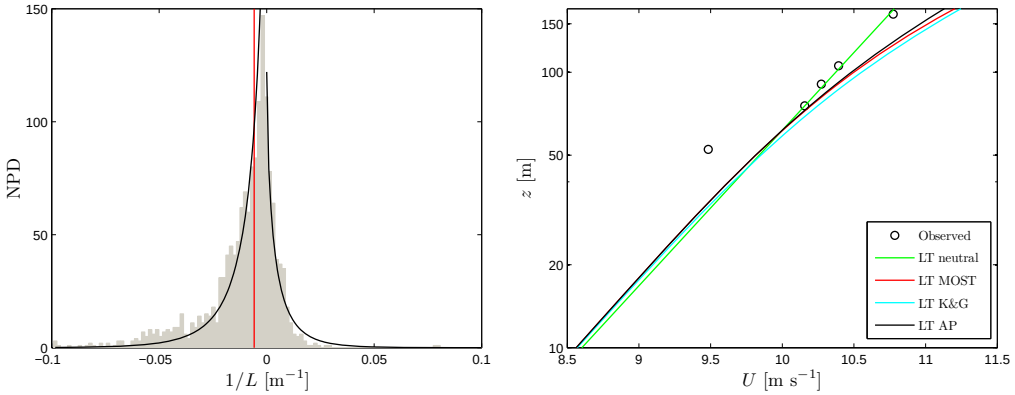

Figure 104: *As Fig. 94, but for the WRF outputs and observations from the wind lidar at Beatrice*

Figure 104 (right) illustrates the long-term vertical wind speed profile observed by the wind lidar at Beatrice. For this case, it is evident that the first wind speed measurement (52.5 m AMSL) does not follow the other levels and therefore we avoid it for the analysis (we do not have an installation report for this wind lidar, so it is difficult to relate this effect to distortion or shading issues). For the long-term vertical wind speed profile predictions, we also assume $L_m = 1000$ m as for the previous cases. $z_m = 727$ m from the mean of the concurrent WRF model outputs, showing the highest value of all WRF BLH estimations. $\langle u_* \rangle$ and z_o are then estimated simultaneously using the observed long-term wind speed at the second level assuming $\langle \psi_m \rangle = 0$ ($\langle u_* \rangle = 0.31$ m s^{-1}). The mean WRF u_* gives a higher value compared to this second-level fitted one ($u_* = 0.37$ m s^{-1}). The profile-derived mean u_* is much lower ($u_* = 0.26$ m s^{-1}), because the first wind speed level was used for the profile method. For $\langle \psi_m \rangle$, we use the above WRF derived values. About the long-term predictions: we find the same results and problems as those from the analysis at Taqa and Schooner, although in this case the LT neutral profile predicts well the observations up to 162.5 m AMSL. The other three profiles over-estimate the wind speed. For this case the LT K&G and LT AP profiles are very close to the LT MOST one, since the $\langle \psi_m \rangle$ term is very small all the way up to the highest level.

Utsira

For this node, the heights used for the u_* and L derivations with the profile method might also be outside the surface layer (67 and 80 m AMSL). Figure 105 illustrates the behavior of α (estimated at 73 m AMSL from the observations) with atmospheric stability. As expected, α increases with stable atmospheric conditions. Similar 'artifacts', as those for the previous cases, are found in the plot, as well as low scatter. The theoretical lines predict the trend of the observations, agreeing well on the unstable side. For the stable side, α is over-predicted by MOST with atmospheric stability. When using Eq. (16) with z_i as the mean of the WRF BLH outputs under stable conditions ($z_i = 454$ m), the agreement of the predicted α value with the observations is high.

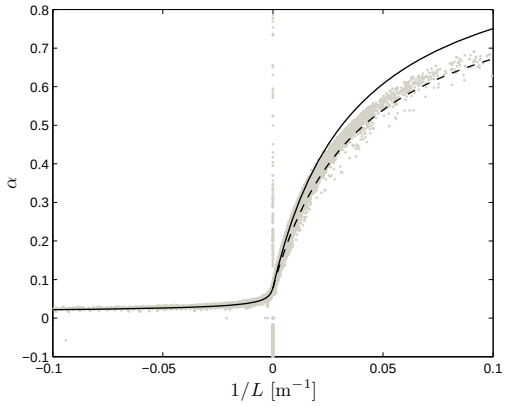

Figure 105: *Same as Fig. 93 but for the Utsira wind lidar node at 73 m AMSL*

Figure 106 (left) shows the distribution of $1/L$ values from WRF at the Utsira island. The theoretical distribution function for unstable and stable atmospheric conditions show very good agreement with the histogram. The centroid of the distribution is found at -0.0024 m^{-1}, implying general predominance of unstable conditions. However, as in many of the previous cases, when estimating the long-term stability, a slight correction to the stable side is found (at 100 m, $\langle \psi_m \rangle = -0.25$).

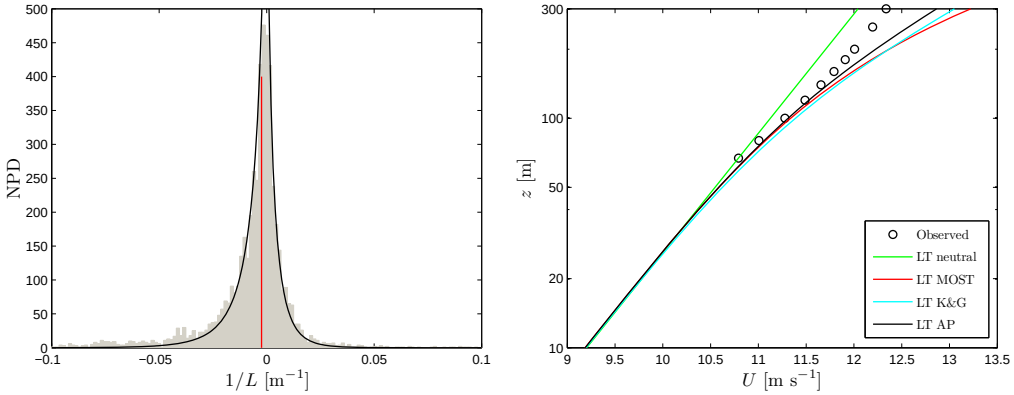

Figure 106: *As Fig. 94, but for the WRF outputs and observations from the wind lidar at Utsira*

Figure 106 (right) illustrates the long-term vertical wind speed profile observed by the wind lidar at Utsira. For this case, it is not evident that the first wind speed measurements are affected by the orography of the island, although speed ups should be measured up to 150–200 m ALL as shown in Appendix C. Therefore the real offshore wind profile at Utsira will show lower wind speeds in the first measurement levels. For the long-term vertical wind speed profile predictions, we also assume $L_m = 1000$ m as for the previous cases.

$z_m = 595$ m from the mean of the concurrent WRF model outputs. $\langle u_* \rangle$ and z_o are then estimated simultaneously using the observed long-term wind speed at the first level assuming $\langle \psi_m \rangle = 0$ ($\langle u_* \rangle = 0.33$ m s^{-1}). The mean WRF u_* gives a much higher value compared to this first-level fitted one ($u_* = 0.39$ m s^{-1}). The profile-derived mean u_* is just slightly higher ($u_* = 0.34$ m s^{-1}). For $\langle \psi_m \rangle$, we use the above WRF derived values. About the long-term predictions: we find the same results and problems as those from the analysis at Taqa, Schooner and Beatrice, although in this case the LT MOST, LT K&G and LT AP profiles predict well the observations up to ~ 150 m AMSL, over-predicting the wind speed higher up.

Greater Gabbard

For all met mast nodes, we need to restrict the analysis to winds higher than 2 m s^{-1}, because in many cases, where this is lower than 2–3 m s^{-1}, the measurement performed at some of the cup anemometers on the mast becomes suspiciously too low compared to the others. The heights used for the u_* and L derivations with the profile method are in the boundary of the surface layer (42.5 and 52.5 m AMSL), although this is a mast node (most masts have measurements close to the surface). Figure 107 illustrates the behavior of α (estimated at 47.5 m AMSL from the observations) with atmospheric stability. As expected, α increases with stable atmospheric conditions. Similar 'artifacts', as those for the previous cases, are found in the plot, as well as low scatter. The theoretical lines predict the trend of the observations, agreeing well on the unstable side. For the stable side, α is over-predicted by MOST with atmospheric stability. When using Eq. (16) with z_i as the mean of the WRF BLH outputs under stable conditions ($z_i = 312$ m), the agreement of the predicted α value with the observations is very good.

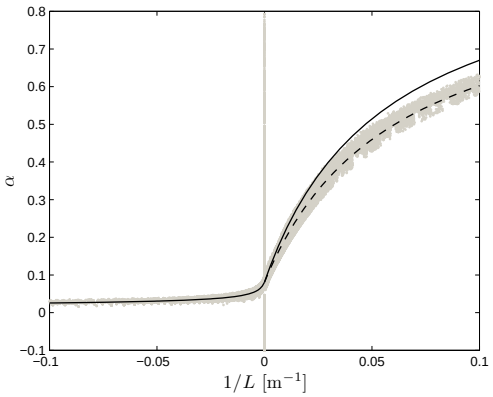

Figure 107: *Same as Fig. 93 but for the Greater Gabbard met mast node at 47.5 m AMSL*

Figure 108 (left) shows the distribution of $1/L$ values from WRF at the Greater Gabbard met mast. The theoretical distribution function for unstable and stable atmospheric conditions shows good agreement with the histogram, although the function on the stable side slightly under-predicts the frequency at ∼0.03–0.04 m^{-1}. The centroid of the distribution is found at -0.0021 m^{-1}, indicating general predominance of unstable conditions. However, as for most of the previous cases, when estimating the long-term stability, a correction to the stable side is found (at 80 m, $\langle \psi_m \rangle = -0.74$).

Figure 108 (right) illustrates the long-term vertical wind speed profile observed by the met mast at Greater Gabbard. The first three observations show a different and slightly lower wind profile than the two upper most ones. For the long-term vertical wind speed profile predictions, we also assume $L_m = 1000$ m as for the previous cases. $z_m = 446$ m from the mean of the concurrent WRF model outputs. $\langle u_* \rangle$ and z_o are estimated simultaneously using the observed long-term wind speed at the first level assuming $\langle \psi_m \rangle = 0$ ($\langle u_* \rangle = 0.28$ m s^{-1}). The mean WRF u_* gives a higher value compared to this first-level fitted one

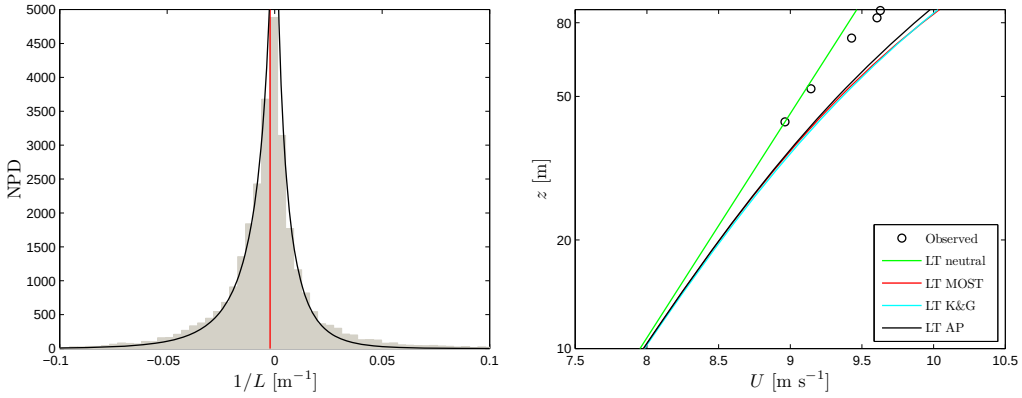

Figure 108: As Fig. 94, but for the WRF outputs and observations from the met mast at Greater Gabbard

($u_* = 0.32$ m s^{-1}). The profile-derived mean u_* gives a similar value to that derived from the first-level ($u_* = 0.27$ m s^{-1}). For $\langle\psi_m\rangle$, we use the above WRF derived values. About the long-term predictions: the LT neutral profile slightly under-predicts the wind speed all the way up to 86.5 m AMSL, whereas the other three profiles overestimate the wind speed at all levels, which might be due to the method performed to estimate u_*–from the neutral log profile with a measurement above the surface layer–as for some of the wind lidar nodes.

Lillgrund

The measurement at 13 m AMSL (the closest observation to the surface) is in this data set systematically wrong (showing a constant low value), thus, it is not used for the analysis. The heights used for the u_* and L derivations with the profile method are most of the time inside the surface layer (20 and 40 m AMSL). Figure 109 illustrates the behavior of α (estimated at 30 m AMSL from the observations) with atmospheric stability. As expected, α increases with stable atmospheric conditions. Similar 'artifacts', as those for the previous cases, are found in the plot, as well as low scatter. The theoretical lines predict the trend of the observations, agreeing well on the unstable side. For the stable side, α is over-predicted by MOST with atmospheric stability. When using Eq. (16) with z_i as the mean of the WRF BLH outputs under stable conditions ($z_i = 326$ m), the agreement of the predicted α value with the observations is better, although α remains over-predicted.

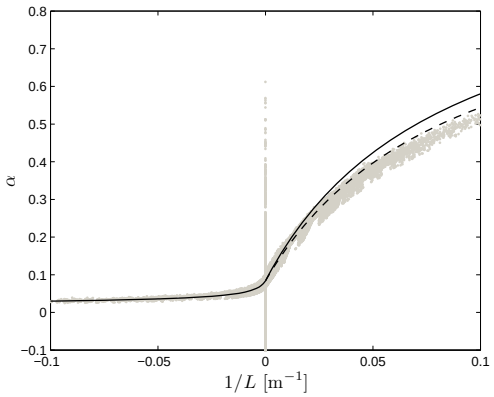

Figure 109: Same as Fig. 93 but for the Lillgrund met mast node at 30 m AMSL

Figure 110 (left) shows the distribution of $1/L$ values from WRF at the Lillgrund met mast. The theoretical distribution function for unstable and stable atmospheric conditions shows good agreement with the histogram, although at Lillgrund we also observe a peak

on the unstable range (~ -0.05 m^{-1}) as at Schooner. The centroid of the distribution is found at -0.0031 m^{-1}, indicating general predominance of unstable conditions. However, as in most of the previous cases, when estimating the long-term stability, a correction to the stable side is found (at 60 m, $\langle\psi_m\rangle = -0.74$).

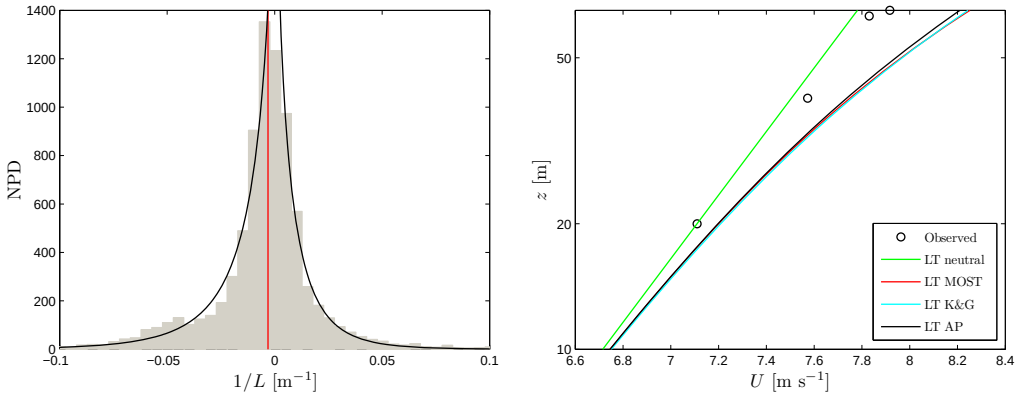

Figure 110: As Fig. 94, but for the WRF outputs and observations from the met mast at Lillgrund

Figure 110 (right) illustrates the long-term vertical wind speed profile observed at the met mast at Lillgrund. For this case, a good amount of observations are affected by the wind farm north east of the mast and therefore the profiles are not expected to be in agreement with the theory. The long-term analysis includes the wake affected wind, since we only have one year of data. For the long-term vertical wind speed profile predictions, we also assume $L_m = 1000$ m as for the previous cases. $z_m = 424$ m from the mean of the concurrent WRF model outputs. $\langle u_*\rangle$ and z_o are then estimated simultaneously using the observed long-term wind speed at the second level assuming $\langle\psi_m\rangle = 0$ ($\langle u_*\rangle = 0.23$ m s^{-1}). The mean WRF u_* gives a much higher value compared to this second-level fitted one ($u_* = 0.29$ m s^{-1}). The profile-derived mean u_* gives the same value as the second-level fitted one. For $\langle\psi_m\rangle$, we use the above WRF derived values. About the long-term predictions: except from the LT neutral profile, which slighlty underestimates the wind speed all the way up to 70 m AMSL, the other profiles overestimate the wind speed, but this might be also due to the wake effect of the wind farm on the measurements.

Fino 1

For this node, the heights used for the u_* and L derivations with the profile method are most of the times inside the surface layer (33 and 40 m AMSL). Figure 111 illustrates the behavior of α (estimated at 41.5 m AMSL from the observations) with atmospheric stability. As expected, α increases with stable atmospheric conditions. Similar 'artifacts', as those for the previous cases, are found in the plot, as well as low scatter. In this particular case, the theoretical lines predict the trend of the observations, agreeing well on the unstable and stable sides. In the stable side, α is slightly under-predicted when using Eq. (16) with z_i as the mean of the WRF BLH outputs under stable conditions ($z_i = 393$ m). This might be due a too low BLH applied in stable conditions, but it might also be due to general higher vertical wind shears measured at some of the sectors at Fino 1 (see Section 4.2); the flow distortion effects at the 33-m height measurements are, for example, higher than those at the 40-m level due to the helipad/platform.

Figure 112 (left) shows the distribution of $1/L$ values from WRF at the Fino 1 met mast. The theoretical distribution function for unstable and stable atmospheric conditions show very good agreement with the histogram. The centroid of the distribution is found at -0.0021 m^{-1}, implying general predominance of unstable conditions. However, as for most of the previous

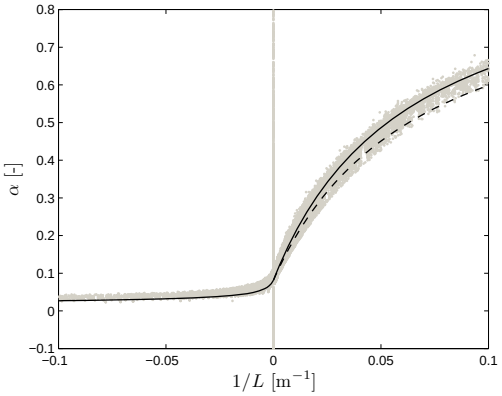

Figure 111: *Same as Fig. 93 but for the Fino 1 met mast node at 41.5 m AMSL*

cases, when estimating the long-term stability, a correction to the stable side is found (at 100 m, $\langle\psi_m\rangle = -0.76$).

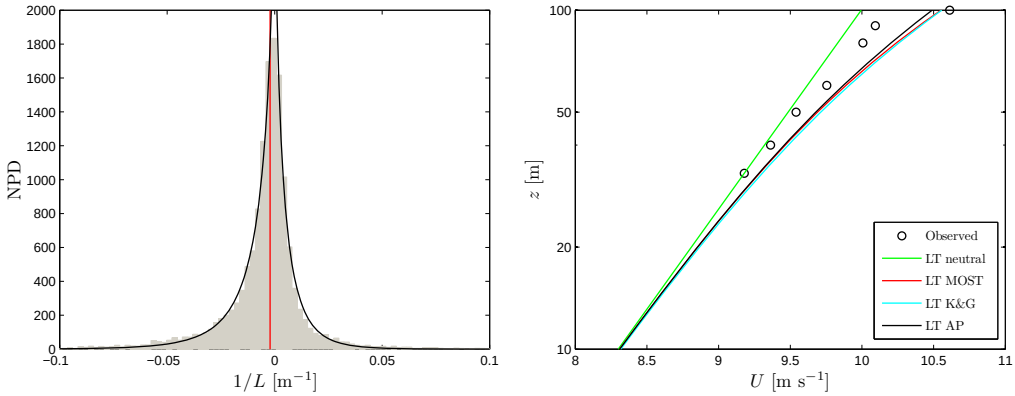

Figure 112: *As Fig. 94, but for the WRF outputs and observations from the met mast at Fino 1*

Figure 112 (right) illustrates the long-term vertical wind speed profile observed at the Fino 1 met mast. Here it is evident the problems of flow distortion on the measurements and thus it is difficult to judge how the observed profile from a non-distorted data set would look like. Many studies correct the flow distortion on the side-mounted cup anemometers at Fino 1 by assuming that the top one is correct, although this measurement is performed on a rod cage and, therefore, it might be even more flow distorted. For the long-term vertical wind speed profile predictions, we however perform the analysis assuming $L_m = 1000$ m as for the previous cases and $z_m = 534$ m from the mean of the concurrent WRF model outputs. $\langle u_*\rangle$ and z_o are estimated simultaneously using the observed long-term wind speed at the first level assuming $\langle\psi_m\rangle = 0$ ($\langle u_*\rangle = 0.29$ m s^{-1}). The mean WRF u_* gives a higher value compared to this first-level fitted one ($u_* = 0.34$ m s^{-1}). The profile-derived mean u_* is just slightly lower ($u_* = 0.28$ m s^{-1}). For $\langle\psi_m\rangle$, we use the above WRF derived values. About the long-term predictions: the LT neutral profile under-predicts the wind speed all the way up to 100 m AMSL, as usual. The other three profiles show the same behavior and values, generally over-predicting the wind speed, although they show a slightly lower long-term wind speed at the 100-m level (which might be the most true or distorted one).

At Fino 1, as for the following NORSEWInD met mast nodes, there are means to derive the atmospheric stability from observations. Here, we would have preferred to estimate a bulk Richardson number instead of a gradient one, since as shown in Lange et al. (2004), the extrapolated winds using bulk measurements compared better to observations than the gradient methods. However, the measurements of sea temperatures show few good data.

Therefore, we estimate the stability corrections from the temperatures at 30 and 40 m AMSL, wind speeds at 33 and 40 m AMSL, relative humidity at 33 m AMSL and pressure at 20 m AMSL, based on the gradient Richardson number (shown in Appendix B), assuming the relations between this and the Obukhov length as in Lange et al. (2004). We then compare the extrapolated winds at 100 m AMSL using three different methodologies to the observations, shown as "REAL" in Fig. 113. We illustrate such comparisons in scatter plots, with the same amount of 10-min data (N), so that the results can be inter-compared. For all comparisons, a linear regression through origin is performed (which gives the mean wind speed bias) and the linear correlation coefficient (R^2) is presented.

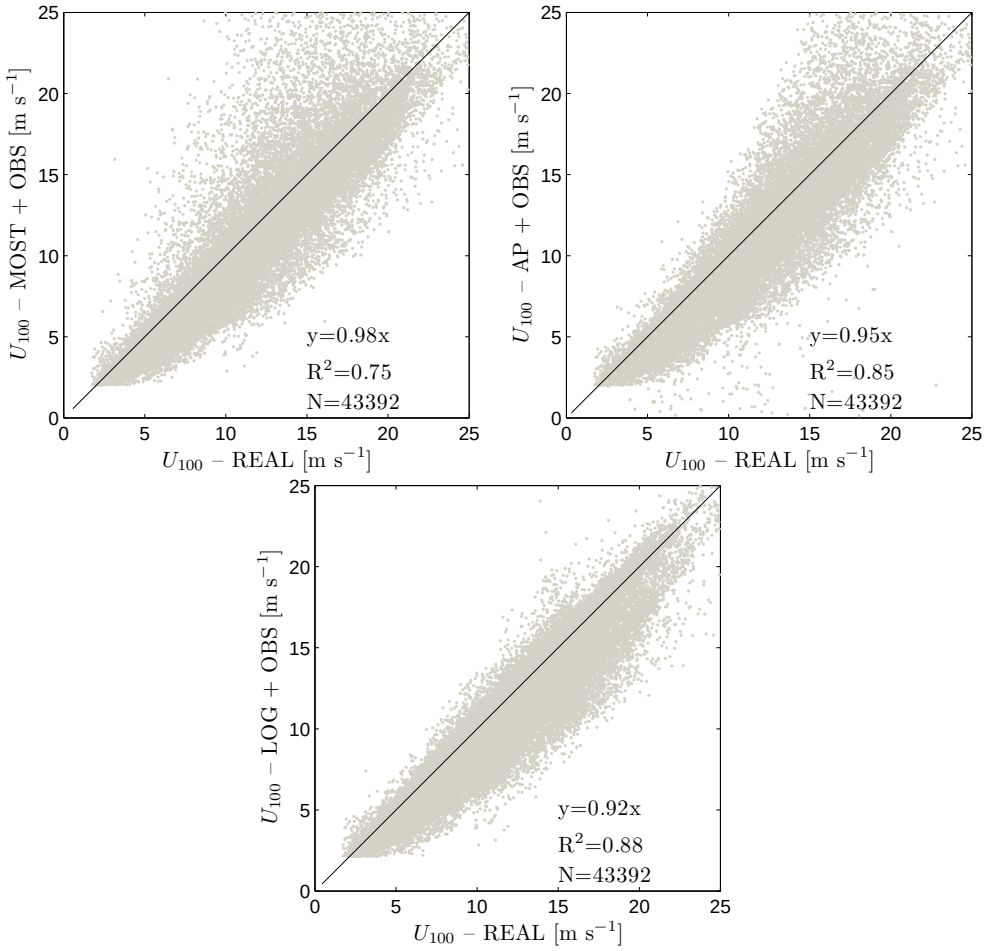

Figure 113: Comparison of the 100 m wind speed observed at the Fino 1 met mast against three estimated values (see text for details)

The first method "MOST + OBS" estimates first u_* and z_o combining MOST and Charnock's relation with the first wind speed measurement at 33 m AMSL, i.e. Eqs. (5) and (4) with $\alpha_c = 0.0144$ as in Garratt (1977) and Sathe et al. (2011), and ψ_m estimated at that level. Then using the same set of equations, the 100-m wind is computed but with the correspondent 100-m ψ_m value. "AP + OBS" applies a similar methodology, but the 100-m wind is estimated using Eq. (15) instead of (5). The BLH in this case is estimated as $z_i = 0.12u_*/f_c$ in stable conditions following the results in Peña et al. (2008). The third method "LOG + OBS" is also similar to the fist one but ψ_m is always assumed to be zero when estimating u_* and the 100-m wind. For Fino 1, the results show that accounting for stability either using MOST or the profile in Peña et al. (2008), the mean biases will be higher but the correlations lower than assuming a neutral atmosphere. In this case, such "striking" and dubious results might be due to 1) very inaccurate estimations of atmospheric stability,

because of high distorted measurements and inaccurate sensors 2) the 100-m wind is out of the surface layer and 3) u_* is estimated at 33 m so it might not represent the surface layer value either.

Fino 2

For this node, the heights used for the u_* and L derivations with the profile method might also be in the boundary of the surface layer (32 and 42 m AMSL), as for Fino 1. Figure 114 illustrates the behavior of α (estimated at 37 m AMSL from the observations) with atmospheric stability. α also increases with stable atmospheric conditions. Similar 'artifacts', as those for the previous cases, are found in the plot, as well as low scatter. The theoretical lines predict the trend of the observations, agreeing well on the unstable side. For the stable side, α is over-predicted by MOST with atmospheric stability. When using Eq. (16) with z_i as the mean of the WRF BLH outputs under stable conditions ($z_i = 298$ m), the agreement of the predicted α value with the observations is rather high.

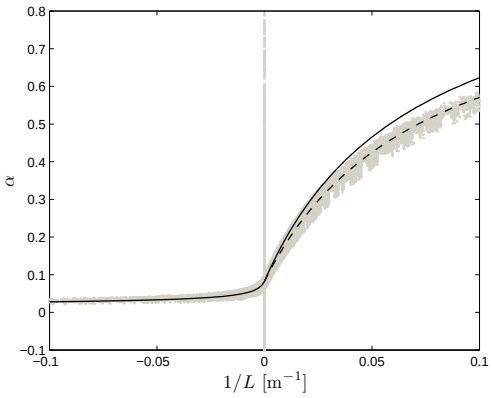

Figure 114: *Same as Fig. 93 but for the Fino 2 met mast node at 37 m AMSL*

Figure 115 (left) shows the distribution of $1/L$ values from WRF at the Fino 2 met mast. The theoretical distribution functiosn for unstable and stable atmospheric conditions show very good agreement with the histogram, which is interesting since this is the first time where such analysis has been performed in the Baltic Sea for a long data set. The centroid of the distribution is found at -0.0009 m^{-1}, implying that the atmosphere is very close to neutral. When estimating the long-term stability, a high correction to the stable side is found (at 100 m, $\langle \psi_m \rangle = -1.65$).

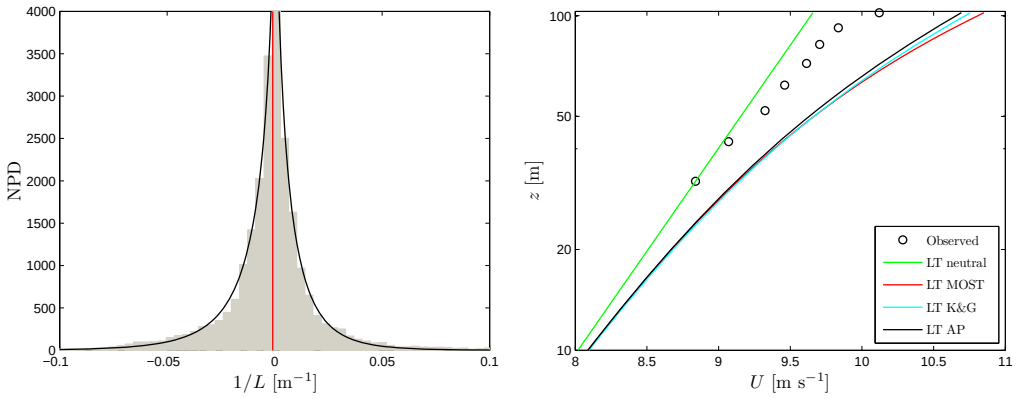

Figure 115: *As Fig. 94, but for the WRF outputs and observations from the met mast at Fino 2*

Figure 115 (right) illustrates the long-term vertical wind speed profile observed at the Fino 2

met mast. Here it is also evident the problems of flow distortion on the measurements, similarly to the results at Fino 1. For the long-term vertical wind speed profile predictions, we perform the analysis assuming $L_m = 1000$ m as for the previous cases and $z_m = 419$ m from the mean of the concurrent WRF model outputs. $\langle u_* \rangle$ and z_o are estimated simultaneously using the observed long-term wind speed at the first level assuming $\langle \psi_m \rangle = 0$ ($\langle u_* \rangle = 0.28$ m s^{-1}). The mean WRF u_* gives a higher value compared to this first-level fitted one ($u_* = 0.31$ m s^{-1}). The profile-derived mean u_* shows the same value as that from fitting the first level. For $\langle \psi_m \rangle$, we use the above WRF derived values. About the long-term predictions: the LT neutral profile under-predicts the wind speed all the way up to 102 m AMSL, whereas the other three profiles show the same behavior and values, over-predicting the wind speed at all levels. Here u_* is estimated from the measurements at 32 m AMSL which might be simply too high above the surface.

For Fino 2, the means to derive stability come from using a gradient Richardson number, similarly to that at Fino 1. Here we estimate the stability corrections from the temperatures at 30 and 40 m AMSL, wind speeds at 32 and 42 m AMSL, relative humidity at 30 m AMSL and pressure at 30 m AMSL. When comparing the extrapolated winds at 102 m using the three different methodologies as for Fino 1 (see Fig. 116), we found a even better result (in terms of correlation) by assuming neutral atmospheric conditions than correcting for stability for either MOST or the profiles correcting for the BLH effect. In fact, "MOST + OBS" shows a high amount of scatter above the 1:1 line for high wind speeds. This is due to over-prediction of the stability correction in stable conditions. However, in this case, we can be very skeptical about the stability measures since we should observe such over-estimations mostly in the low wind speed range where stable conditions are predominant. Thus, a stable correction is probably been applied to near-neutral winds (typical of high wind speeds). This is corroborated by analyzing the results of "AP + OBS" which account for the BLH effect and where most of these high winds are not corrected.

Egmond aan Zee

For this node, the second height used for the u_* and L derivations with the profile method might also be outside the surface layer, although the first is nearly always inside (21 and 70 m AMSL). Figure 117 illustrates the behavior of α (estimated at 45.5 m AMSL from the observations) with atmospheric stability. As expected, α increases with stable atmospheric conditions. Similar 'artifacts', as those for the previous cases, are found in the plot, as well as low scatter. The theoretical lines predict the trend of the observations, agreeing well on the unstable side. For the stable side, α is over-predicted by MOST with atmospheric stability. When using Eq. (16) with z_i as the mean of the WRF BLH outputs under stable conditions ($z_i = 350$ m), the agreement of the predicted α value is rather good.

Figure 118 (left) shows the distribution of $1/L$ values from WRF at the Egmond aan Zee met mast. The theoretical distribution function for unstable and stable atmospheric conditions shows very good agreement with the histogram. The centroid of the distribution is found at -0.0030 m^{-1}, implying general predominance of unstable conditions. However, as in many of the previous cases, when estimating the long-term stability, a slight correction to the stable side is found (at 100 m, $\langle \psi_m \rangle = -0.68$).

Figure 118 (right) illustrates the long-term vertical wind speed profile observed at the Egmond aan Zee met mast. For this case, the observations do not show any evident flow distortion, since the measurements are selected based on the less-distorted cup anemometer on the mast. For the long-term vertical wind speed profile predictions, we also assume $L_m = 1000$ m as for the previous cases. $z_m = 456$ m from the mean of the concurrent WRF model outputs. $\langle u_* \rangle$ and z_o are then estimated simultaneously using the observed long-term wind speed at the first level assuming $\langle \psi_m \rangle = 0$ ($\langle u_* \rangle = 0.26$ m s^{-1}). The mean WRF u_* gives a much higher value compared to this first-level fitted one ($u_* = 0.32$ m s^{-1}). The profile-derived mean u_* is just slightly higher ($u_* = 0.27$ m s^{-1}). For $\langle \psi_m \rangle$, we use the above WRF derived values. About the long-term predictions: the LT neutral profile under-predicts the

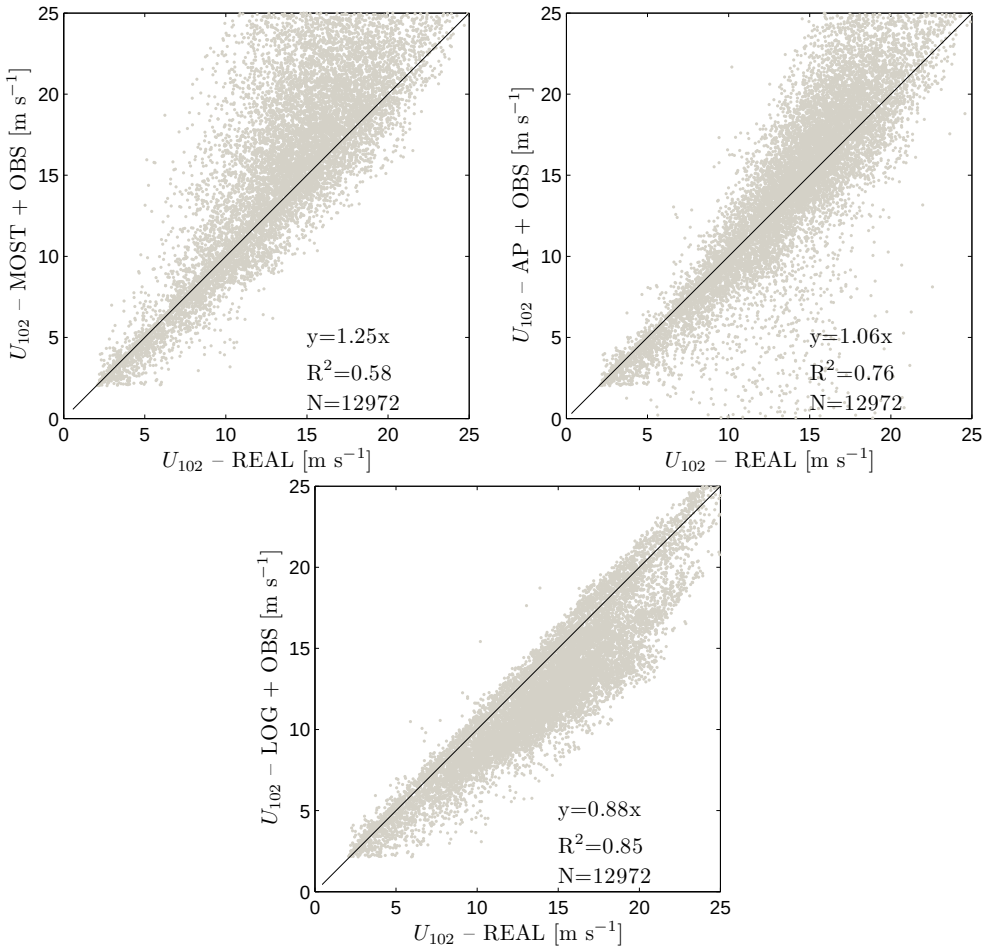

Figure 116: *As in Fig. 113 but for the Fino 2 met mast at 102 m AMSL*

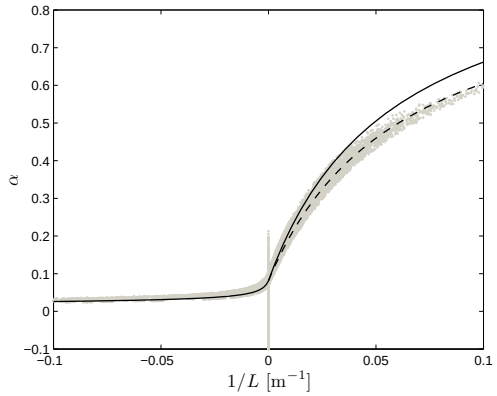

Figure 117: *Same as Fig. 93 but for the Egmond aan Zee met mast node at 45 m AMSL*

wind speed at the 70 and 116 m AMSL and the other three profiles, which show a similar behavior, agree very well with the observations, being the error the lowest for the LT AP profile, i.e. that accounting for the BLH.

For Egmond aan Zee, the means to derive stability come from using a bulk Richardson number, similarly to that for the M2 mast at Horns Rev I in Section 6. Here we estimate the stability corrections from the temperatures at 3 m BMSL and 21 m AMSL, wind speed at 21 AMSL, relative humidity at 21 m AMSL and pressure at 20 m AMSL. When comparing the extrapolated winds at 116 m using the three different methodologies as for Fino 1 (see Fig. 119), we found 1) a clear over-estimation of the wind speed under stable conditions by

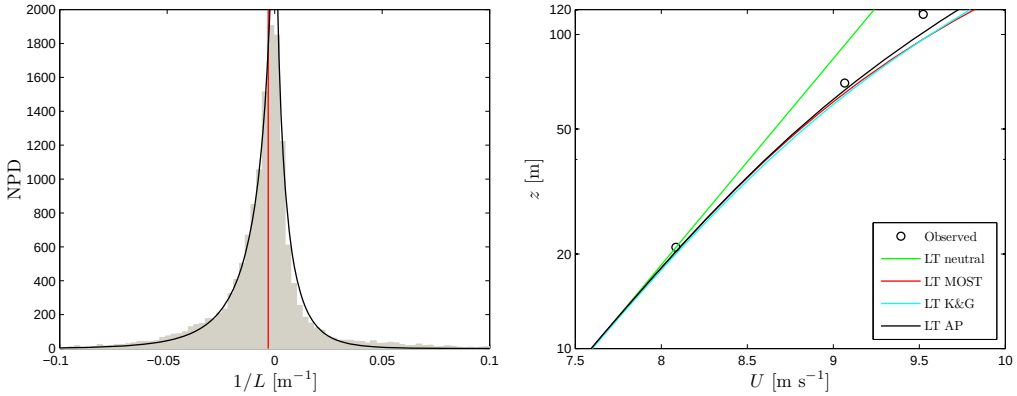

Figure 118: As Fig. 94, but for the WRF outputs and observations from the met mast at Egmond aan Zee

MOST (the high amount of scatter above the 1:1 line, 2) a clear correction for the BLH effect by the profiles in Peña et al. (2008) and 3) a general underestimation of the wind speed when assuming neutral atmospheric conditions. In this case, where we are more certain about the accuracy of the stability measures due to previous work with the Egmond aan Zee data (Sathe, 2009; Sathe et al., 2011), we find the highest correlations when using stability information and the profiles in Peña et al. (2008) than when assuming MOST with or without stability corrections. However, when using MOST, we find the lowest mean wind speed biases (1%). The highest biases as for Fino 1 are given by the neutral extrapolated profile.

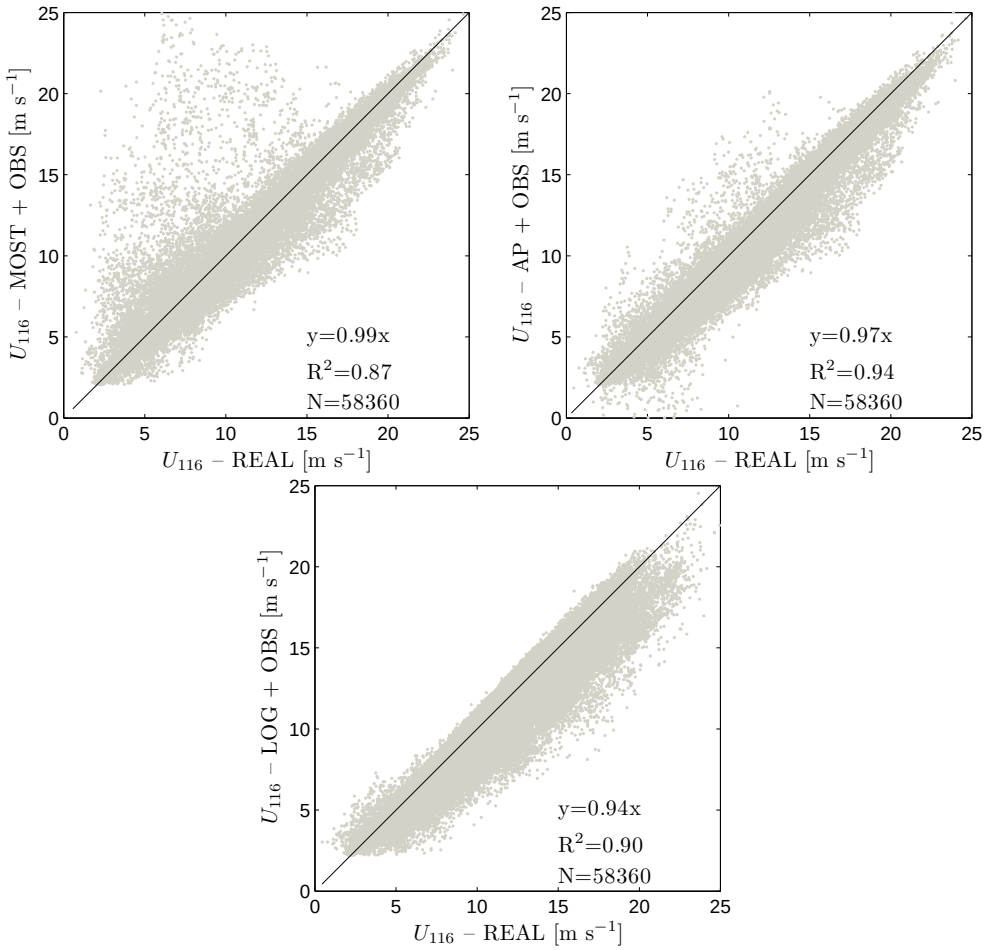

Figure 119: As in Fig. 113 but for the Egmond aan Zee met mast at 116 m AMSL

M7 – Horns Rev I

For this node, the heights used for the u_* and L derivations with the profile method are most of the times inside the surface layer (20 and 30 m AMSL). Figure 120 illustrates the behavior of α (estimated at 25 m AMSL from the observations) with atmospheric stability. As expected, α increases with stable atmospheric conditions. Similar 'artifacts', as those for the previous cases, are found in the plot, as well as low scatter. The theoretical lines predict the trend of the observations, agreeing well on the unstable side. For the stable side, α is over-predicted by MOST with atmospheric stability, as well as by using Eq. (16) with z_i as the mean of the WRF BLH outputs under stable conditions ($z_i = 392$ m).

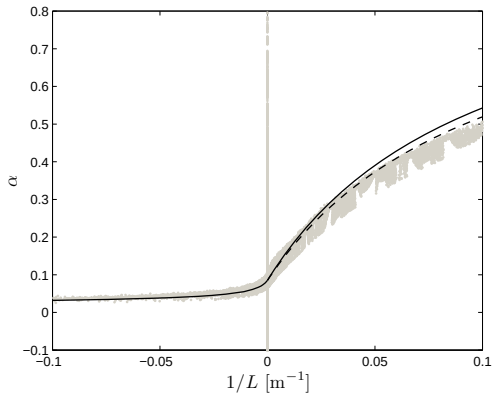

Figure 120: *Same as Fig. 93 but for the M7 met mast node at 25 m AMSL*

Figure 121 (left) shows the distribution of $1/L$ values from WRF at the M7 met mast. The theoretical distribution function for unstable and stable atmospheric conditions shows very good agreement with the histogram. The centroid of the distribution is found at -0.0027 m^{-1}, i.e. general predominance of unstable conditions. However, when estimating the long-term stability, a small correction to the stable side is found (at 70 m, $\langle \psi_m \rangle = -0.32$).

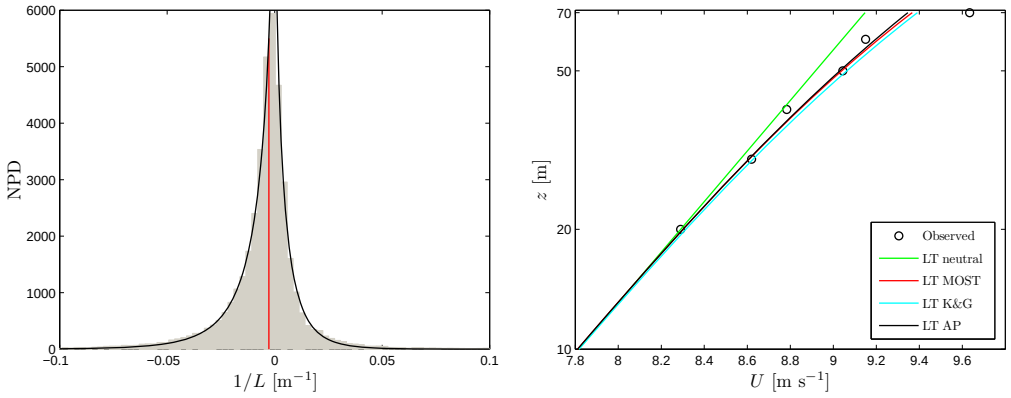

Figure 121: *As Fig. 94, but for the WRF outputs and observations from the met mast at M7*

Figure 121 (right) illustrates the long-term vertical wind speed profile observed at the M7 met mast. In this case, we also observe that the pole measurement shows a different behavior from that of the side-mounted anemometers, as shown above for the Fino 1 met mast. This is a well-known phenomenon observed at the three meteorological masts installed at the Horns Rev I wind farm and might be due to the combined effect of flow distortion due to the mast and booms on the side-mounted anemometers and a speed up effect at the pole measurement, since it is located close to the mast base (Peña et al., 2009). For the long-term vertical wind speed profile predictions, we also assume $L_m = 1000$ m as for the previous cases. $z_m = 502$ m from the mean of the concurrent WRF model outputs. $\langle u_* \rangle$ and z_o are then

estimated simultaneously using the observed long-term wind speed at the first level assuming $\langle\psi_m\rangle = 0$ ($\langle u_*\rangle = 0.27$ m s^{-1}). The mean WRF u_* gives a much higher value compared to this first-level fitted one ($u_* = 0.33$ m s^{-1}). The profile-derived mean u_* is just slightly higher ($u_* = 0.28$ m s^{-1}). For $\langle\psi_m\rangle$, we use the above WRF derived values. About the long-term predictions: The LT neutral profile slightly underestimates the wind speed compared to the side-mounted cup observations, and it strongly under-predicts the wind speed at 70 m AMSL. The other three profiles show a similar behavior, following closely the side-mounted cup observations and underestimating the wind speed at 70 m AMSL.

For M7, the means to derive stability also come from using a bulk Richardson number, similarly to that for the M2 mast at Horns Rev I in Section 6. Here we estimate the stability corrections from the temperatures at 3 m BMSL and 16 m AMSL, wind speed at 20 AMSL and pressure at 16 m AMSL. Relative humidity is assumed to be 78% at 20 m AMSL. When comparing the extrapolated winds at 70 m using the three different methodologies as for Fino 1 (see Fig. 122), we find similar features as the Egmond aan Zee case above 1) a clear over-estimation of the wind speed under stable conditions by MOST (the high amount of scatter above the 1:1 line in the low wind speed range), 2) a clear correction for the BLH effect by the profiles in Peña et al. (2008) and 3) a general underestimation of the wind speed when assuming neutral atmospheric conditions, although compared to the other two methods, it is only 1–2% higher. We also find the highest correlations when using stability information and the profiles in Peña et al. (2008) than when assuming MOST with or without stability corrections. The highest biases as for Fino 1 and Egmond aan Zee are given by the neutral extrapolated profile.

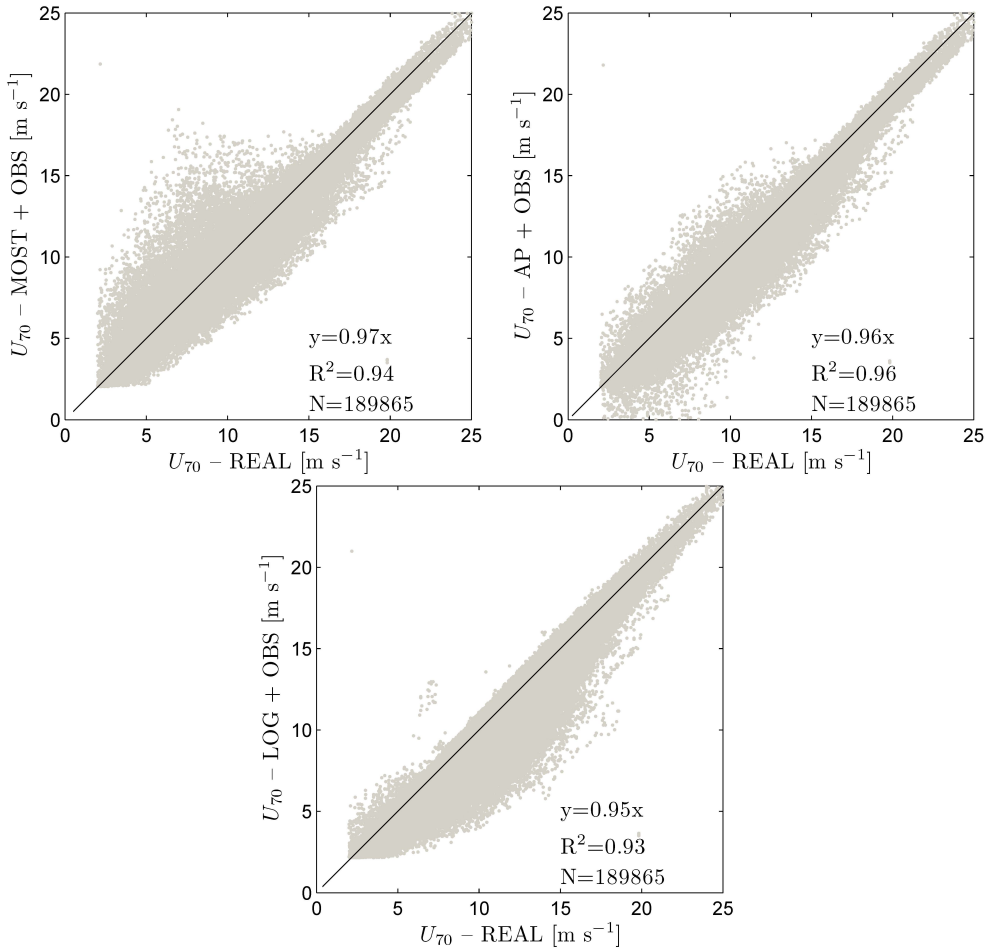

Figure 122: As in Fig. 113 but for the M7 met mast at 70 m AMSL

8 Inputs into satellite wind maps

This section relates to the techniques developed and used for the extrapolation of satellite winds to heights where offshore turbines operate. Such techniques are close-related to the analysis of the offshore vertical wind speed profile performed in Sections 4–7.

8.1 Introduction

Satellite winds normally refer to the wind speed estimated at 10-m height AMSL. This wind speed has been estimated by relating the radar backscatter signal from surface sea waves to the wind speed measured by anemometers placed on buoys. These empirical relations are known as geophysical model functions (GMFs) and their development and improvement have been matter of research during the last decades (Stoffelen and Anderson, 1997; Hersbach et al., 2007; Hersbach, 2010).

Two 10-m wind products can be retrieved by the GMFs: a 10-m true wind u_{10}, i.e. a wind speed 'comparable' to an in situ measurement, and a 10-m equivalent neutral wind (ENW) $u_{10\text{ENW}}$, which is the wind speed derived at 10-m AMSL by assuming neutral atmospheric stability conditions. There are no known formulations of GMFs capable of relating the radar backscatter signal to winds at heights higher than 10 m. Therefore, if one wants to estimate *instantaneous*[3] winds at different levels, one should use these 10-m winds to extract information about the wind profile. For example, using the wind profile in Eq. (5) for diagnosing u_{10}:

$$u_{10} = \frac{u_*}{\kappa}\left[\ln\left(\frac{10}{z_0}\right) - \psi_{m10}\right], \tag{29}$$

one can derive u_* for a set of given z_0 and ψ_{m10} values and then estimate winds at any level X as (e.g. using MOST):

$$u_X = \frac{u_*}{\kappa}\left[\ln\left(\frac{X}{z_0}\right) - \psi_{mX}\right]. \tag{30}$$

The question is how to estimate z_0, ψ_{m10} and ψ_{mX}. z_0 can be parameterized using Charnock's relation in Eq. (4) assuming a value for α_c, e.g. 0.0144 (Garratt, 1977; Sathe et al., 2011). ψ_{m10} and ψ_{mX} on the other hand are empirical relations that are dependent on L, i.e. the stability of the atmosphere (see Eq.s 7 and 8), which cannot be observed by satellites. For the ENW case, u_* is estimated in a simpler way since

$$u_{10\text{ENW}} = \frac{u_*}{\kappa}\ln\left(\frac{10}{z_0}\right). \tag{31}$$

However when estimating winds at any other level, we still need to use Eq. (30) and so ψ_{mX} is also required.

The observation of stability measures such as L is rarely performed in offshore conditions. In fact, the value of satellite winds is to provide information on those locations where in situ observations are normally not available, so it is difficult (not to say impossible) to obtain measurements of L to be used for the extrapolation of the 10-m satellite winds.

One alternative for the estimation of such stability measures is the use of a NWP model such as WRF. In Section 6, sonic, bulk and WRF turbulent fluxes, temperature, winds and stability measures were compared in an instantaneous basis and it was found a low correlation between WRF and sonic heat and momentum fluxes close to the surface and a much lower one for $1/L$ (R $=\sim 0.56$), although the mean biases are relatively low. However, on a long-term basis, distributions of $1/L$ from both WRF and observations are nearly identical and so the long-term atmospheric stability corrections (Figures 91 and 92). Therefore, in principle one should only extrapolate the long-term 10-m satellite winds to any other level by using NWP information on a long-term basis (as shown in Section 7.2 for the NORSEWInD wind lidar nodes); the errors in the extrapolation might be very high otherwise.

[3] By instantaneous we refer to 10-min, 30-min, 1-hour average winds

However, as shown above, from the 10-m satellite winds one can derive an u_* value almost 'directly', since the 10-m wind speed is used (not the WRF-u_* value), and the 'error' on this estimation only comes from the parameter ψ_{m10} when assuming MOST (and only when using u_{10}, not $u_{10\text{ENW}}$). This error is in principle small because the term ψ_m is low close to the surface. The largest errors are found when estimating winds at higher levels where ψ_m increases with height.

8.2 The Egmond aan Zee example

In order to get an idea of the error associated to the extrapolation of winds to high levels using either observations or WRF outputs for estimating stability measures, so that we can analyze the uncertainty in the methodology applied for lifting satellite winds to hub-height winds, we look at data from the Egmond aan Zee met mast. This mast is the only NORSEWInD node where this type of analysis can be performed because 1) Stability measures can be derived from both observations and from WRF model outputs, 2) The highest measurement level (116 m) is above the 80–100 m AMSL range of most turbines' hub height, 3) The first wind speed level (required to estimate u_*) is close to the surface (21 m AMSL) and 4) The wind speed observations do not need to be corrected for flow distortion and we can select the cup anemometer less affected by the mast-boom structure.

The 10-min data from this node are only filtered so that we avoid the effect of the wake of the wind farm on the observations. The 10-min data are used in case that there is a concurrent WRF output associated to it. The WRF model runs are exactly those presented in Section 6, but extracted for the Egmond aan Zee nearest grid point (instead of that close to the M2 location). The WRF outputs used for the analysis are:

1. Wind speed at the third model level, which is about 125 m AMSL
2. The surface layer friction velocity
3. The surface layer sensible heat flux
4. The surface layer temperature
5. The BLH

Items 2–4 are used to derive L from Eq. (6) and estimate the stability corrections ψ_m at 21 and 116 m AMSL from the model outputs. We also derive L and ψ_m from the observations using the bulk fluxes estimated as in Section 6.2.

Wind speed

In Figs. 123–129, we illustrate in scatter plots the comparisons between the observed 116-m wind speed (always in the x-axis) against different methods for extrapolation of the wind to the 116-m level or the direct WRF output (in the y-axis). All scatter plots have the same amount of data (N $= 10049$). For all comparisons, a linear regression through origin is performed (showing the mean wind speed bias) and the linear correlation coefficient (R^2) is also presented.

In Fig. 123 we compute the 116-m wind speed u_{116} by 1) estimating ψ_m at 21 and 116-m from the bulk observations 2) deriving u_* using MOST (Eq. 30) and Charnock's relation together with the previously computed ψ_{m21} value and the 21-m wind speed observation and 3) estimating u_{116} using MOST and Charnock's relation together with the previously computed ψ_{m116} and u_* values.

The mean wind speed bias is very low ($\sim -1\%$) and the correlation is high ($R^2 = 0.87$). Most of the outliers are located above the 1:1 line, i.e. the predicted value is higher than the observation. This is mainly because MOST is not longer valid in very stable conditions, where the term ψ_m becomes rather large over-predicting the correction of the wind speed due to atmospheric conditions, which results in rather large wind speeds. This is a known

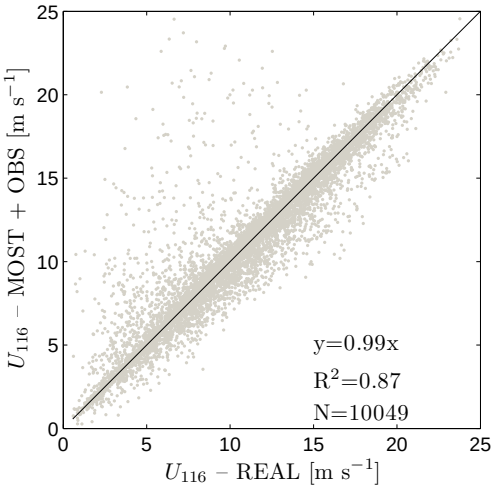

Figure 123: *Comparison of the 116-m wind speed observed at the Egmond aan Zee met mast against an estimated value (see related text for details)*

issue and the general approach is to filter the very stable conditions, which results in a higher correlation. However, a limit for such conditions is subjective and might leave too many data out of the analysis.

In Fig. 124, u_{116} is also estimated using MOST (Eq. 30), but with the direct output of u_* from WRF and the estimation of ψ_m at 116 m from the WRF outputs (so no observations are used at all). The scatter plot shows a quite large mean bias ($\sim 11\%$), which is mainly due to the general u_* over-prediction by the WRF model. The low correlation ($R^2 = 0.51$) is quite similar to that found for the velocity scales at the Horns Rev site in Section 6.4.

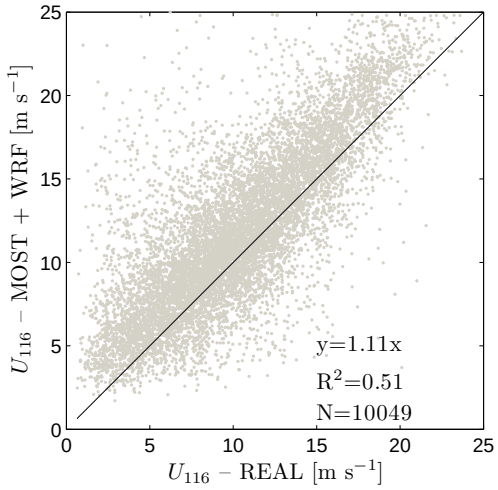

Figure 124: *As in Fig. 123*

In Fig. 125, u_{116} is estimated as in Fig. 124, but instead of using MOST we use the wind profiles from Peña et al. (2008) (Eq. 15) that correct the over-prediction of wind speed for stable conditions. The result is a slight reduction of the mean bias to $\sim 7\%$ (compared to the MOST case) and a high improvement in the correlation ($R^2 = 0.68$), which is evident from the much lower amount of outliers above the 1:1 line. This approach is one of those used by Kjeller Vindteknikk AS (KVT), our partner in the NORSEWInD project and in charge of the wind atlas, to extrapolate winds up to 100 m AMSL.

So far, the comparisons have been performed by using stability measures derived either from the WRF outputs or from observations. From WRF we are also able to extract the wind speed modeled at a level close to 116 m (the third level is ~ 125 m) and this is the one

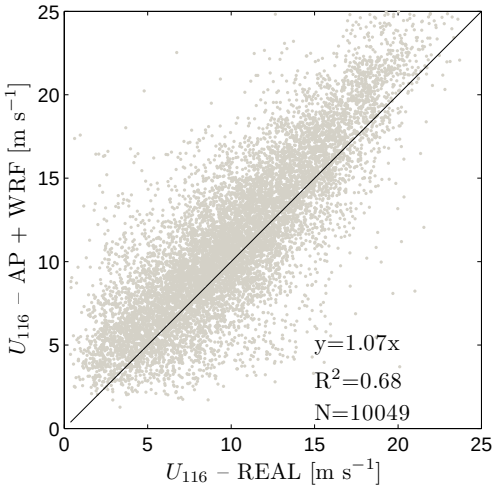

Figure 125: *As in Fig. 123*

we compared to the observation in Fig. 126. The mean bias is low ($\sim -3\%$) showing and under-prediction of winds by WRF at such levels, although the model height is higher than the observation. WRF wind speed under-prediction was also found at other NORSEWInD sites using different WRF configurations: at Fino 2 (Peña et al., 2011) and at Høvsøre (Floors et al., 2012). The correlation is lower than those shown in Peña et al. (2011) for different stations using a higher resolution WRF model setup and higher than that shown in Section 6.4 for M2 using the same WRF model setup.

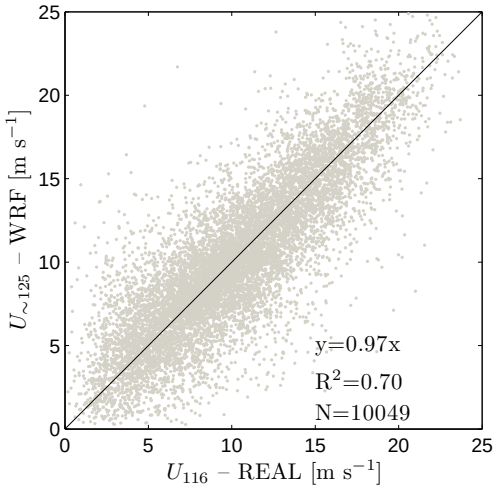

Figure 126: *As in Fig. 123*

However, we have not estimated u_{116} as we would like to when using satellite measurements yet, i.e. a combination of WRF outputs and the satellite observation. In this case we assume that the satellite measurement is equivalent to that wind speed observed at 21 m AMSL. The first 'satellite'-type estimation uses a procedure similar to that performed for Fig. 123, i.e. we 1) estimate ψ_m at 21 and 116-m from the WRF outputs 2) derive u_* using MOST (Eq. 30) and Charnock's relation together with the previously computed ψ_{m21} value and the 21-m wind speed observation and 3) estimate u_{116} using MOST and Charnock's relation together with the previously computed ψ_{m116} and u_* values.

As for the case shown in Fig. 123, the mean wind speed bias in Fig. 127 is very low ($\sim 0\%$) and the correlation is high ($R^2 = 0.80$). Most of the outliers are also located above the 1:1 line due to the high values of ψ_m for very stable corrections resulting in over-predicted wind speeds for such atmospheric conditions.

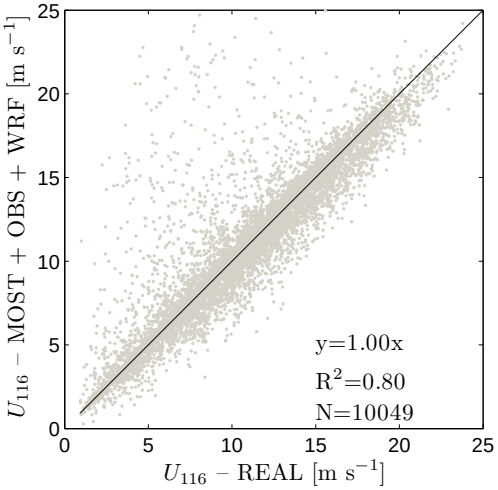

Figure 127: *As in Fig. 123*

The second 'satellite'-type estimation (shown in Fig. 128) is nearly identical to that used for Fig. 127, but instead of using MOST we use the wind profiles from Peña et al. (2008). Although the mean bias is not as good as the previous estimation ($\sim -4\%$), the correlation is the highest of all estimations ($R^2 = 0.93$), since most of the over-predicted wind speeds are corrected and to the fact that u_* is here estimated from an observation of the wind speed.

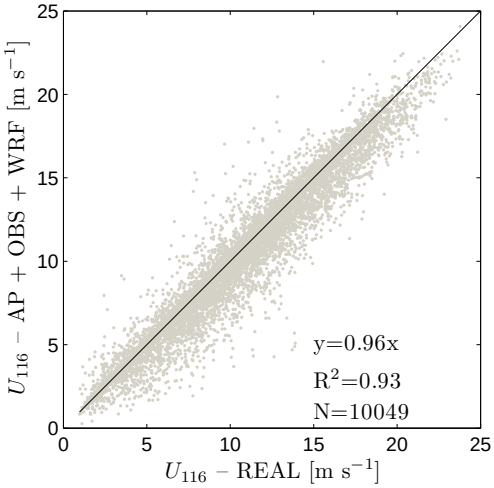

Figure 128: *As in Fig. 123*

A third and final 'satellite'-type estimation can be made by neglecting all atmospheric stability corrections, so u_* is estimated from u_{21} assuming $\psi_{m21} = 0$ using Eq. (30) and Charnock's relation and then, using the same equations, u_{116} is derived assuming $\psi_{m116} = 0$. The result is illustrated in Fig. 129. The mean bias is rather low ($\sim -6\%$) and the correlation the second highest of all estimations ($R^2 = 0.90$).

The statistics are rather interesting because one would expect that by neglecting the impact of stability the errors in the prediction of wind speeds will highly increase. However, for this data set, we can see that for most of the stable conditions, the estimated wind speed at 116 m is fairly well predicted by the neutral log wind profile. This does not have to do with the ability of the neutral log profile to predict winds at high levels, but with the problems of MOST for predicting winds at high levels far beyond the surface layer, where the theory is not longer valid and the corrections due to atmospheric conditions should not be applied–at least not under stable conditions.

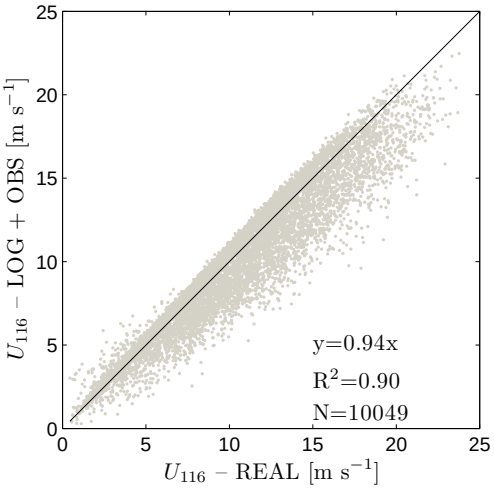

Figure 129: *As in Fig. 123*

Wind power density

Another type of comparison between the different methodologies for estimating u_{116} can be performed based on the power density value, which is more useful than the mean wind speed for wind resource assessment. The power density is here derived by treating all the u_{116} estimations and observations as time series–so we basically replace u_h by u_{116} in Eq. (1) and assume $\rho = 1.225$ kg m^{-3}. Table 2 illustrates the results for all the methodologies presented in Figs. 123–129.

Table 2: *Power density estimations in W m^{-2} based on observations and predictions of the wind speed at 116 m AMSL at Egmond aan Zee. The different methodologies used for the predictions are explained in the related text for Figs. 123–129*

Observation	Fig. 123	Fig. 124	Fig. 125	Fig. 126
REAL	MOST + OBS	MOST + WRF	AP + WRF	WRF
1053	1065	1779	1444	1088
	Fig. 127	Fig. 128	Fig. 129	
	MOST + OBS + WRF	AP + OBS + WRF	LOG + OBS	
	1126	974	900	

It is clear from the table that when using either MOST or the wind profiles from Peña et al. (2008) together with the u_* and ψ_m estimations from WRF, the power density is highly over-predicted compared to the observations. This is partly due to the positive mean wind speed bias for both types of methodologies, but also because the (high) scatter is distributed in both sides of the 1:1 line so the positive values have a larger effect on the power density than the negative ones (because we use the wind speed cubed). Using the wind speed at 21 m to estimate u_* with ψ_m estimations from WRF with either MOST or the profiles from Peña et al. (2008) gives slightly higher and lower values, respectively, compared to the observations. The difference with the direct WRF model output is even lower. The best estimation of power density is performed by using ψ_m and u_{21} observations to derive u_*. The highest power density under-predictions are found when neglecting all atmospheric stability effects. This is mainly due to the negative mean wind speed bias, which comes from the over-estimation of the wind speed by the neutral wind speed profile for unstable conditions.

Vertical wind shear

Wind speed and power density are not sufficient measures for the evaluation of the extrapolation methodologies because one can accurately predict wind speed and power at a given height without knowing the shape of the vertical wind speed profile. This can lead to large errors in the wind speed prediction for the levels below and above the predicted height. Further, it is also important to accurately predict the vertical wind shear in the layer where the wind turbines operate for performance, loading and safety purposes. Therefore, we evaluate all methodologies mentioned above in terms of the vertical wind shear: for all results from the WRF model, the observations and the different predictions, we estimate the α value between the levels 70 and 116 m AMSL from Eq. (9).

Figure 130 illustrates the result of the α analysis in terms of distribution. This is preferred, since the mean and median α values might be close for the different methodologies compared to the observations, although the number of high and low shear conditions might be totally different.

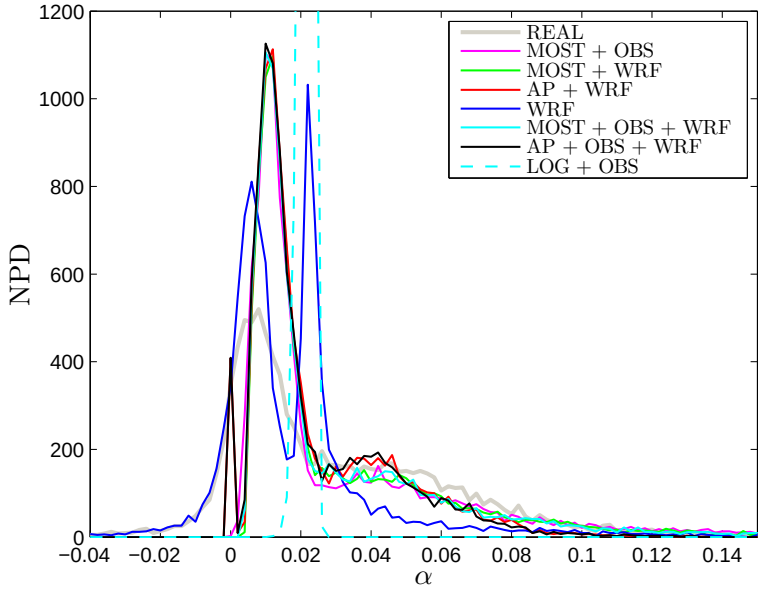

Figure 130: Distribution of the vertical wind shear between the levels 70 and 116 m AMSL based on observations and predictions of the wind speed. The different methodologies used for the predictions are explained in the related text for Figs. 123–129

As illustrated, the observed α value (REAL) is distributed between negative and positive values with a long tail within the positive side and a peak at ~ 0.008. It is important to mention that the theoretical value (according to surface-layer theory for neutral conditions) is 0.0768. None of the different methodologies is able to predict the negative values observed from the observations. Only the WRF model (WRF) follows closely the negative side of the distribution, but it shows to peaks; one around 0.006 and the other at 0.022. These two peaks might come from the characteristics of the vertical wind shear for unstable and neutral atmospheric conditions derived by the YSU PBL scheme of the WRF model. The amount of high wind shear situations is clearly under-predicted by the model. By neglecting all atmospheric stability effects (LOG + OBS), we produce a rather narrow distribution (peaking at 0.022) being the most different compared the observed one. The other five methodologies, using MOST or the profiles from Peña et al. (2008) and estimating ψ_m and u_* either from WRF or from the observations, show similar distributions; they are all close to the observed one for high wind shear values (above 0.02), but they all peak at ∼0.010. These five methods start to under-predict the amount of low wind shear values at ∼0.005 and those methods using the profiles of Peña et al. (2008) show a second peak at 0. This is because these profiles

are only valid up to the BLH, so we assume that the wind speed is constant with height above the BLH; the peak actually shows the amount of situations where the BLH is lower than 70 m AMSL.

9 Conclusions

An extensive analysis of the observations performed by wind lidars and met masts at a number of offshore sites within the framework of the NORSEWInD project has been performed. The analysis has been based on measurements of the vertical wind shear and wind speed profile within the heights were large wind turbines operate, i.e. between 10 m up to 300 m AMSL. The major findings are:

- Wind lidars provide valuable information of the vertical wind shear within a wide geographical area and range of vertical levels in the atmosphere that it is nearly impossible to obtain with the current met mast network in the North Sea. Until now wind lidars had been mostly used to complement met campaigns, but in most of the NORSEWInD cases, they are proven to successfully replace the met masts, showing a high degree of portability and reliability, and avoiding mast and boom distortion related effects.
- Information on the vertical wind speed profile, within the vertical area close to that where wind turbines operate, is important to better predict the power output from the turbine. By measuring the wind speed at hub height only, information about the energy flux is missed and thus the power outputs become more uncertain.
- The commonly adopted offshore vertical wind shear value, $\alpha = 0.2$, is valid for a very narrow set of atmospheric and marine conditions. α varies in the marine SBL with atmospheric stability, roughness (as the sea roughness is not constant and increases with wind speed) and height. Above the surface layer, other effects, such as the BLH and baroclinicity, become more important. For the same height and roughness, α is higher during stable than unstable conditions.
- For the analysis of the long-term vertical wind speed profile, we require information about the long-term stability condition, which can only be identified by analyzing the long-term distribution of the short-term stability measures. These include the turbulent fluxes (heat and momentum) and temperature.
- In offshore conditions the observed α values at 100 m AMSL are often within the range -0.2–0.8 with a peak within the range 0–0.125. Negative values are found both under unstable and stable atmospheric conditions. The centroid of the distribution of these α values is generally found to be close to that value estimated from the neutral log wind profile assuming neutral conditions and $z_o = 0.0002$ m. In onshore conditions α increases, mainly due to the higher roughness length.
- α is found to be nearly constant during the diurnal cycle, because of the slight diurnal variation of the sea temperature (contrary to an onshore site, where the surface temperature increases during daytime). On a monthly basis, α is generally found to be highest and lowest during the spring and autumn months, respectively. This is due to the seasonality of the sea temperature, which during spring is still cold from the winter, while the air is warming up, thus giving rise to stable conditions; during autumn the sea is still warm, while the air starts to cool down, thus giving rise to unstable conditions.
- No clear indication of α dependency on distance to the coast is found. Most of the NORSEWInD nodes exhibit an increasing α for increasing wind speeds, since the sea roughness increases with wind speed. Furthermore, for most nodes the behavior of α with wind speed is well predicted by using the neutral wind speed profile and Charnock's relation within the range 5–10 m s^{-1} and under-predicted for higher wind speeds. When analyzing the seasonality of α, it is generally found that the predicted α values assuming neutral conditions are below the observed values, indicating a general stable correction to the vertical wind shear over the North Sea. Classifying observations of α into unstable and stable atmospheric conditions (based on observed stability measures), we clearly find a higher α value for stable than for unstable conditions, as expected.

- From a sonic-WRF-bulk comparison of 10-min observations and model results at mast 2 (Horns Rev I) we find high correlations and statistics for the velocity scales (wind speed and friction velocity) and temperatures, and low correlations for the heat flux and Obukhov length, although the mean biases are not high. The scatter is always higher when the comparison is performed against the WRF model outputs. We found, on a long-term basis, a nearly identical stability correction to the long-term vertical wind speed profile when computed from the bulk estimations and the WRF outputs; the profile needs to be corrected to the stable side. We also show that in general small long-term stable corrections need to be performed for a large area in the North Sea.
- By analyzing most of the NORSEWInD nodes' observations of α and the derived stability measures, it is shown that MOST predicts well the behavior of α under unstable atmospheric conditions but tends to over-predict it under stable conditions. Such over-prediction is avoided when the BLH is taken into account. The long-term stability distributions fit well the histogram of stability measures based on WRF outputs at all nodes, although a good number of them does not exceed 1-year of available data. The long-term vertical wind speed profile derived from WRF is difficult to compare to the observations, because u_* is not available from observations and is generally over-predicted by WRF. However, in the cases that the data are long enough and that the long-term neutral wind speed profile is fitted to a measurement well inside the surface layer, the long-term predicted profiles agree well with the observations.
- When extrapolating winds using profile formulations that take into account the influence of both stability and BLH, we find the highest correlations compared to the observation, only in the cases where the stability measures are accurate and the low-level measurement is not distorted. By using stability information only, we find the lowest correlations and general lower mean wind speed biases.
- When using short-term estimates of u_* and stability from the WRF model, we found that the predicted wind speed at a hub-height level is highly uncertain and has a large mean bias compared to the hub-height wind speed observation when MOST is applied to the extrapolation. The mean bias decreases and the correlation increases when the BLH is taken into account and the results are similar than the WRF output. When using stability information from the WRF model, but deriving u_* from a low-level wind speed (as an analogy of the satellite case where winds at 10-m are retrieved), the statistics for the predicted hub-height wind become better than the above mentioned and similar to those found when the stability information comes from observations, both types of predicitions assuming MOST. When incorporating the BLH, the highest correlations are found, which is mainly because MOST strongly over-predicts the wind speed at levels beyond the surface layer.

Acknowledgments

This work and its results were only possible thanks to the support and funding from the EU through the project "NORSEWInD" contract TREN-FP7EN-219048. We would like also to acknowledge the fruitful discussions and the data shared with our project partners at Kjeller Vindteknikk AS, particularly Erik Berge and Rolv E. Bredesen. Wind lidar and Fino 3 data were kindly provided by Detlev Kindler from GL Garrad Hassan.

10 Publication list

The following are a number of publications within the framework of NORSEWInD's work task 3.1:

- Alfredo Peña, Sven-Erik Gryning and Charlotte B. Hasager (2010) Length scales of the neutral wind profile over homogeneous terrain. *Journal of Applied Meteorology and Climatology* **49**:792–806
- Alfredo Peña, Sven-Erik Gryning and Jakob Mann (2010) On the length-scale of the wind profile. *Quarterly Journal of the Royal Meteorological Society* **136**:2119–2131
- Merete Badger, Jake Badger, Morten Nielsen, Charlotte B. Hasager and Alfredo Peña (2010) Wind class sampling of satellite SAR imagery for offshore wind resource mapping. *Journal of Applied Meteorology and Climatology* **49**:2474–2491
- Andrea Hahmann and Alfredo Peña (2010) Validation of boundary-layer winds from WRF mesoscale forecasts over Denmark. *Proceedings of the European Wind Energy Association Conference & Exhibition*, Warsaw, Oral presentation
- Caroline Draxl, Andrea N. Hahmann, Alfredo Peña, Jesper N. Nissen and Gregor Giebel (2010) Validation of boundary-layer winds from WRF Mesoscale Forecasts with applications to wind energy forecasting. *Proceedings of the 19th Symposium on Boundary Layers and Turbulence*, Oral presentation
- Alfredo Peña, Sven-Erik Gryning and Jakob Mann (2010) The length-scale of the diabatic wind profile. *Proceedings of the Science of Making Torque from Wind Conference*, Heraklion, Oral presentation
- Andrea N. Hahmann, Caroline Draxl, Alfredo Peña and Joakim R. Nielsen (2011) Simulating the vertical structure of the wind with the weather research and forecasting (WRF) model. *Proceedings of the European Wind Energy Association Conference & Exhibition*, Brussels, Poster presentation
- Charlotte B. Hasager, Merete Badger, Alfredo Peña, Xiaoli G. Larsén and Ferhat Bingöl (2011) SAR-based wind resource stadistics in the Baltic Sea. *Remote Sensing* **3**:117–144
- Ameya Sathe, Sven-Erik Gryning and Alfredo Peña (2011) Comparison of the atmospheric stability and wind profiles at two wind farm sites over a long marine fetch in the North Sea. *Wind Energy* **14**:767–780
- Andrea N. Hahmann, Caroline Draxl, Alfredo Peña and Joakim R. Nielsen (2011) Simulating the vertical structure of the wind with the WRF model. *12th Annual WRF Users' Workshop*, Boulder, Oral presentation
- Rogier Floors, Sven-Erik Gryning, Alfredo Peña and Ekaterina Batchvarova (2011) Analysis of diabatic flow modification in the internal boundary layer. *Meteorologische Zeitschrift* **20**:649–659
- Alfredo Peña, Sven-Erik Gryning, Torben Mikkelsen, Charlotte Hasager and Mark Kelly (2011) Long-term vertical wind shear observed by wind lidars at several locations on the North Sea. *Proceedings of the European Offshore Wind Energy Association Conference & Exhibition*, Amsterdam, Poster presentation
- Merete Badger, Jake Badger, Charlotte Hasager, Morten Nielsen, Alfredo Peña and Alexis Mouche (2011) Wind resource mapping over the North Sea using satellite SAR. *Proceedings of the European Offshore Wind Energy Association Conference & Exhibition*, Amsterdam, Poster presentation

- Ioanna Karagali, Alfredo Peña, Merete Badger, Andrea Hahmann and Charlote Hasager (2011) QuikSCAT for wind energy resource assessment. *Proceedings of the American Geophysical Union Fall Meeting*, San Francisco, Oral presentation
- Alfredo Peña and Andrea N. Hahmann (2012) Atmospheric stability and turbulent fluxes at Horns Rev–an intercomparison of sonic, bulk and WRF model data. *Wind Energy* **15**:717–731
- Ioanna Karagali, Alfredo Peña, Merete Badger, and Charlotte B. Hasager (2012) Wind characteristics in the North and Baltic Seas from the QuickSCAT satellite. *Wind Energy*, in review
- Ioanna Karagali, Merete Badger, Andrea N. Hahmann, Alfredo Peña, Charlotte B. Hasager and Anna Maria Sempreviva (2012) Spatial and temporal variability of winds in the Northern European Seas. *Renewable Energy*, in review
- Alfredo Peña, Sven-Erik Gryning, Torben Mikkelsen, Charlotte Hasager and Mark Kelly (2012) The modeling and observation of the long-term offshore wind profile and wind shear. *Proceedings of the European Wind Energy Association Conference & Exhibition*, Copenhagen, Oral presentation
- Merete Badger, Alfredo Peña, Rolv Erlend Bredesen, Erik Berge, Andrea Hahmann, Jake Badger, Ioanna Karagali, Charlotte Hasager and Torben Mikkelsen (2012) Bringing satellite winds to hub height. *Proceedings of the European Wind Energy Association Conference & Exhibition*, Copenhagen, Oral presentation
- Caroline Draxl, Andrea N. Hahmann, Alfredo Peña and Gregor Giebel (2012) Evaluating winds and vertical wind shear from WRF model forecasts using seven PBL schemes. *Wind Energy*, in press
- Alfredo Peña and Sven-Erik Gryning (2012) The challenging offshore wind conditions. *Proceedings of the International Conference on Research at Alpha Ventus*, Bremerhaven, Invited oral presentation
- Ioanna Karagali (2012) Offshore wind energy: wind and sea surface temperature from satellite observations. PhD Thesis, DTU Wind Energy, Roskilde
- Merete Badger, Alfredo Peña, Ad Stoffelen, Tilly Driesenaar, Erik Berge and Rolv Erlend (2012) Bringing ocean winds from 10 m to higher levels. *Proceedings of the International Geoscience and Remote Sensing Symposium*, Munich, Oral presentation
- Alfredo Peña, Torben Mikkelsen, Sven-Erik Gryning, Charlotte B. Hasager, Andrea N. Hahmann, Merete Badger, Ioanna Karagali and Michael S. Courtney (2012) Offshore vertical wind shear. Technical Report. DTU Wind Energy-E-Report-0005 (EN), DTU Wind Energy, Roskilde

References

Badger, M., J. Badger, M. Nielsen, C. B. Hasager, and A. Peña, 2010: Wind class sampling of satellite SAR imagery for offshore wind resource mapping. *J. Applied Meteorol. Climatol.*, **49**, 2474–2491.

Barthelmie, R. and L. E. Jensen, 2010: Evaluation of wind farm efficiency and wind turbine wakes at the Nysted offshore wind farm. *Wind Energy*, **13**, 573–586.

Byrkjedal, Ø. and E. Berge, 2008: The use of WRF for wind resource mapping in Norway. *9th Annual WRF User's Workshop*, Boulder.

Carlsson, B., A. Rutgersson, and A.-S. Smedman, 2009: Investigating the effect of a wave-dependent momentum flux in a process oriented ocean model. *Boreal. Env. Res.*, **14**, 3–17.

Charnock, H., 1955: Wind stress over a water surface. *Quart. J. Roy. Meteorol. Soc.*, **81**, 639–640.

Chen, F. and J. Dudhia, 2001: Coupling an advanced land-surface/hydrology model with the penn state/NCAR MM5 modeling system. Part I: Model description and implementation. *Mon. Wea. Rev.*, **129**, 569–585.

Courtney, M., R. Wagner, and P. Lindelöw, 2008: Testing and comparison of lidars for profile and turbulence measurements in wind energy. *Earth Environ. Sci.: Conf. Ser.*, **1**, 012 021 (14 pp).

Cutler, N. J., J. D. Kepert, H. R. Outhred, and I. F. MacGill, 2008: Characterizing wind power forecast uncertainty with numerical weather predicition spatial fields. *Wind Engineering*, **32**, 509–524.

Dudhia, J., 1989: : Numerical study of convection observed during the winter monsoon experiment using a mesoscale two-dimensional model. *J. Atmos. Sci.*, **46**, 3077–3107.

Floors, R., S.-E. Gryning, A. Peña, and E. Batchvarova, 2011: Analysis of diabatic flow modification in the internal boundary layer. *Meteorol. Z.*, **20**, 649–659.

Floors, R., C. L. Vincent, S.-E. Gryning, E. Batchvarova, and A. Peña, 2012: Wind profile in the coastal boundary layer: wind lidar measurements and wrf modelling. *Bound.-Layer Meteorol.*, in review.

Friehe, C. A., 1977: Estimation of the refractive-index structure parameter in the atmospheric boundary layer over the ocean. *Appl. Opt.*, **16**, 334–340.

Garratt, J. R., 1977: Review of drag coefficients over oceans and continents. *Mon. Wea. Rev.*, **105**, 915–929.

Grachev, A. A. and C. W. Fairall, 1996: Dependence of the Monin-Obukhov stability parameter on the bulk Richardson number over the ocean. *J. of Applied Meteorol.*, **36**, 406–414.

Gryning, S.-E., E. Batchvarova, B. Brümmer, H. Jørgensen, and S. Larsen, 2007a: On the extension of the wind profile over homogeneous terrain beyond the surface layer. *Boundary-Layer Meteorol.*, **124**, 251–268.

Gryning, S.-E., H. Jørgensen, S. Larsen, and E. Batchvarova, 2007b: The wind profile up to 300 meters over flat terrain. *J. Phys.: Conf. Ser.*, **75**, 012 066 (9 pp).

Hagemann, S., D. Callies, and B. Lange, 2009a: Deliverable 1.14: Description of met masts, instrumentation and historical data used in the project. Tech. Rep. EU Project number: 219048, Institut für Solare Energieversorgungstechnik e. V. (ISET), 36 pp.

Hagemann, S., D. Callies, and B. Lange, 2009b: Deliverable 1.15: First version of data processing procedures. Tech. Rep. EU Project number: 219048, Institut für Solare Energieversorgungstechnik e. V. (ISET), 15 pp.

Hahmann, A. N. and A. Peña, 2010: Validation of boundary-layer winds from WRF mesoscale forecasts over Denmark. *Proceedings of the European Wind Energy Association Conference & Exhibition*, Warsaw.

Hahmann, A. N., D. Rostkier-Edelstein, T. T. Warner, F. Vandenberghe, Y. Liu, R. Babarsky, and S. P. Swerdlin, 2010: A reanalysis system for the generation of mesoscale climatographies. *J. Applied Meteorol. Climatol.*, **49**, 954–972.

Hasager, C. B., A. Peña, M. B. Christiansen, P. Astrup, M. Nielsen, M. Nonaldo, F. Thompson, and P. Nielsen, 2008: Remote sensing observation used in offshore wind energy. *IEEE J. Selected Topics Appl. Earth Obs. Rem. Sens.*, **1**, 67–69.

Hersbach, H., 2010: Comparisons of c-band scatterometer CMOD5.N equivalent neutral winds with ECMWF. *J. Atmos. Ocean. Techn.*, **27**, 721–736.

Hersbach, H., A. Stoffelen, and S. de Haan, 2007: An improved c-band scatterometer ocean geophysical model function: CMOD5. *J. Geophys. Res.*, **112**, C3006 476–793.

Hong, S.-Y., Y. Noh, and J. Dudhia, 2006: A new vertical diffusion package with an explicit treatment of entrainment processes. *Mon. Wea. Rev.*, **134**, 2318–2341.

Hu, X.-M., J. W. Nielsen-Gammon, and F. Zhang, 2010: Evaluation of three planetary boundary layer schemes in the WRF model. *J. Appl. Meteorol. Climatol.*, **49**, 1831–1844.

IEC, 2005: *61400-1 Wind turbine generator systems – Part 1:Safety requirements*. Int. Electrotechnical Commission.

Jensen, L. E., 2007: Array efficiency at Horns Rev and the effect of atmospheric stability. *Proceedings of the European Wind Energy Association Conference & Exhibition*, Milano.

Jørgensen, H. E., T. Mikkelsen, S.-E. Gryning, S. Larsen, P. Astrup, and P. E. Sørensen, 2008: Measurements from Høvsøre met mast. Tech. Rep. Risoe-R-1592(EN), Risø National Laboratory, Roskilde, URL:www.risoe.dk.

Kaimal, J. C. and J. E. Gaynor, 1991: Another look at sonic thermometry. *Boundary-Layer Meteorol.*, **56**, 401–410.

Kain, J. S. and J. M. Fritsch, 1990: A one-dimensional entraining/detraining plume model and its application in convective parameterization. *J. Atmos. Sci.*, **47**, 2784–2802.

Kanamitsu, M., W. Ebisuzaki, J. Woollen, S. K. Yang, J. J. Hnilo, and M. Fiorino, 2002: NCEP-DOE AMIP-II Reanalysis (R-2). *Bull. Am. Meteorol. Soc.*, **83**, 1631–1643.

Kelly, M. and S.-E. Gryning, 2010: Long-term wind profiles based on similarity theory. *Boundary-Layer Meteorol.*, **136**, 377–390.

Kindler, D., 2010a: Lidar installation report - windcube wc 026. Tech. rep., Windtest K.-W.-Koog GmbH, 5 pp.

Kindler, D., 2010b: Lidar installation report - windcube wc 037. Tech. rep., Windtest K.-W.-Koog GmbH, 4 pp.

Kindler, D., 2010c: Lidar installation report - windcube wc 044. Tech. rep., Windtest K.-W.-Koog GmbH, 6 pp.

Kindler, D., 2010d: Lidar installation report - windcube wc 058. Tech. rep., Windtest K.-W.-Koog GmbH, 9 pp.

Lange, B., S. Larsen, J. Højstrup, and R. Barthelmie, 2004: Importance of thermal effects and the sea surface roughness for offshore wind resource assessment. *J. Wind Eng. Ind. Aerodyn.*, **92**, 959–988.

Liu, H., G. Peters, and T. Foken, 2001: New equations for sonic temperature variance and buoyancy heat flux with an omnidirectional sonic anemometer. *Bound.-Layer Meteor.*, **100**, 459–468.

Lu, H. and F. Porté-Agel, 2011: Large-eddy simulation of a very large wind farm in a stable atmospheric boundary layer. *Phys. Fluids*, **23**, 065 101 (1–19).

Mann, J., S. Ott, B. Jørgensen, and H. Frank, 2002: WAsP Engineering 2.0. Tech. Rep. Risoe-R-1356(EN), Risø National Laboratory, Roskilde, Denmark, *http://www.risoe.dk/rispubl/VEA/ris-r-1356.htm*.

Mlawer, E. J., S. J. Taubman, P. D. Brown, M. J. Iacono, and S. A. Clough, 1997: Radiative transfer for inhomogeneous atmosphere: RRTM, a validated correlated-k model for the long-wave. *J. Geophys. Res.*, **102(D14)**, 16 663–16 682.

Monin, A. S. and A. M. Obukhov, 1954: Osnovnye zakonomernosti turbulentnogo peremeshivanija v prizemnom sloe atmosfery (Basic laws of turbulent mixing in the atmosphere near the ground). *Trudy Geofiz. Inst. AN SSSR*, **24 (151)**, 163–187.

Mortensen, N. G., D. N. Heathfield, L. Myllerup, L. Landberg, and O. Rathmann, 2007: Getting started with WAsP 9. Tech. Rep. Risø-I-2571(EN), Risø National Laboratory, Roskilde, Denmark, *http:/www.wasp.dk/Download/DownloadFiles/General/Getting Started with WAsP 9.pdf*.

Oost, W. A., C. M. J. Jacobs, and C. van Oort, 2000: Stability effects on heat and moisture fluxes at sea. *Bound.Layer Meteorol.*, **95**, 271–302.

Peña, A., 2009: Sensing the wind profile. Tech. Rep. Risoe-PhD-45(EN), Risø DTU, 80 pp.

Peña, A. and S.-E. Gryning, 2008: Charnock's roughness length model and non-dimensional wind profiles over the sea. *Boundary-Layer Meteorol.*, **128**, 191–203.

Peña, A., S.-E. Gryning, and C. B. Hasager, 2008: Measurements and modelling of the wind speed profile in the marine atmospheric boundary layer. *Boundary-Layer Meteorol.*, **129**, 479–495.

Peña, A., S.-E. Gryning, and C. B. Hasager, 2010a: Comparing mixing-length models of the diabatic wind profile over homogeneous terrain. *Theor. Appl. Climatol.*, **100**, 325–335.

Peña, A., S.-E. Gryning, and J. Mann, 2010b: On the length-scale of the wind profile. *Q. J. Royal Meteorol. Soc.*, **136**, 2119–2131.

Peña, A., A. Hahmann, C. B. Hasager, F. Bingöl, I. Karagali, J. Badger, M. Badger, and N.-E. Clausen, 2011: South baltic wind atlas. Tech. Rep. Risoe-R-1775(EN), Risø National Laboratory for Sustainable Energy, Technical University of Denmark, 66 pp.

Peña, A. and A. N. Hahmann, 2012: Atmospheric stability and turbulent fluxes at Horns Rev–an intercomparison of sonic, bulk and WRF model data. *Wind Energy*, **15**, 717–731.

Peña, A., C. B. Hasager, S.-E. Gryning, M. Courtney, I. Antoniou, and T. Mikkelsen, 2009: Offshore wind profiling using light detection and ranging measurements. *Wind Energy*, **12**, 105–124.

Peña, A., S.-E-Gryning, and A. N. Hahmann, 2012: Observations of the coastal atmospheric boundary-layer height in western denmark. *J. Geophys. Res.*, in review.

Rutgersson, A., A.-S. Smedman, and A. Omstedt, 2001: Measured and simulated latent and sensible heat fluxes at two marine sites in the Baltic Sea. *Bound.Layer Meteorol.*, **99**, 53–84.

Sathe, A., 2009: Project site data – OWEZ data analyzis. Tech. Rep. We@Sea project 2004-012, TU Delft, 54 pp.

Sathe, A., S.-E. Gryning, and A. Peña, 2011: Comparison of the atmospheric stability and wind profiles at two wind farm sites over a long marine fetch in the North Sea. *Wind Energy*, **14**, 767–780.

Sempreviva, A. M., S. E. Larsen, N. G. Mortensen, and I. Troen, 1990: Response of neutral boundary layers to changes of roughness. *Boundary-Layer Meteorol.*, **50**, 205–225.

Skamarock, W. C., et al., 2008: A description of the advanced research WRF version 3. Tech. Rep. NCAR/TN-475+STR, Mesoscale and Microscale Meteorology Division, National Center for Atmospheric Research, Boulder, Colorado, USA, 113 pp.

Smith, S. D., 1980: Coefficients of sea surface wind stress, heat flux, and wind profiles as function of wind speed and temperature. *J. Geophys. Res.*, **93**, 467–472.

Stickland, M. T., S. Fabre, and T. Scanlon, 2010: Norsewind data report and correction data for horns rev 2. Tech. rep., University of Strahclyde, 50 pp.

Stoffelen, A. and D. Anderson, 1997: Scatterometer data interpretation: estimation and validation of the transfer function CMOD4. *J. Geophys. Res.*, **102**, C3 5767–5780.

Storm, B., J. Dudhia, S. Basu, A. Swif, and I. Giammanco, 2009: Evaluation of the weather research and forecasting model on forecasting low-level jets: implications for wind energy. *Wind Energy*, **12**, 81–90.

Sušelj, K. and A. Sood, 2010: Improving the Mellor-Yamada-Janjić parameterization for wind conditions in the marine planetary boundary layer. *Bound.-Layer Meteorol.*, **136**, 301–324.

Thompson, G., R. M. Rasmussen, and K. Manning, 2004: Explicit forecasts of winter precipitation using an improved bulk microphysics scheme. Part I: Description and sensitivity analysis. *Mon. Wea. Rev.*, **132**, 519–542.

Vincent, C. L., P. Pinson, and G. Giebel, 2011: Wind fluctuations over the North Sea. *Int. J. Climatol.*, **31**, 1584–1595.

Wagner, R., M. Courtney, J. Gottschall, and P. Lindelöw-Marsden, 2011: Accounting of the speed shear in wind turbine power performance measurement. *Wind Energy*, **14**, 993–1004.

Wang, W., et al., 2009: *WRF-ARW Version 3 Modeling System User's Guide*. Mesoscale & Microscale Meteorology Division, National Center for Atmospheric Research, Boulder, USA.

Zilitinkevich, S. S. and I. N. Esau, 2005: Resistance and heat-transfer laws for stable and neutral planetary boundary layers: old theory advanced and re-evaluated. *Quart. J. Roy. Meteor. Soc.*, **131**, 1863–1892.

Appendix A: Wind lidar – Cloud and fog interference

In this WT, we have also been (accidentally) involved in the analysis of the effects of fog and clouds on the wind lidars. This analysis took place during the testing, calibration and verification period of the wind lidars at the Høvsøre test station prior to deployment to the NORSEWInD wind lidar nodes.

The analysis of these effects started when comparing the wind lidar and the mast cup anemometer wind speeds. Figure 131 illustrates the wind speed comparison for one of the ZephIR units with the cup anemometers at 100 and 116.5 m.

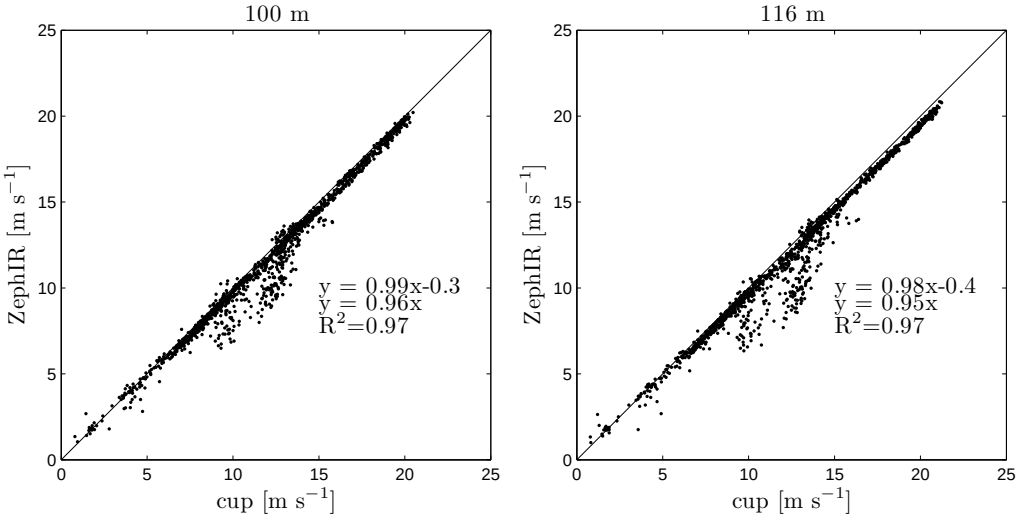

Figure 131: Wind speed comparison between a ZephIR wind lidar and the cup anemometers at Høvsøre at 100 m (left) and 116.5 m (right)

As shown in the figure, the wind lidar wind speed is nearly the same as the cup anemometer one, except that there is a number of outliers, specially in the middle range of wind speeds where the wind lidar wind speed is lower than the cup one (negative outliers). This type of behavior has been previously observed from measurements at Høvsøre but the amount of outliers were much less. What is commonly observed at Høvsøre is the presence of outliers on the opposite part of the 1:1 line (positive outliers), i.e. the wind lidar wind speeds are higher than the cup ones. This behavior is due to cloud contamination, which has a large effect on the continuous wave lidars because of the increasing measurement volume with height (Peña et al., 2009). Natural Power, the company which produces the ZephIR wind lidar, developed a 'cloud correction algorithm' that solves the problem.

From our experience and knowledge we were certain that these negative outliers were provoked by mist and fog which increases the backscatter coefficient from aerosols at low heights. In order to show this, we analyze the scaling factor output from the wind lidar at two heights, 40 and 116.5 m. The scaling factor is an output of the ZephIR wind lidar and indicates how much the spectra of radial velocities has to be scaled for analysis due to the intensity of backscatter radiation. By taking the ratio of the scaling factors at two heights, e.g. 40 and 116.5 m, the episodes where the concentration of aerosols at two heights highly differs can be found. This ratio is an indicator of clouds or in some cases fog or mist episodes. Figure 132-left shows the scaling ratio as function of wind lidar/cup wind speed ratio.

When the scaling ratio is about 1, the wind speed ratio is about 1 too as the aerosol profile in the atmosphere is nearly constant. It is evident that there are many 'episodes' with scaling ratios above 2, i.e. possible mist at the lower height (in this case 40 m). When we compare

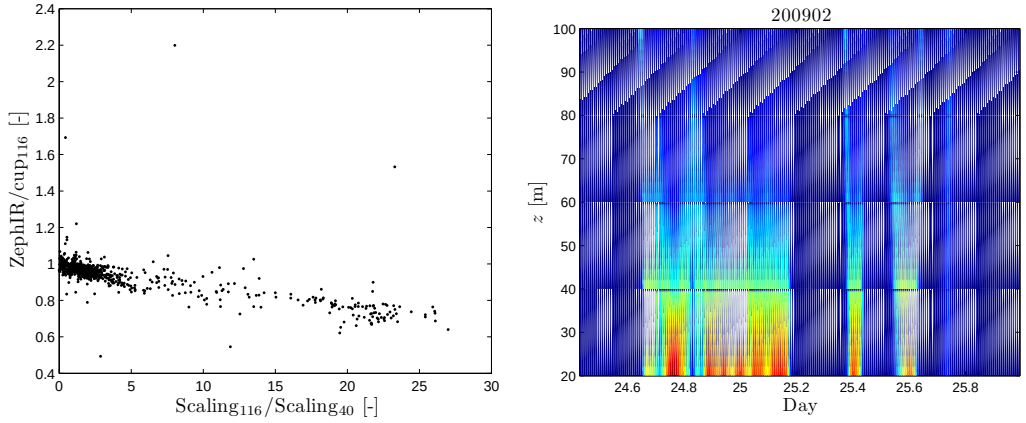

Figure 132: (left) The ZephIR wind lidar/cup anemometer wind speed ratio at 116.5 m at Høvsøre as function of the scaling ratio from measurements at 116.5 and 40 m. (right) Ceilometer backscatter coefficient for most of the days where scaling ratio is above 2

the results when a scaling ratio filter is used an improvement in the wind speed comparison is found (Fig. 133). Data on the figures are shown for scaling ratios below 2.

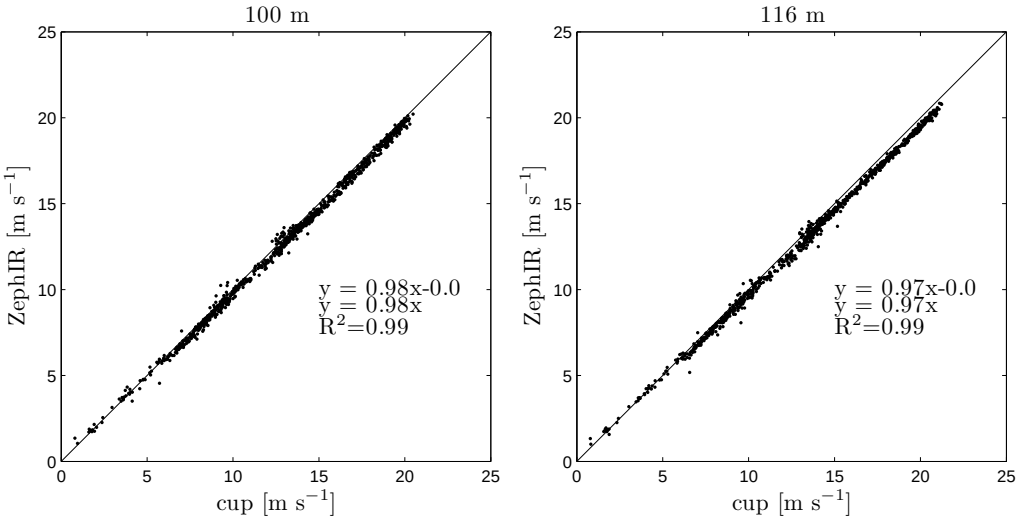

Figure 133: Wind speed comparison between a ZephIR wind lidar and the cup anemometers at Høvsøre at 100 m (left) and 116.5 m (right) after filtering for low fog and mist episodes using the scaling ratio

An independent check has been performed on the times where scaling ratios above 2 were found. There are around 140 episodes between the midday of Februrary 24, 2009, and the night of February 25, 2009, which account for ∼50% of the outliers removed in the wind speed comparison. A ceilometer was used for this purpose and revealed very high aerosol backscatter intensities for this period (see in Fig. 132-right, the non-blue colors at low heights).

Appendix B: The wind lidar at Fino 3

A ZephIR wind lidar was installed at the Fino 3 research platform and observed winds for 6 months (April to October 2011). It measured winds at 51, 71, 91, 101, 130 and 160 m AMSL, overlapping the Fino 3 measurements at heights 50, 70, 90 and 100 m AMSL. The idea of the wind lidar installation on the Fino 3 platform was to extend the observations of the mast with accurate wind lidar wind speed measurements. However, first wind lidar/cup anemometer comparisons revealed an underestimation of the wind lidar wind speed compared to the cups for the four overlapping heights (Fig. 134).

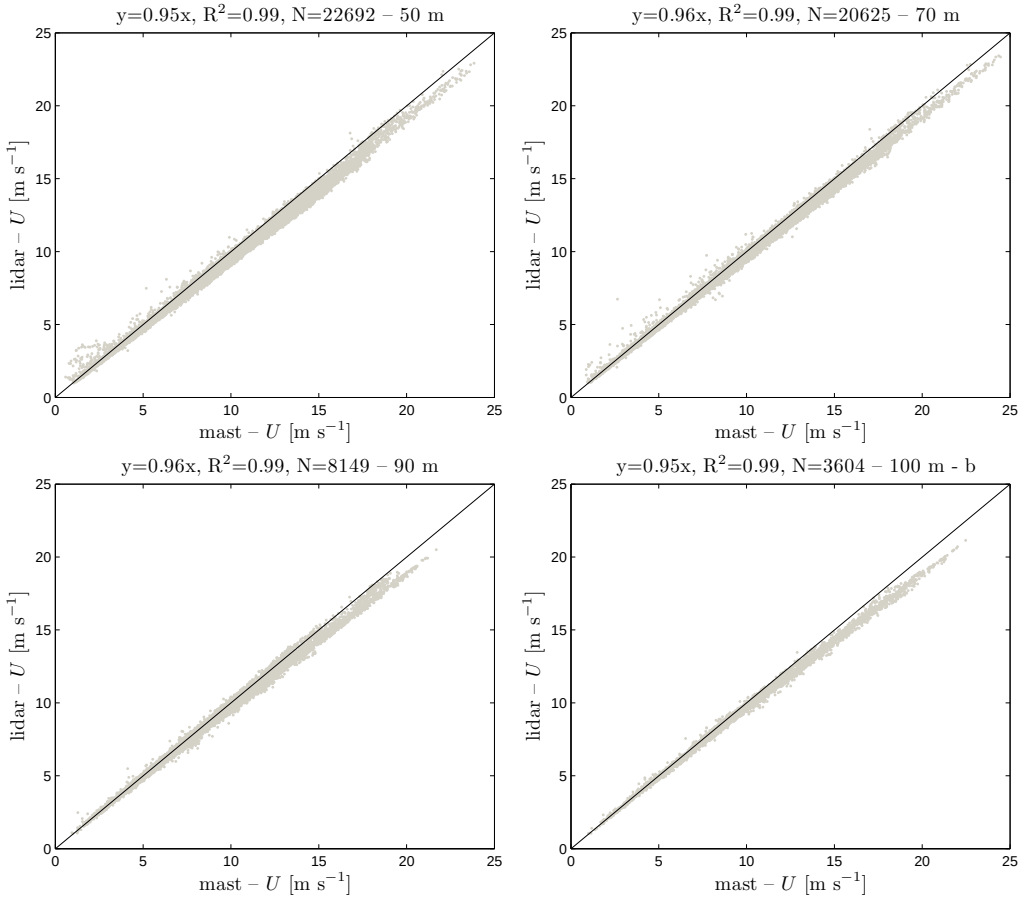

Figure 134: *Comparison of wind speeds for the wind lidar at Fino 3 at 4 overlapping heights: 50 m AMSL (top left), 70 m AMSL (top right), 90 m AMSL (bottom left) and 100 m AMSL (bottom right)*

At the heights 50, 70 and 90 m AMSL the wind speed is measured at three different booms on the mast so in the figure is illustrated the comparison by selecting the boom which is less distorted by the other booms and mast. For the 100 m AMSL height there is only one boom and thus the fewer data (wind directions affected by the mast are discarded). The slope of the linear regression is 0.95–0.96 for all heights There is definitively a distortion effect of the mast on the wind lidar scans. The wind lidar scans the atmosphere around the mast and from the figure of eight, i.e. a polar graph showing the radial wind speeds for the scan area at each height, it is evident that the wind lidar scans are affected by the wake of the mast (Detlef Kindler, personal communication). However, even at 100 m (the maximum height of the mast), the wind lidar highly underpredicts the cup wind speed.

Analysis on the wind lidar profiles was also performed. The wind shear parameter α has been derived from the wind lidar measurements at 71 and 51 m AMSL and plotted as a

function of the potential temperature difference (Fig. 135-left). Although the scatter, a trend of increasing α values with increasing potential temperature is observed as expected, since stable conditions, where α is higher, appear with increasing potential temperature difference. Figure 135-right illustrates a similar comparison but α is plotted as function of the gradient Richardson number given as,

$$\mathrm{Ri_g} = \left(\frac{g}{T}\right) \frac{(\Delta\Theta_v/\Delta z)}{(\Delta U/\Delta z)^2}, \tag{B-1}$$

where $\Delta\Theta_v$ and ΔU are the differences of potential temperature and wind speed at two levels separated at a distance Δz. For Fino 3, the temperatures at 55 and 29 m AMSL and the wind speeds at 71 and 51 m AMSL are used (together with pressure at 23 m AMSL and relative humidity measurements at 29 and 55 m AMSL). From the figure, a clear increase of α values is observed with increasing $\mathrm{Ri_g}$ values. Together with the 10-min values, a running mean is plotted and clearly shows the trend.

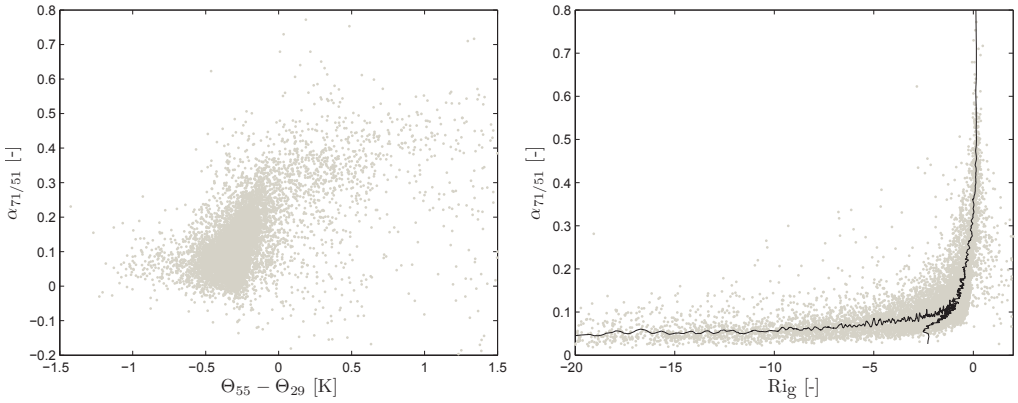

Figure 135: Variation of the wind shear parameter α at Fino 3 with potential temperature difference (left) and gradient Richardson number (right). A running mean is shown in the solid line

Figure 136-left illustrates the error in wind speed at 71 m AMSL as function of $\mathrm{Ri_g}$. Here, the error is defined as the difference between the wind lidar wind speed and that estimated from the diabatic wind profile in Eq. (5), i.e. accounting for atmospheric stability. To estimate the wind speed at any height, the diabatic wind profile is first fitted to the wind lidar observation at 51 m AMSL assuming Charnock's relation in Eq. 4 with $\alpha_c = 0.0144$ (to get the friction velocity).

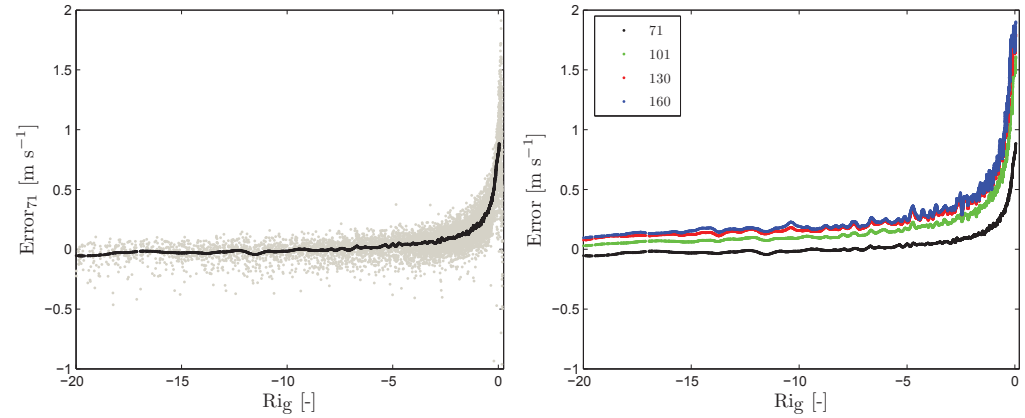

Figure 136: The error in wind speed prediction at Fino 3 as function of the gradient Richardson number for the 71 m AMSL height (left) and four different heights (rights)

As shown in the figure the error increases for increasing Ri_g values, as expected, since the diabatic wind profile has problems particularly under stable conditions (due to the BLH, low level jets, surface layer height, etc.). Figure 136-right shows the error computations at each wind lidar height, where the error increases the higher above the ground due to the limitation of the diabatic wind profile to predict winds particularly under stable conditions.

Appendix C: Wind lidar corrections at Utsira

C.1 Wind lidar error at Utsira

The conical scanning wind lidars over- and under-estimate the wind speed compared to a point measurement at the same height when the flow is not homogenous. This "error" can be estimated by simulating the wind lidar scanning configuration combined with the flow model of WAsP Eng. At Utsira, the flow over the island has been analyzed for four main directions (North–0°, East–90°, South–180°, and West–270°).

Figure 137 shows the result for the vertical component of the wind speed, w, at 40 m for a southerly reduced geostrophic wind. The errors from the conical scanning wind lidars can be easily observed in the figure, because the wind speed (in this case the vertical wind speed) is obviously not the same at all the points within the measurement volume.

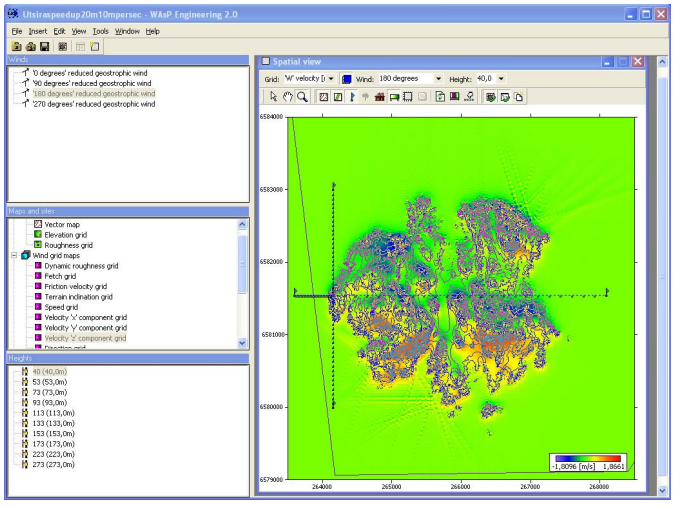

Figure 137: The Utsira island in WAsP Eng. The colors show the vertical wind speed for a southerly geostrophic wind speed of 10 m s^{-1}. The wind lidar is located in the intersection of the transects

Based on the wind lidar error script of WAsP Eng, we are able to estimate the error of the wind lidar at all measuring heights compared to an "imaginary" mast with cups at the same heights for 12° sectors. Figure 138 illustrates the result of the script for the WindCube (assuming that the first beam is oriented to the North) for some selected heights. These results can be used for correcting the observations of the vertical wind speed profile from the wind lidar. The wind lidar error script of WAsP Eng only takes into account the error due to the flow inhomogeneities when scanning conically. The error due to the measurement volume is not estimated.

C.2 Fast flow modeling over Utsira

One simple and very fast fashion to estimate the influence of the terrain on the measurements performed on the island (in this case at the wind lidar location in Fig. 137) is to estimate the flow speed up for four main wind directions at all measuring heights. We have done this by placing four different transects aligned with the four directions and the wind lidar location as common intersection. The speed up can be then estimated by inserting four reduced geostrophic winds correspondent to the four different directions.

We can compare the results of the flow model for the upstream and the wind lidar located

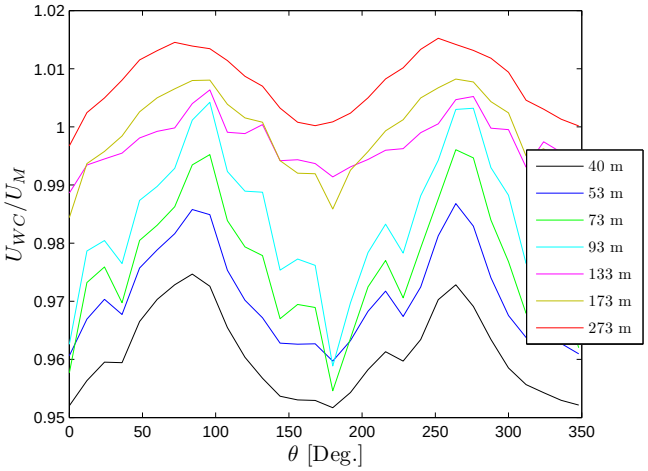

Figure 138: *Ratio of the WindCube to the imaginary cup wind speed for different wind directions and heights*

vertical wind speed profiles for the four different directions. Figure 139 illustrates this comparison for a geostrophic wind of 7 m s^{-1}. In Fig. 140 the same results are shown, but the wind speed has been normalized by the 40 m value, the directions has been separated, and a very preliminary analysis of the wind lidar observations has been included. In Figs. 141 and 142 similar results are shown compared to those in Figs. 139 and 140, but for a geostrophic wind of 10 m s^{-1}.

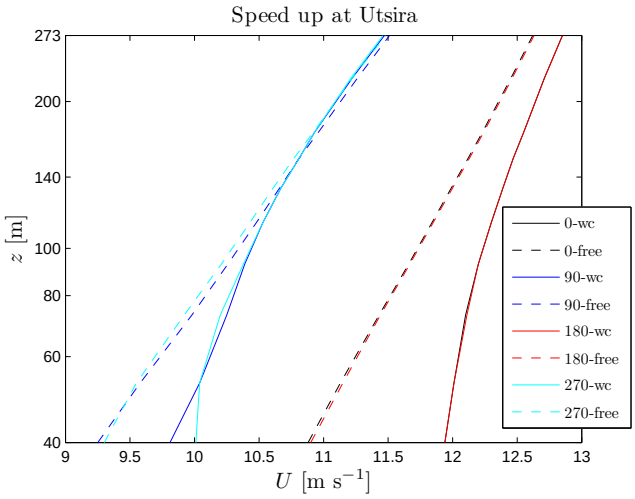

Figure 139: *Comparison of the upstream (free) and wind lidar (wc) located wind profiles for the four main directions. The upstream wind profiles are shown in dash lines and the wind lidar located wind profiles in solid lines*

C.3 Sensitivity to resolution

WAsP Eng can also be used to test the importance of the model resolution for capturing the *perturbations* caused by e.g. terrain complexity. For the case of Utsira, this is done by inserting a long transect along the island in the south-north direction, because this is the preferred wind direction at the site (see Fig. 143). The wind speed perturbations are extracted at different stations 57.5 m apart along the transect at a height of 40 m from different grid resolutions.

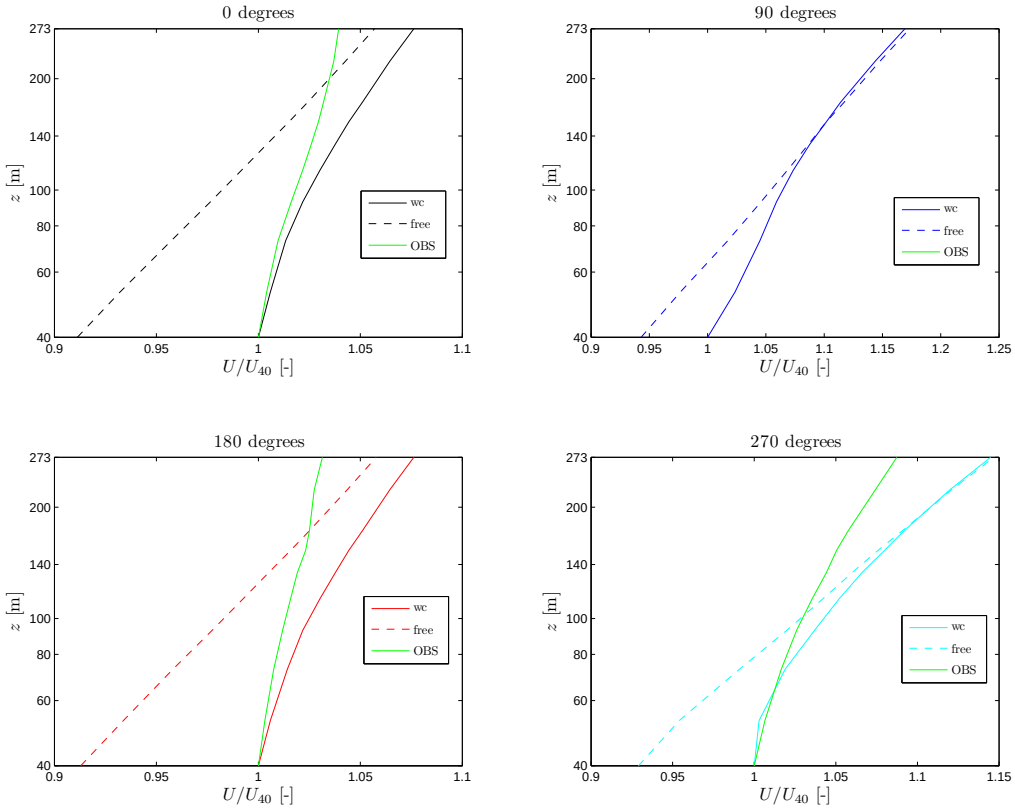

Figure 140: *Comparison of the upstream and lidar located wind profiles for the four main directions (the four panels). The upstream wind profiles are shown in dash lines and the lidar located wind profiles in solid lines of the same color. A preliminary analysis of the lidar data is shown in green color*

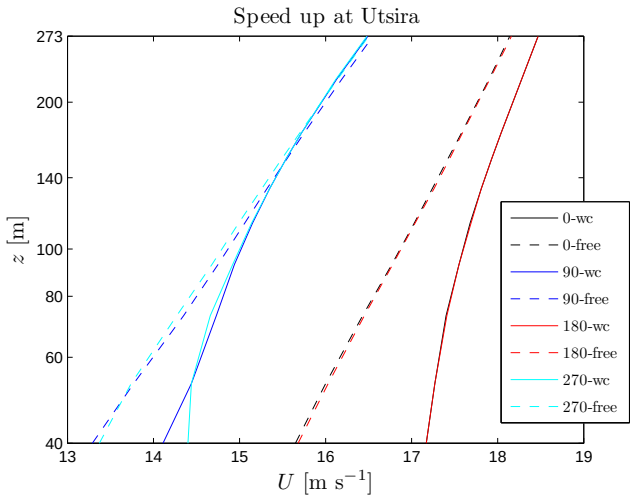

Figure 141: *Comparison of the upstream and wind lidar located wind profiles for the four main directions. The upstream wind profiles are shown in dash lines and the wind lidar located wind profiles in solid lines*

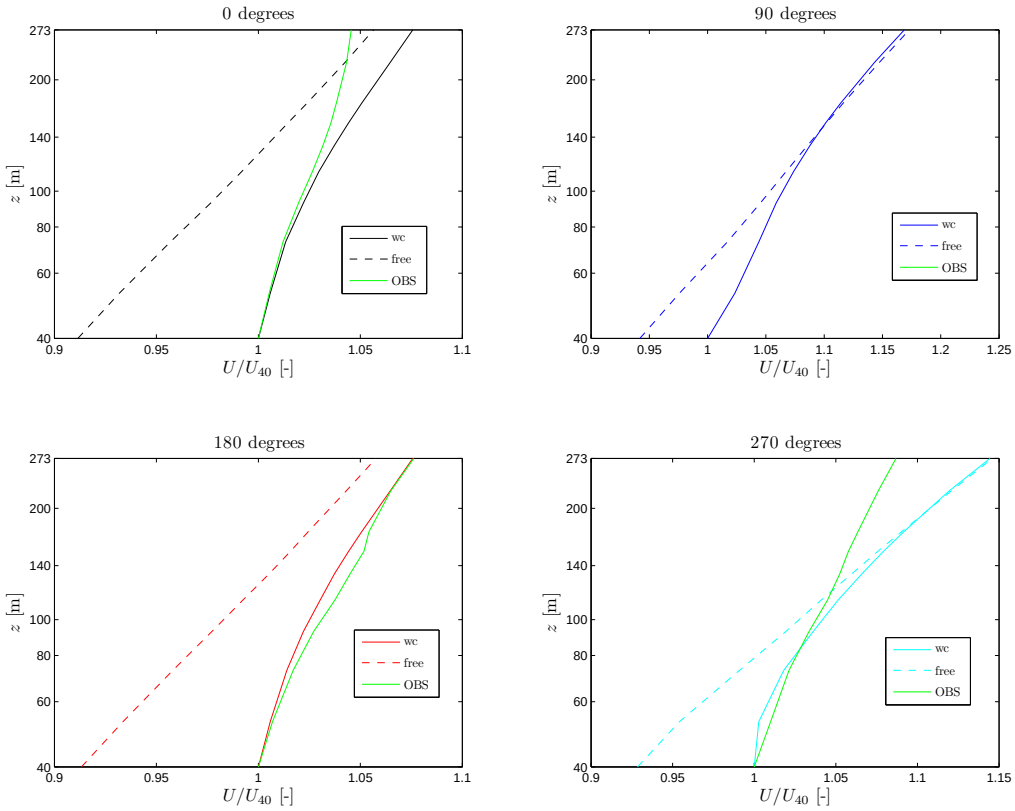

Figure 142: Comparison of the upstream and wind lidar located wind profiles for the four main directions (the four panels). The upstream wind profiles are shown in dash lines and the wind lidar located wind profiles in solid lines of the same color. A preliminary analysis of the wind lidar data is shown in green color

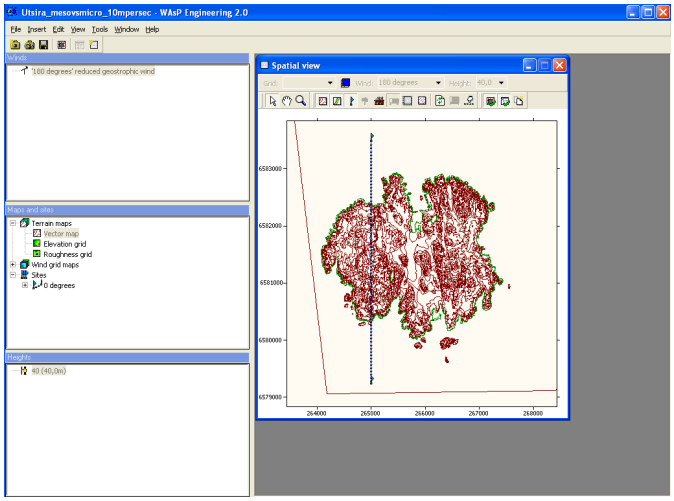

Figure 143: WAsP Eng resolution's sensitivity analysis of the Utsira island

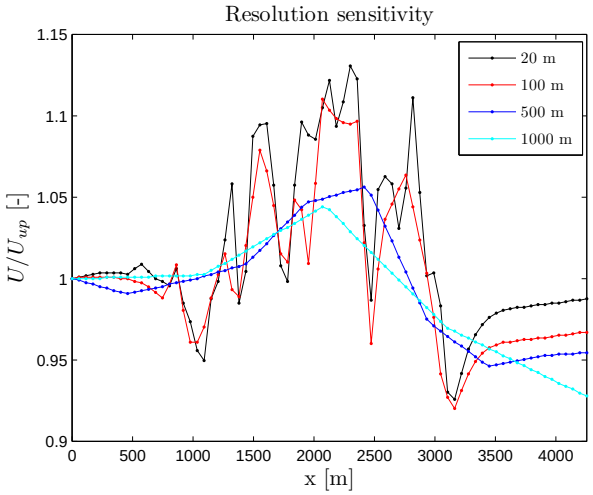

Figure 144: Sensitivity analysis of the resolution of the model in WAsP Eng. The upstream wind speed has been used for the normalization of the perturbation

DTU Wind Energy
Technical University of Denmark

Frederiksborgvej 399
4000 Roskilde
Denmark
Phone +45 4677 5024

www.vindenergi.dtu.dk